

2017

Assessment of Fluid Residence Time in Reservoirs – Case Study of Radiolysis Effects in Crude Oils from China and Norway

Zhao, Jing

Zhao, J. (2017). Assessment of Fluid Residence Time in Reservoirs – Case Study of Radiolysis Effects in Crude Oils from China and Norway (Master's thesis, University of Calgary, Calgary, Canada). Retrieved from <https://prism.ucalgary.ca>. doi:10.11575/PRISM/25028

<http://hdl.handle.net/11023/3794>

Downloaded from PRISM Repository, University of Calgary

UNIVERSITY OF CALGARY

Assessment of Fluid Residence Time in Reservoirs – Case Study of Radiolysis Effects in Crude
Oils from China and Norway

by

Jing Zhao

A THESIS

SUBMITTED TO THE FACULTY OF GRADUATE STUDIES

IN PARTIAL FULFILMENT OF THE REQUIREMENTS FOR THE

DEGREE OF MASTER OF SCIENCE

GRADUATE PROGRAM IN GEOLOGY AND GEOPHYSICS

CALGARY, ALBERTA

April 2017

© Jing Zhao 2017

Abstract

Fluid residence time in a trap is a key factor in many petroleum systems evaluation, basin modeling and carbon storage studies. It will not only provide constraints for basin modeling but also contribute an alternative approach to caprock efficiencies evaluations for carbon storage and oil charge studies. However, dating of fluid flow events in petroleum systems is currently based on indirect methods, and direct assessment of hydrocarbon charge and residence time from analysis of crude-oil is not feasible. In the 1990s, Frolov et al. examined abundant olefin concentrations in crude oil and proposed a new concept of olefin generation in crude oils by natural radiolytic dehydrogenation of saturated hydrocarbons. Motivated by this concept and development of radiation chemistry, the study of my thesis aims at investigating the radiolysis effects and mechanisms, identifying a hydrocarbon-related potential proxy system, and thus, to develop a new precise analytical method to permit functional dating of reservoirs by organic geochemical proxies with realistic reservoir gamma ray doses.

High-dose (0–10000 kGy) and low-dose (0–200 kGy) gamma ray irradiation experiments were designed and conducted on the selected crude oil samples from the Chinese Tarim Basin, the North Sea and the Barents Sea, which aim to find novel radiation damage products and discover potential radiolysis marker candidates as well as analytical methods to quantify them. The original and irradiated oil samples were separated into saturated and aromatic hydrocarbon fractions, and were characterized using gas chromatography-mass spectrometry (GC-MS). The high-dose irradiation results were applied to develop methods, study the key radiolysis mechanism and detect radiolysis markers, while low-dose irradiation results were further used to derive correction factors and build a more precise and realistic correlation between radiolysis proxies and irradiation dose.

After irradiation, the majority of GC-MS monitored compounds were destroyed at different rates. The rates are dependent on the original concentration, compound class, molecular size (carbon number) and the oil matrix. A few compounds, particularly *n*-alkanes C_{9–12}, were generated after oil radiolysis. The dating proxies were determined from GC-MS results and preliminary dating concepts of the reservoir filling were developed. In an ideal scenario, knowing the irradiation dose and the reservoir radiation dose rate from analysis of samples would enable the calculation of reservoir residence age. Future work will further explore the analytical approaches, proxy modeling and the application of such concepts in case histories.

Acknowledgements

Firstly, I would like to express my sincere gratitude to my supervisors Dr. Steve Larter and Dr. Haiping Huang for the continuous support on my master study and related research, for their patience, motivation, and immense knowledge. Steve's and Haiping's guidance helped me in all the time of research and writing of this thesis. My sincere thanks also go to Dr. Lloyd Snowdon and Dr. Thomas Oldenburg who provided me great help on thesis writing and revision. Without their precious support it would not be possible to conduct and finish this research.

Then, I would like to thank the great team members of RvW projects:

- Priyanthi Weerawardhena and Kim Nightingale for their invaluable lab guidance. Without their help and assistance, I would not be able to finish the lab work in a standard manner and get these excellent data.
- Renzo Correa, the project manager, for his excellent leadership and rigorous attitudes towards research, leading me to a more professional way after over two years of collaboration.
- Roshanak Sonei for her patience and support in reviewing previous results and carrying on experimental research.
- Dr. Eduardo Villarreal Barajas from Faculty of Medicine for his patient explanation and guidance on the low-dose irradiation experiments conducted at Foothills Hospital.
- Sponsors from Lundin Energy for their financial support and professional assistance during sponsor meetings.

Besides, I also thank all the current and previous fellows at PRG Group: Susan Dooley, Ryan Snowdon, Melisa Brown, Gabriella Gonzalez, Aprami Jaggi, Ranya Algeer, Jagos Radovic, Yuan Bao, Bin Cheng, Jingping Ma, Tianxin Jiang and Qianru Wang for the valuable assistance in my daily life and stimulating discussions on my research topics.

Last but not the least, I would like to thank my parents and my friend Kevin for their support and love during the difficult time.

Table of Contents

Abstract	ii
Acknowledgements	iii
Table of Contents	iv
List of Tables	vii
List of Figures	viii
List of Abbreviations	xiii
Chapter One: Introduction and Literature Review.....	1
1.1 Background	1
1.2 Petroleum system timing.....	2
1.3 Method development and limitation of dating fluid residence time	5
1.3.1 Potassium-argon (K/Ar) dating of illites.....	6
1.3.2 Fluid inclusions.....	6
1.3.3 Radiometric couples rhenium-osmium (Re/Os).....	7
1.4 Radiation chemistry of hydrocarbons	8
1.4.1 Previous study on natural radioactivity.....	8
1.4.2 Introduction to the basics of radiolysis	9
1.4.3 Gamma ray: source, unit of measurement, energy and interaction.....	10
1.5 Motivation and research objective	11
Chapter Two: Geological Background	14
2.1 Tarim Basin, NW China	14
2.1.1 Geological setting	14
2.1.2 Petroleum systems of Tarim Basin	15
2.2 North Sea and Barents Sea, Norway.....	16
2.2.1 Geological setting of the North Sea	17
2.2.2 Petroleum Systems of the North Sea.....	19
2.2.3 Geological setting of the Barents Sea	19
2.2.4 Petroleum systems of the Barents Sea	21
Chapter Three: Samples and Methods	22
3.1 Samples information	22
3.1.1 Oil/condensate samples from Tarim Basin, NW China.....	22
3.1.2 Oil samples from North Sea and Barents Sea.....	23
3.2 Separation of hydrocarbon fraction.....	24

3.3 Characterization method	25
3.4 γ -ray irradiation experiments	25
3.4.1 High-dose irradiation experiment	27
3.4.2 Low-dose irradiation experiment	27
Chapter Four: Basic Radiolysis Effects and Mechanism	31
4.1 Compound destruction under high-dose irradiation (50-10000 kGy)	31
4.2 "Level 1" compounds	34
4.2.1 Tricyclic terpanes (TTs) and hopanes (PTs)	34
4.2.2 Phenanthrene and alkylphenanthrenes (P)	38
4.2.3 Aromatic steroid hydrocarbons (TAS & MAS)	41
4.2.4 Steranes (STs)	43
4.3 "Level 2" compounds	47
4.3.1 Naphthalene and alkyl-naphthalenes (N)	47
4.3.2 Dibenzothiophenes (DBTs)	50
4.3.3 Normal and isoprenoid alkanes	53
4.4 "Level 3" compounds (compounds with poor correlated concentration and dose)	55
4.4.1 Adamantanes (AD)	55
4.4.2 Bicyclic sesquiterpane (BSTs)	57
4.5 Basic radiolysis mechanism	58
4.5.1 Influencing factor: original concentration	58
4.5.2 Influencing factor: compound class	61
4.5.3 Influencing factor: oil matrix	62
Chapter Five: Case studies I and II: High-dose and low-dose irradiated oils	63
Case study I: High-dose irradiated oils from Tarim Basin, NW China	63
5.1 Basic geochemical characteristics of original oils from Tarim Basin	63
5.2 Compound destruction rates: "SCORE" for representative radiolysis markers	65
5.2.1 Saturated hydrocarbon: TTs, PTs, STs	66
5.2.2 Aromatic hydrocarbons: N, P, DBTs and TAS	68
Case study II: Low-dose irradiated oils from the North Sea and Barents Sea, Norway	71
5.3 Basic geochemical characteristics of original oils from North Sea and Barents Sea	71
5.4 Compound destruction under low-dose irradiation	73
5.4.1 Concentration: no significant change	73
Chapter Six: Conclusions and Future work	75
REFERENCES	76

APPENDIX 1: GC-MS IDENTIFICATION OF COMPOUNDS	80
A1.1 Saturated hydrocarbons.....	80
A1.2 Aromatic hydrocarbons.....	85

List of Tables

Table 1.1 Overview of chronological parameters in the petroleum system and current states of major dating tools	4
Table 3.1 Table of Tarim sample information (O: Ordovician; T: Triassic; C: Carboniferous. °API = [141.5/specific gravity-131.5])	22
Table 3.2 Table of Tarim sample bulk composition (after Zhang and Huang, 2005)	23
Table 3.3 Table of North Sea and Barents Sea sample information	24
Table 3.4 List of all samples irradiated under high-dose and low-dose	26
Table 4.1 Radiation doses (kGy) of NSLO and AHO samples irradiated in phase 1 & 2.....	31
Table 4.2 Compound type categories.....	34
Table 4.3 Normalized radiolysis destruction slopes (normalized concentration vs. dose) for investigated hydrocarbon compounds in high-dose irradiated NSLO samples	62
Table 5.1 Molecular parameters based on saturated hydrocarbon and aromatic hydrocarbons for T1-T10 non-irradiated samples	63
Table 5.2 Table of selected Tarim sample information and bulk composition	65
Table 5.3 Radiolysis SCORE for compounds in T1, T2 and T6 high-dose irradiated samples ...	69

List of Figures

Fig. 1.1 RvW Project overview and research objectives	1
Fig. 1.2 Conventional petroleum system profile.....	3
Fig. 1.3 Schematic illustration of fluid fluxes (oil, gas, water, CO ₂) in and out of a reservoir. For example, a charged flux of say, oil (q ₁), contributes via storage and transport in the reservoir to leakage through the caprock (q ₂) and spillage from the spill point of the trap (q ₃). By age dating the fluid residence time profile in the reservoir and comparing it with radionuclide distribution using a fluid age mixing model, in principle, the charge history and fluxes may be delimited (after Larter et al., 2012).	5
Fig. 1.4 Irradiation dose-response curves (after Frolov et al., 1998)	9
Fig. 1.5 Alpha, beta, gamma and neutron radiation.....	10
Fig. 2.1 Tectonic sketch map of the Tarim Basin and stratigraphic column of the Lower Palaeozoic strata (Huang et al., 2015)	14
Fig. 2.2 Stratigraphy of the cratonic region of the Tarim Basin (after Zhang et al., 2005)	15
Fig. 2.3 Norwegian Continental Shelf Map	16
Fig. 2.4 Structural Map of the North Sea Triple Junction (modified after Faersth, 1996)	17
Fig. 2.5 Composite stratigraphic column for the Norwegian sector of the northern part of the South Viking Graben (after Kane et al., 2010)	18
Fig. 2.6 Regional geology feature of Loppa High area, Barents Sea.....	19
Fig. 2.7 Stratigraphic chart illustrating the main lithologies in the Barents Sea (after Ohm et al., 2008)	20
Fig. 3.1 The decay scheme of ⁶⁰ Co.....	27
Fig. 3.2 The decay scheme of ¹³⁷ Cs	28
Fig. 3.3 Low-dose irradiation Experiment Design.....	29
Fig. 3.4 Dose rate calibration method.....	29
Fig. 3.5 Correlation between irradiation dose vs. net optical density (netOD) and calibration results for Layer C	30
Fig. 4.1 Plot showing the variation in concentration of C ₂₇ 10β(H),13α(H) 20S diasterane (C ₂₇ βαS) with radiation dose (kGy) for NSLO and AHO samples.....	31

Fig. 4.2 Plot of initial concentration versus the degradation slope ($\Delta\text{ppm}/\Delta\text{kGy}$) for investigated saturated and aromatic hydrocarbons in high-dose (0–10000 kGy) irradiated NSLO and AHO samples.....	32
Fig. 4.3 Plot of normalized slopes (normalized concentration vs. dose) for investigated saturated and aromatic hydrocarbons in high-dose (0–10000 kGy) irradiated NSLO and AHO samples.	33
Fig. 4.4 Distribution of tricyclic terpanes and hopanes shown in GC-MS chromatogram m/z 191 of the saturated hydrocarbon fraction of non-irradiated NSLO and AHO samples.....	35
Fig. 4.5 Plots showing the variation in concentrations of tricyclic terpanes and pentacyclic terpanes (hopanes) with radiation dose (kGy)	36
Fig. 4.6 Plot of slopes ($\Delta\text{ppm}/\Delta\text{kGy}$) for tricyclic terpanes and pentacyclic terpanes (hopanes) in high-dose (0–10000 kGy) irradiated NSLO and AHO samples	37
Fig. 4.7 Plot of normalized slopes (normalized concentration vs. dose) for tricyclic terpanes and pentacyclic terpanes in high-dose (0–10000 kGy) irradiated NSLO and AHO samples.....	38
Fig. 4.8 Structure of phenanthrene and C ₁₋₂ methyl-naphthalenes	38
Fig. 4.9 Distribution of alkylphenanthrenes shown in m/z of 192, 206 mass chromatograms in the aromatic hydrocarbon fraction of non-irradiated NSLO samples.....	39
Fig. 4.10 Plots showing the variation in concentrations of phenanthrenes and C ₁₋₂ alkyl-phenanthrenes with radiation dose (kGy)	39
Fig. 4.11 Plot of slopes ($\Delta\text{ppm}/\Delta\text{kGy}$) for phenanthrenes and C ₁₋₂ alkyl-phenanthrenes in high-dose (0–10000 kGy) irradiated NSLO and AHO samples	40
Fig. 4.12 Plot of normalized slopes (normalized concentration vs. dose) for phenanthrene and C ₁₋₂ alkyl-phenanthrenes in high-dose (0–10000 kGy) irradiated NSLO and AHO samples.....	40
Fig. 4.13 Conversion of C ₂₉ -monoaromatic (MA) to C ₂₈ -triaromatic (TA) steroids during thermal maturation (Peters et al., 2005).....	41
Fig. 4.14 Distribution of mono-, tri-aromatic steroid shown in m/z 253, 231 mass chromatograms in the aromatic hydrocarbon fraction of non-irradiated NSLO and AHO samples.....	41
Fig. 4.15 Plots showing the variation in concentrations of monoaromatic steroid (MAS) and triaromatic steroid (TAS) hydrocarbons with radiation dose (kGy)	42

Fig. 4.16 Plot of slopes ($\Delta\text{ppm}/\Delta\text{kGy}$) for MAS and TAS in high-dose (0–10000 kGy) irradiated NSLO and AHO samples.....	42
Fig. 4.17 Plot of normalized slopes (normalized concentration vs. dose) for MAS and TAS in high-dose (0–10000 kGy) irradiated NSLO and AHO samples	43
Fig. 4.18 Formation and isomerization of steranes.....	43
Fig. 4.19 Distribution of steranes shown in m/z 217 mass chromatogram in the saturated hydrocarbon fraction of non-irradiated NSLO and AHO samples	44
Fig. 4.20 Plots showing the variation in concentrations of steranes with radiation dose (kGy)...	44
Fig. 4.21 Plots showing the variation in concentrations of steranes with radiation dose (kGy) for samples irradiated in phase 1 & 2	45
Fig. 4.22 Plot of slopes ($\Delta\text{ppm}/\Delta\text{kGy}$) for steranes in high-dose (0–10000 kGy) irradiated NSLO and AHO samples.....	46
Fig. 4.23 Plot of normalized slopes (normalized concentration vs. dose) for steranes in high-dose (0–10000 kGy) irradiated NSLO and AHO samples.....	46
Fig. 4.24 Structure of naphthalene and C ₁₋₅ methylnaphthalenes	47
Fig. 4.25 Structure distribution of alkylnaphthalenes shown in m/z 156, 170,184 mass chromatogram in the aromatic hydrocarbon fraction of non-irradiated NSLO samples	47
Fig. 4.26 Plots showing the variation in concentrations of naphthalenes and C ₀₋₅ alkylnaphthalenes with radiation dose (kGy).....	48
Fig. 4.27 Plots showing the variation in concentrations of naphthalenes with radiation dose (kGy) for NSLO and AHO samples irradiated in phase 1 & 2.....	49
Fig. 4.28 Plot of slopes ($\Delta\text{ppm}/\Delta\text{kGy}$) for sum C ₀₋₅ alkylnaphthalenes in high-dose (0–10000 kGy) irradiated NSLO and AHO samples	49
Fig. 4.29 Plot of normalized slopes (normalized concentration vs. dose) for naphthalenes and C ₁₋₅ alkylnaphthalenes in high-dose (0–10000 kGy) irradiated NSLO and AHO samples ..	50
Fig. 4.30 Chemical structure of dibenzothiophenes and alkyldibenzothiophenes.....	50
Fig. 4.31 Distribution of alkyldibenzothiophenes shown in m/z 198 and 212 mass chromatograms in the aromatic hydrocarbon fraction of non-irradiated NSLO samples.....	51
Fig. 4.32 Plots showing the variation in concentrations of MDBT and C ₀₋₃ DBT with radiation dose (kGy)	51

Fig. 4.33 Plot of slopes ($\Delta\text{ppm}/\Delta\text{kGy}$) for dibenzothiophene and C ₀₋₃ dibenzothiophenes in high-dose (0–10000 kGy) irradiated NSLO and AHO samples	52
Fig. 4.34 Plot of normalized slopes (normalized concentration vs. dose) for dibenzothiophene and C ₀₋₃ dibenzothiophenes in high-dose (0-10000 kGy) irradiated NSLO and AHO samples.....	52
Fig. 4.35 Distribution of normal and isoprenoid alkanes shown in m/z 85 mass chromatogram in the saturated hydrocarbon fraction of non-irradiated NSLO and AHO samples (Pr: Pristane, Ph: Phytane)	53
Fig. 4.36 Plots showing the variation in concentrations of C ₉₋₃₅ n-alkanes with radiation dose (kGy) for NSLO samples irradiated in phase 1 & 2	54
Fig. 4.37 Plots showing the variation in concentrations of C ₉₋₃₅ n-alkanes with radiation dose (kGy) for AHO samples	54
Fig. 4.38 Plot of slopes ($\Delta\text{ppm}/\Delta\text{kGy}$) for normal alkanes (C ₉ –C ₃₅) and isoprenoid alkanes (pristane and phytane) in high-dose (0–10000 kGy) irradiated North Sea Light Oils.....	55
Fig. 4.39 Distribution of C ₀₋₄ alkyl-adamantanes shown in m/z 136,135,149,163,177 mass chromatograms in the saturated hydrocarbon fraction of non-irradiated NSLO and AHO samples.....	56
Fig. 4.40 Plots showing the variation in concentrations of sum C ₀₋₄ alkyl-adamantanes with radiation dose (kGy)	57
Fig. 4.41 Distribution of bicyclic sesquiterpanes shown in m/z 123 mass chromatogram in the saturated hydrocarbon fraction of non-irradiated NSLO	57
Fig. 4.42 Structure plots showing the variation in concentrations of bicyclic sesquiterpanes with radiation dose (kGy)	58
Fig. 4.43 Plots showing the variation of slopes ($\Delta\text{ppm}/\Delta\text{kGy}$) with original concentration of C ₀₋₅ naphthalenes in phase 1&2 irradiated NSLO samples	59
Fig. 4.44 Plots showing the variation of slopes ($\Delta\text{ppm}/\Delta\text{kGy}$) with original concentration of n-C ₉₋₃₅ alkanes in phase 1&2 irradiated NSLO samples.....	60
Fig. 4.45 Plots showing the variation of slopes ($\Delta\text{ppm}/\Delta\text{kGy}$) with original concentration (ppm) of all compounds (normal alkanes excluded) in phase 1&2 irradiated NSLO samples.....	61
Fig. 5.1 Terpane distribution (m/z 191) of non-irradiated Tarim Oils (see Fig. 4.4 for terpane compounds distribution; black traces: oils; red traces: condensates)	64

Fig. 5.2 Sterane compounds distribution (m/z 217) of non-irradiated Tarim Oils (black traces: oils; red traces: condensates)	65
Fig. 5.3 Plots showing the variation in concentrations of tricyclic terpanes (TTs), hopanes (PTs), steranes (STs), diasteranes (Diast) with radiation dose for T1, T2 and T6 samples (kGy)	66
Fig. 5.4 Plots showing the variation of "score" for tricyclic terpanes (TTs) with radiation dose for T1, T2 and T6 samples (kGy)	67
Fig. 5.5 Plots showing the variation in concentrations of C ₀₋₅ naphthalene (C ₀₋₅ N), C ₀₋₂ phenanthrenes (C ₀₋₂ P), dibenzothiophenes (DBTs) and triaromatic steroid hydrocarbons (TAS) with radiation dose for T1, T2 and T6 samples (kGy)	68
Fig. 5.6 Plots showing the variation of "score" for triaromatic steroid hydrocarbons (TAS) with radiation dose for T1, T2 and T6 samples (kGy)	69
Fig. 5.7 Ratio of C ₂₈ bisnorneohopane/ C ₂₉ 17 α (H),21 β (H) hopane (C ₂₈ BH/C ₂₉ H) for 23 investigated oils from North Sea and Barents Sea area (well data from <i>Lundin Energy</i>) ...	71
Fig. 5.8 Ternary plot of C ₂₇₋₂₉ regular steranes	72
Fig. 5.9 Cross plot of C ₂₉ $\beta\beta$ /($\alpha\alpha$ + $\beta\beta$) versus C ₂₉ 20S/(20S+20R)	72
Fig. 5.10 Plots showing the variation in concentrations of steranes with radiation dose (kGy) ..	74

List of Abbreviations

Symbol	Definition
API	American Petroleum Institute gravity
NSLO	North Sea light oil
AHO	Alberta heavy oil
TT	tricyclic terpanes
PT	pentacyclic triterpanes
ST	steranes
N	naphthalene
P	phenanthrene
BST	bicyclic sesquiterpane
DBT	dibenzothiophene
TAS	triaromatic steroid hydrocarbon
MAS	monoaromatic steroid hydrocarbon
AD	adamantane
<i>n</i> -alkane	normal alkane
con./concn.	concentration
NW	northwest
Cond.	condensate

Chapter One: Introduction and Literature Review

1.1 Background

Age dating reservoir fluid residence time is the crucial parameter in many petroleum systems, basin modeling and carbon storage studies. A precise definition of an oil or gas residence time dating method would be valuable for petroleum systems studies, and has major impacts on basin geosciences. However, according to Larter et al. (2012), dating hydrocarbon charge and residence time from analysis of crude-oil is currently not feasible due to the lack of a practical method, and there is a need to establish a well-designed field and laboratory-based research program to develop a practical age dating methodology to study reservoir residence time.

The “RvW” Project was launched in 2012 by the PRG group at the University of Calgary and scientists from Lundin (Norway), aimed at developing a deployable and direct reservoir oil residence age dating tool. A previous three-year study (RvW phase I) indicated how nuclear radiation in reservoirs impacts oil composition and how feasible it is to develop *in situ* gamma ray radiolysis proxies (RvWs), such as the petroleum radiolysis products described by Frolov et al. (1998), as a means of assessing oil and gas residence time profiles in reservoirs. Such an approach, in principle, may be capable of providing the first reliable oil charge dates available (Marcano et al., 2015).

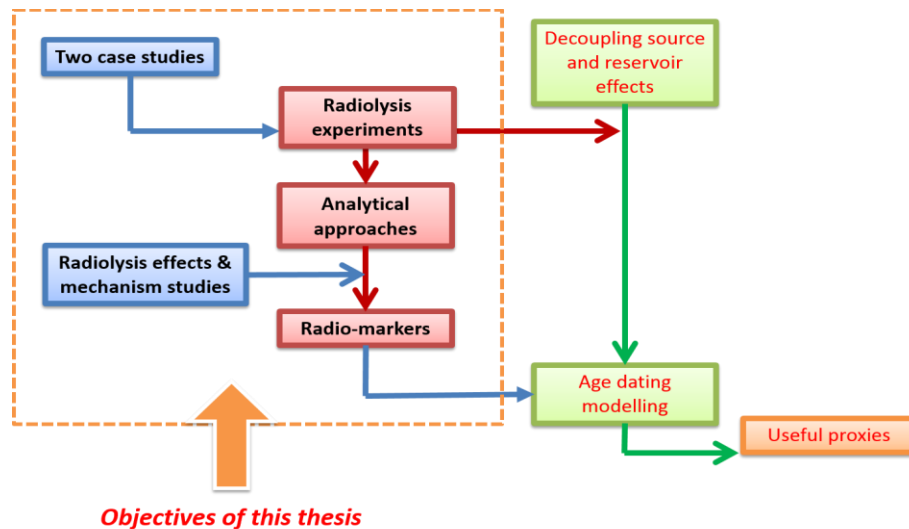


Fig. 1.1 RvW project overview and research objectives

The overall objectives and processes of “RvW” project are shown in Fig.1.1. The major goal of this thesis (RvW phase II) is to look into the radiolysis effects and potential mechanism for molecular compounds of crude oils based on GC-MS analysis, trying to identify useful proxy systems and their utility in fluid reservoir age dating, thus to preliminarily develop the concept of fluid residence time assessment by organic geochemical proxies with realistic reservoir gamma ray doses. Two case studies on crude oils from different regions were also carried out for further discussion about the radiolysis mechanism and identifying good radiolysis markers.

In this thesis, Chapter One firstly describes several approaches which have been tried to assess the fluid charge and residence histories in reservoirs, as well as their limitations. The section also discusses the basics of radiation chemistry and natural radiation phenomena in reservoirs to support our research, followed by the discussion of the motivation and objective of our specific approach. Then, Chapter Two mainly gives the general geological background of our major study areas, with the information about their basic tectonics, stratigraphy and petroleum systems. The section also explains the reasons of why these samples were chosen and the advantages of using these study areas for case studies. In Chapter Three, a brief introduction of the sample sets and methodology is provided, followed by the introduction of how we conducted the irradiation experiments for targeted samples under different dose ranges. The radiolysis effects referring to the correlation between concentrations of individual compounds and irradiation dosage are described in Chapter Four and the basic radiolysis mechanisms are proposed and discussed. In Chapter Five, case studies of two sample sets irradiated under high-dose and low-dose are examined, further discussion of radiolysis mechanisms including the effect of compounds class is provided, molecular size and oil matrix are considered, and finally a conclusion and description of future work are given in Chapter Six.

1.2 Petroleum system timing

The petroleum system is a unifying concept that encompasses all the disparate elements and processes of petroleum geology (Fig.1.2). The essential elements of a petroleum system include an effective source rock, a reservoir rock, a seal rock and an overburden rock. In a petroleum system, there are two processes: the trap formation and generation-expulsion-migration-accumulation of hydrocarbons (Magoon and Dow., 1994). The chronological parameters in the

petroleum system and development of applicable dating tools are shown in Table 1.1. The timing of geological processes is crucial for petroleum systems evaluation.

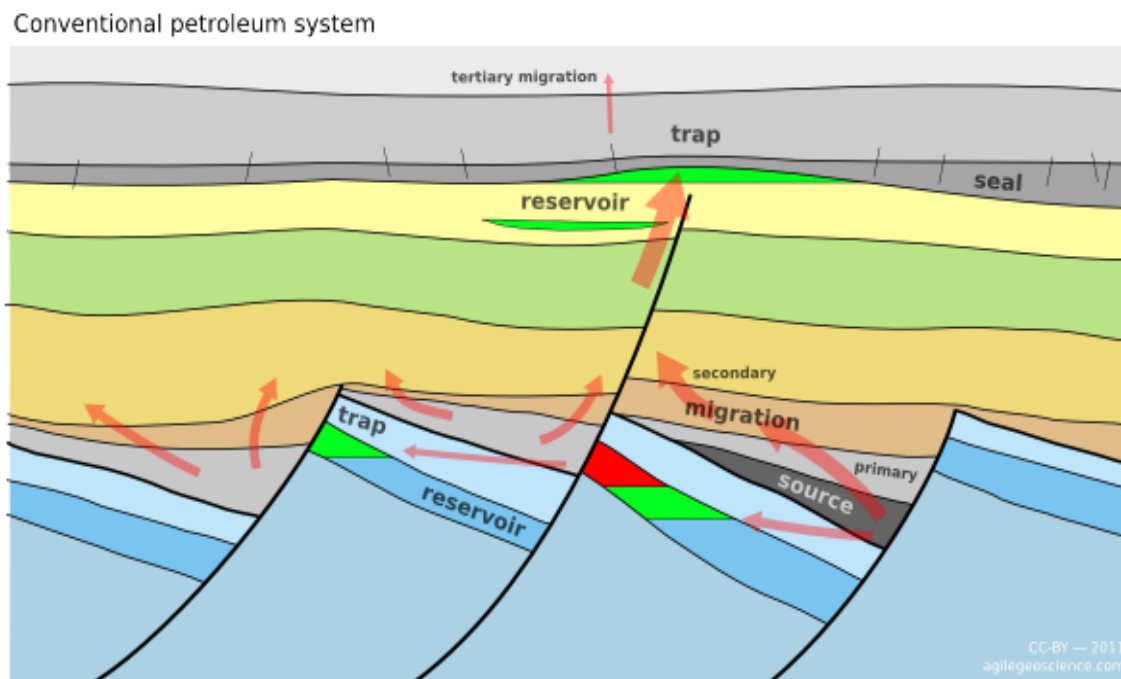


Fig. 1.2 Conventional petroleum system profile
(http://subsurfwiki.org/wiki/Petroleum_system)

Overall, the dating of source rock deposition and reservoir horizons ages by radiometrically calibrated biostratigraphic assessments is now routine and effective (Erwin, 2006). There are also some capabilities such as dating source rocks using age-related biomarkers. Various compounds in source rocks show distributions through geologic time suggesting their use as age-related biomarkers in crude oils (Peters et al., 2005). The dating tools such as the basin modelling were generally advanced. The hydrocarbon generation process was simulated to calculate the charge or the volume of hydrocarbons available for entrapment, to predict the volumes and locations of accumulations and their properties. It brings together several dynamic processes, including sediment deposition, faulting, burial, kerogen maturation kinetics and multiphase fluid flow (Mubarak et al., 2009). However, to model the petroleum potential and reconstruct generation history, some specific past conditions, including heat-flow history, surface temperature, paleowater depth, must be evaluated and treated as boundary conditions by the modelling software. With these variations, the method is relatively unconstrained and it provides source rock maturation times, not actual charge times.

Table 1.1 Overview of chronological parameters in the petroleum system and current states of major dating tools

Parameter	Current state (tools)
Source age	Some capabilities (age-related biomarkers)
Generation age	Fairly advanced but relatively unconstrained (basin modelling)
Charge time	A few very doubtful tools
Trap fluid residence time	No viable proxies (fluid inclusions, K/Ar-illite, Re/Os; not effective)

Generally, the dating of fluid flow events in petroleum systems is currently based on indirect methods, while, many petroleum system phenomena related to formation and alteration of accumulations are highly time dependent. For example, the extent of crude oil alteration by biodegradation is highly controlled by the thermal and oil charge history of a petroleum column (Larter et al., 2003, 2006) and time-dependent mixing of reservoir fluids (Koopmans et al., 2002). The petroleum charge times, oil residence times and charge rate in a trap are valuable for petroleum systems studies (Larter et al., 2012). In petroleum systems, many parameters depend on oil reservoir residence time and oil mixing (e.g. heavy oil properties), and charge times and rates are key variables in controlling hydrocarbon prospectivity as they define volumes of trapped petroleum and the dynamics of trap integrity.

The residence age of fluids in a subsurface reservoir will depend on position in the fluid column, the fluxes of fluids into and out of the trap and diffusive and advective mixing of fluids in the reservoir (Fig. 1.3). In principle, examination of the residence age spatial profiles in a fluid column, coupled to a numerical model of fluid flux, might permit for estimates of the charge, spillage and leakage fluid fluxes into and from the trap (Larter et al., 2012).

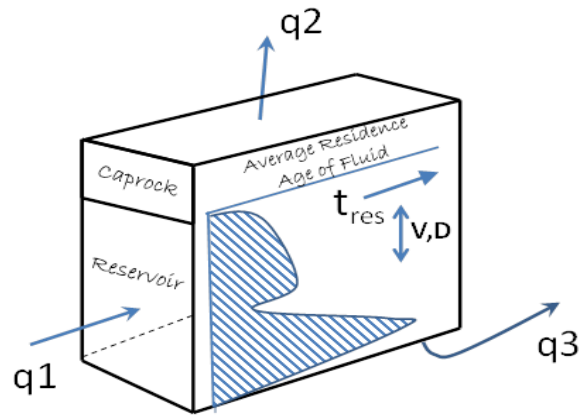


Fig. 1.3 Schematic illustration of fluid fluxes (oil, gas, water, CO₂) in and out of a reservoir. For example, a charged flux of say, oil (q_1), contributes via storage and transport in the reservoir to leakage through the caprock (q_2) and spillage from the spill point of the trap (q_3). By age dating the fluid residence time profile in the reservoir and comparing it with radionuclide distribution using a fluid age mixing model, in principle, the charge history and fluxes may be delimited (after Larter et al., 2012).

1.3 Method development and limitation of dating fluid residence time

In the past study, the most widely adopted dating method of fluid residence time is radiometric dating. It is generally used to date materials such as rocks or carbon, in which trace radioactive impurities were selectively incorporated when they were formed. It compares the abundance of a naturally occurring radioactive isotope within the material to the abundance of its decay products, which form at a known constant rate of decay. Together with stratigraphic principles, radiometric dating methods are used in geochronology to establish the geological time scale (MacRae, 1998). For the specific purpose of dating petroleum reservoir age, K-Ar dating of authigenic illite growing in reservoirs stand out, which is based on the impact of varying water saturations on the diagenetic evolution of mineral systems that provide either radiometric dating couples. The rhenium-osmium radiometric dating has also been discussed in recent years (Selby and Creaser, 2005; Selby et al., 2007).

Fluid inclusion homogenization temperature is also a diagenetic approach which is based on the assessment of phase behavior of fluids trapped in fluid inclusions in authigenic mineral phases (Karlsen et al., 1993). Temperature, pressure and composition data collected from fluid inclusions are used to determine the environment of diagenesis and the timing of cementation and migration (McLimans, 1987).

1.3.1 Potassium-argon (K/Ar) dating of illites

Dating of fibrous illite clay in reservoirs by using K-Ar ages is not a new technique (e.g. Sommer, 1978), and has been well developed. It is based on measurement of the radioactive decay product of an isotope of potassium (K) into argon (Ar). Potassium is a common element found in many materials, such as micas, clay minerals, tephra, and evaporites. Illitic clay is the commonly occurring diagenetic mineral in reservoir sandstones that contains sufficient ^{40}K . Due to the long half-life of potassium (1.3 billion years), the technique is considered to be applicable for dating minerals and rocks more than 100,000 years old.

Illite is often the last or one of the latest mineral cements to form prior to hydrocarbon accumulation. Since the displacement of formation water by hydrocarbons will cause silicate diagenesis to cease or slow, K-Ar ages for illite will confine the timing of this event (the oldest geological age of petroleum accumulation), and also constrain the maximum age of formation of the trap structure (Haszeldine et al., 2003). As an example, the Middle Jurassic Brent oil-bearing sandstone in the North Sea was dated with K-Ar isotopic determination combined with scanning electron microscopy (SEM) observations and x-ray diffractometry (XRD) controls of the diagenetic formation of illitic clay minerals (Hamilton et al., 1992).

However, considering the gaseous nature of the daughter isotope (Ar), the validity or unreliability of this method due to contamination of the measured age dates has been argued extensively. According to Liewig and Clauer (2000), to interpret illite K-Ar dates appropriately, it is necessary that the K present is associated only with illite, the initial Ar is of atmospheric origin and the illite K-Ar system remained closed since crystallization or rehomogenization. These features may differ from one sample to the other, or even between the size fractions of the same sample (Glasmann et al., 1989).

1.3.2 Fluid inclusions

Fluid inclusions are formed in reservoir cements during the process of burial. Roedder (1984) described the various origins and types of fluid inclusions together with criteria for their recognition. Basically, fluid inclusions are entrapped as imperfections during the growth of a cement crystal (primary) or during a later sealing event (secondary) (Mclimans, 1987). Fluid inclusions in quartz or calcite can trap live petroleum phases, which can provide trapping temperature and time estimates. Through the use of vapor/liquid ratio and homogenization

temperature characterization, it can provide information on the composition of oil as a function of time during the oil charge process (Aplin et al., 2000). There were applications using fluid inclusion homogenization temperatures to date the formation of a petroleum reservoir, with the combination of burial and geothermal history of the host rock (Middleton et al., 2000; Kelly et al., 2000).

However, there exists a multiplicity of solutions when using fluid inclusions to define the migration of oil and gas. It commonly only tracks the earliest phase of charge and there is no clear relationship between fluid inclusion occurrence and the actual volume of petroleum in the porosity of reservoir. Therefore, fluid inclusions provide evidence of a date and composition for the earliest charge in the reservoir. The temperature range assessed by it may be corresponded to different period, and the tectonic movement, hydrocarbon generation history and other aspects need to be considered comprehensively to determine the major migration period. Thus, this dating tool provides no direct information on the actual residence age of the fluids in the reservoir porosity.

1.3.3 Radiometric couples rhenium-osmium (Re/Os)

Rhenium-osmium (Re-Os) dating is a form of radiometric dating based on the beta decay of the isotope ^{187}Re to ^{187}Os . Selby and Creaser (2005) argued that the sufficient amounts of Re and Os in hydrocarbons makes the ^{187}Re - ^{187}Os radioisotope system a viable mechanism to date petroleum charge times and the isochrons of Re-Os were well defined. Both rhenium and osmium appear to be associated with the resin and asphaltene fractions and thus may be source related. Selby et al. (2007) suggested that $^{187}\text{Re}/^{188}\text{Os}$ and $^{187}\text{Os}/^{188}\text{Os}$ values in asphaltene at the time of oil generation are similar to those of the whole oil, proposing that asphaltene fractions can be used to approximate the Re-Os isotopic compositions of the whole oil.

However, the radiometric signal carried from the source rock would carry information on either source age or oil expulsion time from the source rock, but it is not obvious how it would carry the signal for the time the oil enters the reservoir. The defined isochrons can also result from fluid exchange and mixing of measured species between oils and water, which might not represent the actual isochron. Larter et al. (2012) suggested that Re-Os method does not define the location of the metals (rhenium and osmium) and exchange between fluids (oil and water) and solids (source rock, carrier bed, and reservoir) may impact data, and the mechanism of how this internal

radiometric clock works is also uncertain. Therefore, this method seems to be interesting but is not yet validated.

1.4 Radiation chemistry of hydrocarbons

Based on the above discussion, an ideal way of directly dating the fluid residence history involves the compositional variation in petroleum hosted components that do not exchange chemically with reservoir media, and are also independent of secondary alteration processes such as biodegradation, thermochemical sulfate reduction or evaporative fractionation. Of all the systems that might be able to directly date in-reservoir fluid residence time, the impact of nuclear radiation from radiogenic nuclides in a reservoir rock on trapped fluid composition seems potentially to be a viable route to an age dating proxy.

1.4.1 Previous study on natural radioactivity

In past study of crude oil composition, it was generally accepted that oils do not contain olefins in significant amounts. However, Hoering (1977) described the considerable quantities of alkenes in Bradford Field (Pennsylvania) and Kushnarev et al. (1989) also detected olefinic hydrogen atoms in several East Siberian crude oils. Motivated by these phenomena, Frolov and colleagues conducted many investigations in 1990s, which initially examined the distribution of olefins in crude oil and proposed various origins to account for these distributions. They analysed hundreds of crude oils from various basins in Russia and several crude oils from Oklahoma and Texas (U.S.A.) ranging from Precambrian up to Cenozoic. The samples were studied for their content of olefin by thin layer chromatography, infra-red spectroscopy, GC, ^1H and ^{13}C NMR (Frolov et al., 1998; Frolov and Smirnov, 1994). Crude oil samples irradiated by ^{60}Co γ -irradiation were investigated (Frolov et al., 1998).

Frolov et al. (1998) explained how radiolysis (natural radiation damage) produces olefins in crude oils and proposed a new concept of olefin generation in crude oils by natural radiolytic dehydrogenation of saturated hydrocarbons (Fig. 1.4).

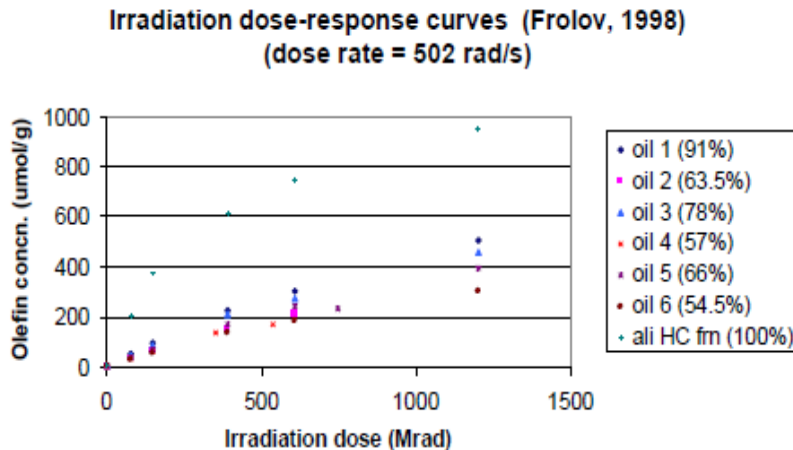


Fig. 1.4 Irradiation dose-response curves (after Frolov et al., 1998)

However, crude oils are very reactive under high radiation doses, with excited hydrocarbon, non-hydrocarbon and alkene molecules created through non-selective bond breaking, bimolecular recombination reactions, hydrogen loss, condensation processes and reactions between any species present, including water, N₂ and CO₂. Specific radiolysis products are hard to measure, as large numbers of low concentration species are produced, from even simple binary compound mixtures (Larter et al., 2012). Thus, spectroscopic approaches, such as nuclear magnetic resonance (NMR), are needed to accurately assess alkene production (Frolov et al., 1998; Frolov and Smirnov, 1994).

1.4.2 Introduction to the basics of radiolysis

Radiolysis is the dissociation of molecules by nuclear radiation. It is the cleavage of one or several chemical bonds resulting from exposure to high-energy flux. The radiation here is associated with ionizing radiation, which refers to the process with enough energy to free electrons from atoms or molecules, thereby ionizing them. It is categorized by the nature of the particles or electromagnetic waves that create the ionizing effects and may be grouped as directly ionizing (any charged massive particle can ionize atoms directly by fundamental interaction if it carries sufficient kinetic energy, e.g. alpha, beta, gamma radiation) and indirectly ionizing (electrically neutral, does not interact strongly with matter, e.g. neutron radiation).

Figure 1.5 demonstrates the constitution of different kinds of ionizing radiation and their ability to penetrate matter. Alpha (α) radiation consists of a fast-moving helium-4 (⁴He) nucleus and is stopped by a sheet of paper. Beta (β) radiation, consisting of electrons, is halted by an aluminum

plate. Gamma (γ) radiation, consisting of energetic photons, is eventually absorbed as it penetrates a dense material. Neutron (n) radiation consists of free neutrons that are blocked by light elements, like hydrogen, which slow or capture them.

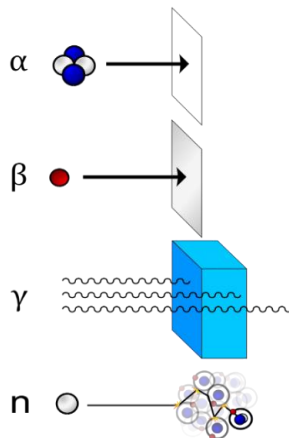


Fig. 1.5 Alpha, beta, gamma and neutron radiation

The natural radiolysis of petroleum in the earth crust is likely caused by irradiation from natural radioactive elements of the U and Th disintegration series (Frolov et al., 1998). It is widely known that in the natural reservoir, the bulk of the primary emitted particle radiation (alpha and beta particles) from the major radionuclides in rocks would be stopped within the mineral grains themselves, assuming relatively uniform distribution of radionuclides among the parent mineralogy. Therefore, gamma radiation produced during the decay series would be the primary irradiator of pore fluids such as water and oil. Frolov et al. (1998) believe that γ -bombardment can be used to simulate processes involved in the natural radiolysis. Thus, we described the alteration and radiolysis effect in crude oils by modeling γ -irradiation in this work, and it would appear that the photons involved in gamma radiation typically travel around 30 cm in sedimentary rocks (Williams, 1963).

1.4.3 Gamma ray: source, unit of measurement, energy and interaction

Gamma rays (γ) are penetrating electromagnetic radiation of a kind arising from the radioactive decay of atomic nuclei and consist of high-energy photons. Natural sources of gamma rays on Earth include a wide range of phenomena, both non-radioactive decay and radioactive decay. In this thesis, we mainly talk about radioactive decay, referring to the gamma rays produced during decay, which normally occurs after other forms of decay (such as α or β decay) occur. An excited nucleus can decay by the emission of an α or β particle. The daughter nucleus is usually

left in an excited state. It can then decay to a lower energy state by emitting a gamma ray photon, in a process called gamma decay.

The effect of gamma and other ionizing radiation is more closely related to the amount of energy deposited rather than the charge. This is called the absorbed dose. In this study, we adopt the SI unit of absorbed dose: gray (Gy), which is the amount of radiation required to deposit 1 joule of energy in 1 kilogram of any kind of matter.

$$1 \text{ Gy} = 1 \frac{\text{J}}{\text{kg}} = 1 \text{ m}^2 \cdot \text{s}^{-2}$$

Different sources of radionuclides emit gamma rays at various energies, such as ^{40}K (1.46 MeV), ^{232}Th (2.62 MeV), $^{238}\text{U}/^{226}\text{Ra}$ (1.76 MeV), ^{60}Co (1.17/1.33 MeV), ^{137}Cs (0.662 MeV) (Chmielewski, 2007). In our experiments, the radioactive isotope cobalt-60 (^{60}Co) was used in the high-dose irradiation experiment and caesium-137 (^{137}Cs) was used in the low-dose irradiation experiment.

The interaction of gamma ray photons with atoms in fluids has a few possible outcomes. The photon can disappear and be absorbed completely through the photoelectric effect, nuclear triplet production or a photonuclear reaction. It can also be scattered and change its direction but keep its energy (Rayleigh scattering), or lose part of its energy through the Compton effect, whereby photons interact with electrons in atoms losing energy and producing lower energy photons as a result (Bailey et al., 2015).

1.5 Motivation and research objective

Based on previous study, it was hypothesized in RvW phase I that gamma ray radiolysis of pore fluids is a key process in sedimentary rocks. The relatively long transit distance of gamma ray photons in sediments means that local variations in source gamma ray signal within the sedimentary column. For example, the occurrence of more radioactive shales in otherwise less radioactive sandstone or carbonate reservoir sections, could in principle, produce inherited signals in fluid chemistry in reservoir sections adjacent to the shales. This would mean that the local in-reservoir gamma ray signal heterogeneity should be evident on a time-dependent basis in pore fluid chemistry. The reservoir residence effects could, in principle, be distinguished from radiolytic effects on organic matter composition affected in a source rock, if the complicating effects of diffusive and effective mixing can be accounted for.

As suggested by Larter et al. (2012), the most robust dating methods must involve oil components that do not exchange with reservoir media. Thus, the ideas of dating hydrocarbon charge and residence time from analysis of crude-oil alone stand out and need to be resolved in a practical way. In the current approach, we are seeking proxies based on components that can be analyzed in a crude oil sample that can be correlated with the residence time of a petroleum sample in a given reservoir setting. The basic approach is that natural nuclear radiation derived from a reservoir medium can change the composition of crude oils in a systematic way that could allow an observer to determine the radiation dose received by the crude oil while in that reservoir.

Olefinic hydrocarbons were found to be generated mainly from nonselective dehydrogenation of saturated hydrocarbons in the oil, the increases in olefin concentration were linearly correlating with total radiation dose received in laboratory experiments (Frolov et al., 1998). It has also been indicated that natural radiolytic dehydrogenation can affect not only saturated hydrocarbons but also other classes of compounds containing hydrocarbon substituents. Frolov et al. (1998) suggested that the distribution and structures of radiogenic olefins were not strongly influenced by the type and energy of bombardment, or the presence of water, salts or mineral phases, nor by sulfur contents or asphaltene concentrations.

To step forward based on the concept of conducting irradiation experiments on crude oil to analyze the olefins, the idea of learning the reservoir residence time by measuring the specific production under simulated irradiation experiment was considered. However, it is hard to practically measure the irradiation production due to the variety and number of new species as well as the low concentration. Compared with new compound production, the compound destruction, which had already been detected in pilot experiments, would be more appropriate to investigate during oil radiolysis, and could be further considered as potential in-reservoir age dating proxy. It is found that physical processes, especially ubiquitous mixing processes, greatly limit the traditional application of molecular proxies to assessing complex system properties. Thus, a proxy based organic geochemical systems for assessment of petroleum residence time in reservoir demands a physical model to interpret data, which must couple the linked effects of: (a) local generation of radiolysis proxies and compound alteration effects; (b) advection of new oil charge being added to a reservoir resulting in an effective mixing; and (c) local diffusion of products and reactants within fluid columns resulting in diffusive mixing of proxies (RvW internal report). An

ideal residence age dating system is resistant to alteration impacts such as biodegradation and thermochemical sulfate reduction, it can distinguish reservoir ageing from source ageing and can be practically employed with gases as well as liquid components at low cost. The ultimate goal is to establish an applicable and precise reservoir oil residence age dating system with a functional age dating proxy model that can be linked to a basin model.

The main objective of this thesis is to have insights into the radiolysis effects and mechanisms based on a variety of whole crude oil radiolysis experiments. Hundreds of oil samples from China and Norway were irradiated under different dose ranges and analyzed by GC-MS. We also describe how the radiolysis sensitivity of different petroleum species highly depends on chemical classes, concentration and oil matrix. The interpretation of results was aimed at testing and developing a working age dating proxy system.

Chapter Two: Geological Background

The sample suite for this thesis consisted of samples from various geological regions. The original oil samples for the irradiation experiments were collected from the Tarim Basin in China (Fig. 2.1), the North Sea and Barents Sea areas of offshore Norway (Fig. 2.3). This chapter review the basic geological setting of the Tarim Basin, North Sea and Barents Sea, including their tectonics and petroleum systems in order to provide a general background for the studied samples.

2.1 Tarim Basin, NW China

2.1.1 Geological setting

The Tarim Basin, located in the southern Xinjiang Uygur Autonomous Region, NW China, is one of the world's largest frontier basins, with an area of 560,000 km² (Fig. 2.1). It is a Palaeozoic cratonic basin, overlain in the south and north by Mesozoic-Cenozoic Foreland Depressions (Li et al., 1996). The cratonic region mainly consists of the Manjiaer Depression and the adjacent Tabei and Tazhong uplifts.

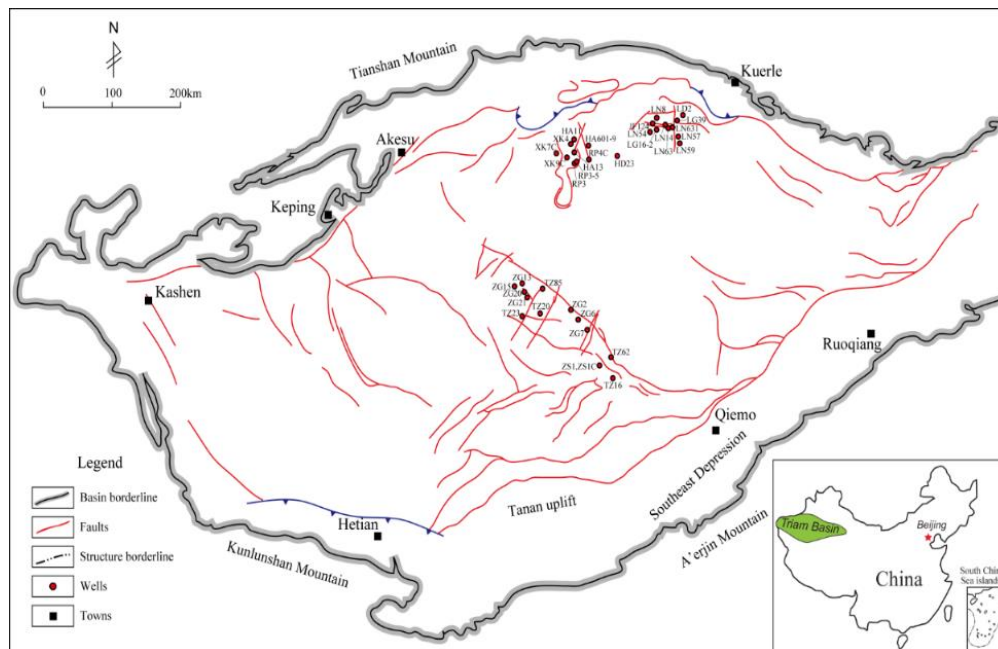


Fig. 2.1 Tectonic sketch map of the Tarim Basin and stratigraphic column of the Lower Palaeozoic strata (Zhang et al., 2015)

The stratigraphy (Fig. 2.2) of the Tarim Basin consists of several marine, continental and transitional sequences (Zhang et al., 2005). The Palaeozoic strata sections were deposited almost entirely in marine settings. The 3 km thick Cambrian-Lower Ordovician strata comprise shallow

marine to lagoonal carbonates, whereas the Middle-Upper Ordovician was deposited during a marine transgression event. Following the deposition of the Silurian and Devonian fine-grained red beds and tidal sandstones, about 1 km of Upper Palaeozoic marine and continental transitional sediments accumulated. After a major Late Permian hiatus, renewed subsidence led to the accumulation of up to 6 km of Mesozoic-Cenozoic fluvio-lacustrine sediments (Zhang et al., 2000, 2005, 2011, 2015; Li et al., 2010; Pang et al., 2012).

Period	Thickness (m)	Lithology	Description	Depositional environment	Petroleum system
Q	100-200		Sand, conglomerate	Continental	overburden
N	2000-4000		Upper part: grey to yellow siltstone and mudstone; lower part: brown-red sandstone and mudstone		
E	100-500		Brown, grey, yellow siltstone and mudstone		
K	700-1100		Brown, grey, yellow siltstone and mudstone		
J	100-300		Sandstone and mudstone		
T	400-600		Interbedded conglomerate, mudstone and sandstone		
P	300-500		Brown, yellow and red sandstone and mudstone	Marine-continental transitional	Reservoir
C	200-800		Interbedded grey mudstone, siltstone and sandstone		Source rock Reservoir
D	0-300		Yellow sandstone and mudstone	Marine	Reservoir
S	0-1000		Yellow sandstone and shale		Source rock
O _{2,3}	100-1500		Dark limestone and mar		
O ₁	500-2000		Gray to dark dolomite and limestone		Source rock/ Reservoir
Є ₃	50-250		Gray dolomite		
Є ₂	100-300		Gray carbonate and shale		
Є ₁	200-500		Gray dolomite		
Pt	200-1500		Carbonate, shale and volcanic rocks		

Fig. 2.2 Stratigraphy of the cratonic region of the Tarim Basin (after Zhang et al., 2005)
2.1.2 Petroleum systems of Tarim Basin

In the Tarim Basin, numerous source rocks, reservoirs and regional cap rocks are developed, with potential source rocks including the Cambrian-Lower Ordovician lagoonal carbonates and mudstones, Middle-Upper Ordovician platform carbonates, Carboniferous-Permian shallow marine carbonates and mudstones, and Triassic-Jurassic coals and lacustrine mudstones. The Carboniferous-Permian source rocks are distributed mainly in the Southwest Foreland Depression, whereas the Mesozoic source rocks are almost exclusively distributed in the foreland depressions (Huang et al., 1999; Zhang et al., 2000; Jia and Wei, 2002).

The Cambrian-Lower Ordovician source rocks generally contain 1.2% to 2.3% TOC and are currently overmature (> 2.0% Ro). The Middle-Upper Ordovician source rocks consist mainly

of argillaceous limestones and marlstones deposited in shelf edge and slope environments, occurring widely in the Tabei (Northern Tarim Basin) and Tazhong (Central Tarim Basin) uplifts and surrounding areas. The average TOC is around 0.43% (maximum 6 wt%), with maturity ranging from mature to overmature (0.8–1.5% Ro) (Hanson et al., 2000).

In the Tarim Basin, faults and fractures are thought to be the main conduit for petroleum migration. Multiphase petroleum generation, migration and accumulation have been widely considered to be characteristic of the Tarim Basin. Multiple charges and various secondary alterations including biodegradation, evaporative fractionation, thermal cracking and thermochemical sulfate reduction exist (Zhang et al., 2000, 2005, 2011, 2015).

This complexity of petroleum system in the Tarim Basin was always a limitation in the past, which made the evaluation of fluid charging history as well as the reservoir residence time very difficult. The conventional age dating methods such as K-Ar dating of illite and fluid inclusion were not precise enough when applied in the specific research of this huge area. Therefore, a definition of oil or gas residence time dating tools would be a crucial parameter for petroleum system studies, and have major impacts on the basin analysis and charge history studies in the Tarim Basin.

2.2 North Sea and Barents Sea, Norway

The study areas are in the Norwegian North Sea and the southern Barents Sea area (Fig. 2.3) and are geographically along the Norwegian Continental Shelf. The samples were distributed within quadrants 7 and 16 in the Norwegian North Sea, quadrant 7120 in the Barents Sea.

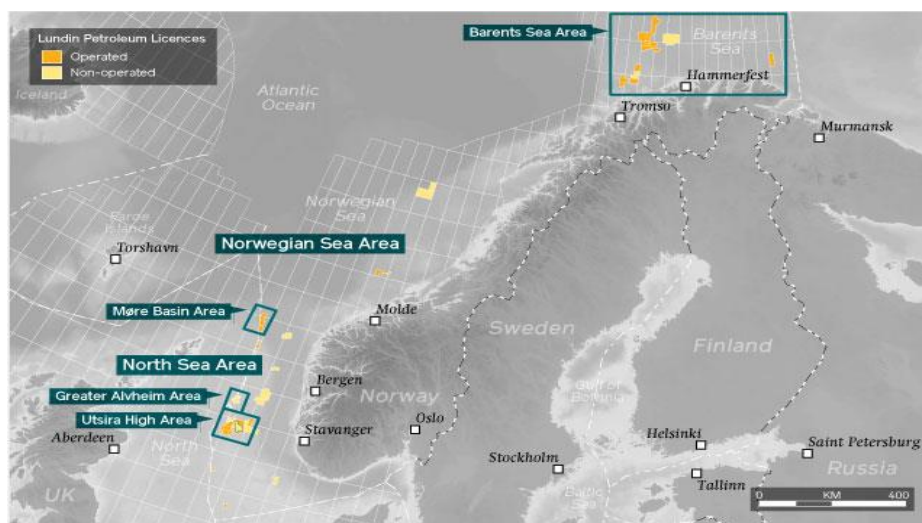


Fig. 2.3 Norwegian Continental Shelf Map

2.2.1 Geological setting of the North Sea

Most selected North Sea samples are from the Utsira High area, which is a prolific hydrocarbon production area (shown in Fig. 2.3 and 2.4). The Utsira High is a large basement high, flanked by the Viking Graben to the west and the Horda Platform to the east (Fig. 2.4). The present structural configuration the result of two major phases of extension (Ziegler, 1992).

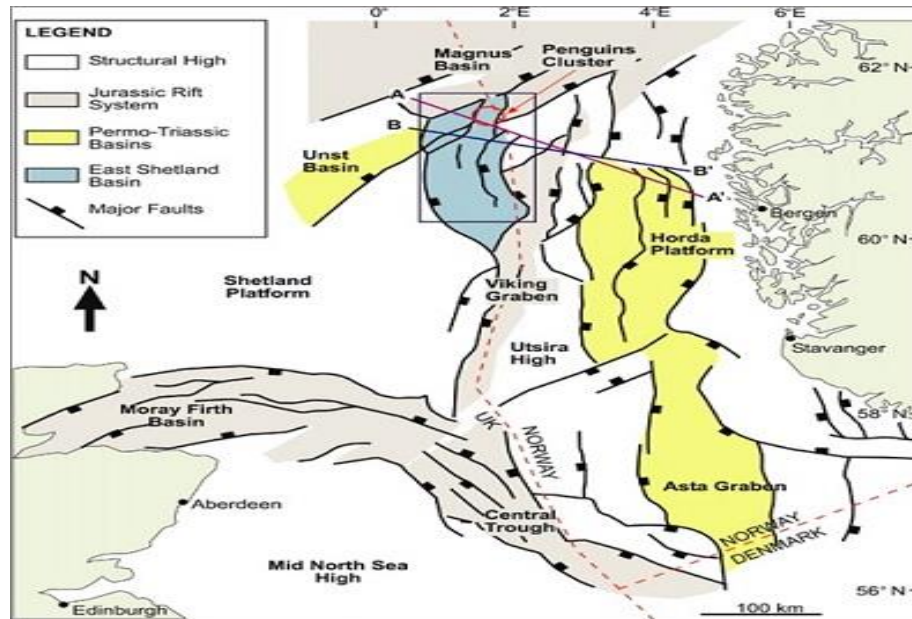


Fig. 2.4 Structural Map of the North Sea Triple Junction (modified after Færseth, 1996)

According to previous studies, the earliest period of extension and fault-controlled basin subsidence is considered to have occurred in the Early-Late Permian (Coward, 1995; Glennie and Underhill, 1998). During this period, the South Viking Graben was located along the northern margin of the North Permian Salt Basin where it formed a broadly north-south-trending, fault-bounded embayment (e.g. Glennie and Underhill, 1998; Ziegler, 1990). Within this embayment, a thick succession of evaporites was deposited (the Zechstein Supergroup), characterized by anhydrite and halite-rich units (Turbot Anhydrite Formation) in the axis of the basin and carbonate-rich, ‘marginal’ evaporite facies (Halibut Carbonate Formation) towards the basin margins (Fig. 2.5; Thomas and Coward, 1996; Glennie et al., 2003). Mobility of salt within the Zechstein Supergroup resulted in thickness variations, and the salt movement commenced during the Triassic resulting in thickness variations in the Triassic succession. During the Early Jurassic, the formation of the Mid-North Sea Dome caused uplift and erosion of the South Viking Graben and the Early Jurassic stratigraphic units are absent within the study area.

System	Series	Group/ Supergroup	Formation	Structural and/or tectono-stratigraphic significance				
Cenozoic			Nordland	post-rift				
			Hordaland					
			Rogaland					
Cretaceous	Upr.	Shetland	Jorsalfare					
			Kyrre					
			Hyggvasson & Blodatta					
	Lwr.	Cromer Knoll	Svarte					
			Rødby					
			Sola					
Jurassic	Upr.	Viking	Draupne		Jurassic minibasin fill			
			Heather					
			Hugin					
	Mid.	Vestland	Sleipner	syn-rift				
			Triassic			Hegre	Skagerrak	Triassic minibasin fill
							Smith Bank	
Permian	Upr.	Zechstein			detachment			
			Lwr.			Rotliegend	Auk	sub-detachment basement
							pre-rift	

Fig. 2.5 Composite stratigraphic column for the Norwegian sector of the northern part of the South Viking Graben (after Kane et al., 2010)

During the Middle Jurassic, collapse of the Mid-North Sea Dome and activity on the Graben Boundary Fault Zone resulted in rapid subsidence and an associated marine transgression (Ziegler, 1990). Shallow marine sediments of the Hugin Formation were deposited above delta-plain deposits of the Sleipner Formation during the earliest rift phase. The main phase of the second extension and subsidence occurred during the Oxfordian to Volgian. Coupled with the rise in sea-level, the increase in fault-driven subsidence rates resulted in continued deepening of the basin, and deposition of the Heather Formation and deep marine mudstones of the Draupne Formation (Late Oxfordian-Late Volgian) (Fig. 2.5). Activity on the Graben Boundary Fault Zone and subsidence in the South Viking Graben waned during the latest Volgian to Ryazanian (Thomas and Coward, 1996).

2.2.2 Petroleum Systems of the North Sea

It is generally agreed that the Jurassic Draupne Formation is the principal petroleum source rock in this area. The Draupne Formation was deposited during the Oxfordian to Ryazanian (Fig. 2.5) in a marine environment with restricted bottom water circulation and thus often under anaerobic conditions. It generally consists of dark grey-brown to black, usually non-calcareous, carbonaceous, occasionally fissile claystone (Barnard and Cooper, 1981; Isaksen and Ledje, 2001). One sample from Brynhild field (shown in Table 3.3), which is situated in the southern part of the North Sea, was selected. The Brynhild reservoir lies at a depth of 3300m in sandstone belonging to the Ula Formation from the Late Jurassic age. The sandstone was deposited in a shallow marine environment.

The previous study indicates the trapping style is variable and includes rotated fault blocks and stratigraphic traps (Pegrum and Spencer, 1990). The cap rock is most commonly the shale of the Draupne Formation. Migration is usually of short distance (Fraser et al., 2003) directly from nearby Upper Jurassic shales.

2.2.3 Geological setting of the Barents Sea

The Barents Sea is located in an intracratonic setting between the Norwegian mainland and Svalbard. It has been affected by several tectonic episodes after the Caledonian orogeny ended in Late Silurian/Early Devonian.



The Barents Sea oils were sampled from the Loppa High area (Fig. 2.6), which forms part of the western margin of the Barents Sea. The Loppa High is an old, Devonian structure, which is flanked by the Hammerfest, Tromsø and Bjørnøya basins. Sediment cover on this high is thin. The two main structural features are the Loppa and Veslemøy highs.

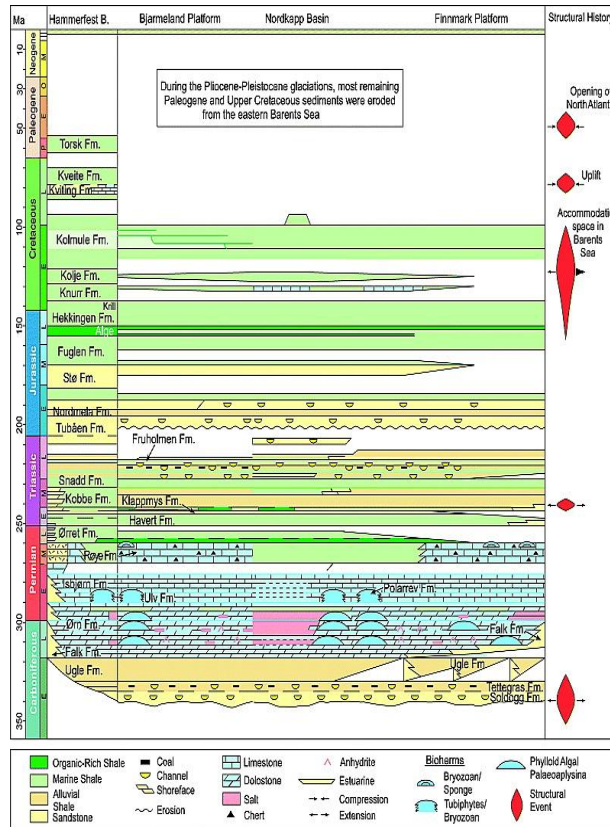


Fig. 2.7 Stratigraphic chart illustrating the main lithologies in the Barents Sea (after Ohm et al., 2008).

Gabrielsen et al. (1990) described the structural elements and lithostratigraphy of the Barents Sea (Figure 2.7). Back to the Mississippian (Early Carboniferous), the Norwegian Barents Sea was dominated by sandstones and alluvial shales with some source rock potential. A marked transition in depositional environment to the Pennsylvanian (Late Carboniferous) is observed, where the period until the Late Permian is dominated by dolostones and limestones and in the Nordkapp Basin the formation of thick salt deposits. The Upper Permian through the Triassic is dominated by marine and alluvial shales and some sandstone layers reflecting the numerous transgressive and regressive episodes of the Triassic. The uppermost Triassic to Middle Jurassic is sandier, reflecting a higher energy depositional environment. The Upper Jurassic and Cretaceous marine shales suggest a more distal marine environment. Late Cretaceous and Tertiary sediments

have partly been removed by erosion as a consequence of episodes of uplift. Three main episodes of uplift are shown at roughly 60 Ma (Paleocene), 33 Ma (Oligocene) and 5 Ma (Pliocene-Pleistocene), the latter two being the most significant (REF). A summary of the structural history of the Barents Sea is also illustrated in the right column of Figure 2.7.

2.2.4 Source rocks of the Barents Sea

The Norwegian Barents Sea covers an area roughly twice the size of the Norwegian North Sea (Figure 2.2), where petroleum presently occurring in traps has been generated and expelled mainly from the Upper Jurassic Kimmeridge Clay equivalent source rock (Ohm et al., 2008). In the Barents Sea, multi-source rock systems have been identified at all stratigraphic intervals from the Carboniferous to the Cretaceous (Figure 2.7). A major hydrocarbon source rock of Middle Triassic age is recognized throughout the Barents Sea area. The Steinkobbe formation has a total organic carbon (TOC) of 2–5%. Locally other Triassic source rocks are seen (Ohm et al., 2008).

Chapter Three: Samples and Methods

This research involved the analysis of crude oil/condensate samples from the Chinese Tarim Basin, oil samples from North Sea and Barents Sea reservoirs. The bulk compositions, sample location and depth information are shown in section 3.1. The samples were separated into saturated and aromatic hydrocarbon fractions based on polarity, as described in section 3.2, and then analyzed by gas chromatography mass spectrometry (GC-MS) for molecular compositions.

Based on the various chemical composition, location and geochemical characterization, several samples were selected for irradiation experiments. The high-dose irradiated samples were selected and analyzed mainly for method development and basic radiolysis effects study, while the low-dose ones were analyzed for further building the precise correlation between radiation dose and compound concentrations. The method and experimental design were described in sections 3.3 and 3.4. Irradiated oils were then separated using the same methods as the original oils and characterized by GC-MS as well.

3.1 Samples information

3.1.1 Oil/condensate samples from Tarim Basin, NW China

Ten oil/condensate samples were collected from the cratonic region of the North and Central Tarim uplift at intervals between 3980 m and 6828 m present depth. The well locations of the collected oils are shown in Fig. 2.1.

Table 3.1 Table of Tarim sample information

(O: Ordovician; T: Triassic; C: Carboniferous. API = [141.5/specific gravity – 131.5])

Code	Well	Formation	Depth (m)	API (°)	Type
T1	Ha6C	O	6788.32	24.0	Oil
T2	TZ62	O	4729.25	41.1	Oil
T3	Ha15-2	O	6578.665	23.6	Oil
T4	TZ16-7	C	3980-4220	32.1	Oil
T5	LN14	T	4430-4436.9	28.4	Oil
T7	Ha13-1c	O3l	6643-6828.6	43.2	Oil
T8	JF134	TII	4409.6-4419	30.6	Oil
T10	LG16-2	O	5478-5505	32.4	Oil
T6	LN57	T	4342.9	53.2	Cond.
T9	TZ242	O	4471-4622	46.0	Cond.

These oils vary considerably in physical properties, ranging from heavy oil to condensate with an API gravity range of 24.0–53.2° at 20 °C (Table. 3.1). The wide variation also extends to sulfur content of 0.02–2.65% and wax content of 5.2–18.0% (Table 3.2), which spans most of the maturity window for oil generation from marine source rocks.

The bulk compositional fractions of these oils/condensates, which were determined by Iatroscan analysis, display a relatively wide range of saturated hydrocarbon, aromatic hydrocarbon, resins (Polar 1) and asphaltenes (Polar 2) concentrations in the range 46.8–79.1%, 15.3–32.7%, 1.3–5.7% and 1.4–28.5%, respectively (Table 3.2).

Table 3.2 Table of Tarim sample bulk composition

Code	S%	Wax%	% Sat	% Aro	% Polar 1	% Polar 2
T1	0.59	7.7	59.6	32.7	2.9	4.9
T2	0.21	7.4	79.1	17.9	1.7	1.4
T3	0.81	6.7	53.9	26.5	4.1	15.6
T4	0.35	6.0	46.8	24.7	3.9	24.7
T5	0.92	6.2	47.1	20.0	4.5	28.5
T7	0.18	5.4	75.5	20.4	1.6	2.5
T8	2.65	8.2	61.7	21.3	5.7	11.4
T10	0.46	18.0	75.3	21.8	1.3	1.6
T6	0.02	–	78.7	15.3	2.2	3.8
T9	0.15	5.2	74.3	21.7	1.8	2.2

These 10 oil samples from the Tarim Basin were all selected to be irradiated under high-dose γ -ray (50–4000 kGy), and characterized with GC-MS as well as other analyzing tools in order to understand the variations in radiolysis markers associated with their original oil chemistry and to build the correlation between radiolysis markers and irradiation dose.

3.1.2 Oil samples from North Sea and Barents Sea

Analyses were completed for 23 crude oil samples (Table 3.3) that were collected from the North Sea and Barents Sea regions at depths around 2000 m. Their molecular character was determined using GC-MS.

After the investigation of different molecular character of these oils, 7 representatives (Table 3.4) were selected to be irradiated under low-dose γ -radiation.

Table 3.3 Table of North Sea and Barents Sea sample information

Code	Field	Area
N1	Apollo	North Sea-Utsira High
N2	Apollo	North Sea-Utsira High
N3	Edvard Grieg	North Sea-Utsira High
N4	Edvard Grieg	North Sea-Utsira High
N5	Edvard Grieg	North Sea-Utsira High
N6	Rolvsnes	North Sea-Utsira High
N7	Rolvsnes	North Sea-Utsira High
N8	Rolvsnes	North Sea-Utsira High
N9	Johan Sverdrup	North Sea-Utsira High
N10	Johan Sverdrup	North Sea-Utsira High
N11	Johan Sverdrup	North Sea-Utsira High
N12	Johan Sverdrup	North Sea-Utsira High
N13	Johan Sverdrup	North Sea-Utsira High
N14	Johan Sverdrup	North Sea-Utsira High
N15	Luno II	North Sea-Utsira High
N16	Luno II	North Sea-Utsira High
N17	Luno II	North Sea-Utsira High
N18	Luno II	North Sea-Utsira High
N19	Luno II	North Sea-Utsira High
N20	Luno II	North Sea-Utsira High
N21	Brynchild	North Sea-Brynchild
B1	Gohta	Barents Sea
B2	Alta	Barents Sea

Besides these 2 sample sets, a North Sea light oil (NSLO) and an Alberta Heavy Oil (AHO) were irradiated under a larger dose range (50–10000 kGy) and were also investigated for their compound concentrations to determine the amount of destruction and to construct the basic age dating method (discussed in Chapter 4).

3.2 Separation of hydrocarbon fraction

The original and irradiated oil samples were fractionated before gas chromatography – mass spectrometry (GC-MS) analysis based on a modified Trevor Bastow method (Bastow et al., 2007). In brief, 50 mg of oil is de-asphalted by solid phase extraction (SPE) procedure (Bennett and Larter, 2000) with Florisil® magnesium silicate cartridges and then loaded on a silica gel (0.6 g, 70-230 mesh) column, pre-washed with pentane. The saturated hydrocarbon compound fraction is collected by elution of 2 mL of pentane, using small aliquots (40 × 50 µl), while the aromatic hydrocarbon compound fraction is collected by eluting 2 mL of dichloromethane, then 2 mL of isopropyl alcohol (IPA). A set of internal standards is added to the oil before the de-asphalting

step to allow quantitative analysis. This internal standard set contains squalane, adamantane-d16, cholestane-d4, phenyldodecane-d30, naphthalene-d8, phenanthrene-d10 and 1,1-binaphthyl for the quantification of 200+ individual compounds in each sample.

3.3 Characterization method

An Agilent GC-MS Instrument (7890B GC and 5977 MS), with a HP-5MS capillary column (30 m × 0.25 mm × 0.25 μm), was used for the analysis of both saturated and aromatic compound fractions. The temperature program for the GC column included 5 min at 40°C, followed by a 4°C/min ramp up to 325°C, then an isothermal hold at 325°C for 15 minutes. Helium was used as carrier gas, at a flow rate of 1.0 mL/min. The mass spectrometer was set to perform, simultaneously, scan and selected ion monitoring (SIM) modes. After analysis on the GC-MS, the peak areas of target compounds were integrated by using ChemStation software and the concentrations were calculated by comparing integrated peak areas with the related internal standard peak area.

The ions monitored in the saturated hydrocarbon fraction were: m/z 85 (normal alkanes); m/z 123 (bicyclic sesquiterpane); m/z 191 (terpanes); m/z 217 (steranes) and m/z 136, 135, 149, 163, 177 (adamantanes). The ions monitored in the aromatic hydrocarbon fraction were: 128 (naphthalene); m/z 142 (C1-naphthalenes); m/z 156 (C2-naphthalenes); m/z 170 (C3-naphthalenes); m/z 178 (phenanthrene); m/z 184 (C4-naphthalenes and dibenzothiophene); m/z 192 (C1-phenanthrenes); m/z 198 (C5-naphthalenes and C1-dibenzothiophenes); m/z 206 (C2-phenanthrenes); m/z 212 (C2-dibenzothiophenes); m/z 231 (triaromatic steroid hydrocarbons) and m/z 253 (monoaromatic steroid hydrocarbons).

The list of compounds identified by GC-MS, sample chromatograms and molecular structures are shown in APPENDIX 1. A total of 202 compounds were selected, integrated and calculated for their concentration.

3.4 γ -ray irradiation experiments

This is not the first time that irradiation experiments were conducted on crude oils. In a previous study, Frolov et al. (1998) suggested that γ -bombardment can be used to simulate processes involved in natural radiolysis, they investigated the crude oil samples irradiated by Cobalt-60 (^{60}Co) gamma rays with irradiation doses ranging from 7 up to 1200 Mrad (70–12000 kGy) to study the olefins. The olefins were found to be generated with increasing concentrations in the proportion with the irradiation dose.

In our study, high-dose (50-10000 kGy) irradiation experiments were conducted at Instituto Nacional de Investigaciones Nucleares in Mexico on hundreds of crude oil samples from Tarim Basin, North Sea and Alberta Basin, followed by low-dose (0–200 kGy) irradiation experiments on selected crude oils from North Sea and Barents Sea (Table 3.4) irradiated in the Health Science Irradiators at the University of Calgary.

Table 3.4 List of all samples irradiated under high-dose and low-dose

Codes	Location	Number of samples	Radiation range (kGy)
Ha 6C O	Tarim Basin	10	50–4000
TZ 62 O	Tarim Basin	10	50–4000
Ha 15-2 O	Tarim Basin	12	50–4000
TZ 16-7 C	Tarim Basin	10	50–4000
LN 14 T	Tarim Basin	10	50–4000
LN 5 T1	Tarim Basin	10	50–4000
Ha13 1C O3L	Tarim Basin	10	50–4000
JF 134 T II	Tarim Basin	10	50–4000
TZ 242 O	Tarim Basin	6	50–4000
LG 16-2 O	Tarim Basin	10	50–4000
NSLO	North Sea	29	50–10000
AHO	Alberta Basin	39	50–10000
N1	North Sea	17	5–200
N6	North Sea	17	5–200
N12	North Sea	15	5–200
N14	North Sea	12	5–200
N15	North Sea	18	5–200
N21	North Sea	15	5–200
B2	Barents Sea	15	5–200

The purpose of conducting high-dose irradiation experiments was to investigate the basic radiolysis effects and mechanisms, as well as developing the method to build a functional correlation between major compounds and radiation dose. While, the actual dose rate of natural radiation in petroleum reservoir are quite low (e.g. around 2160 Gy/Ma for a typical shale, calibrated internally by PRG), it is necessary to conduct low-dose irradiation experiments to study the more natural-like radiolysis process and help to understand the crude oil radiolysis mechanisms in reservoir.

3.4.1 High-dose irradiation experiment

3.4.1.1 Radioactive isotope

The radioactive isotope Cobalt-60 (^{60}Co), with a half-life of about 5.3 years and a stable decay product of Nickel-60 (^{60}Ni), was used in the high-dose irradiation experiment. ^{60}Co decays by beta decay to ^{60}Ni and the activated nickel nucleus emits two gamma rays with energies of around 1.17 and 1.33 MeV (Fig. 3.1). In this experiment, the irradiation dose ranged from 50 to 10000 kGy, with an irradiation dose rate around 14.23 kGy/h (~10,000 kGy/month).

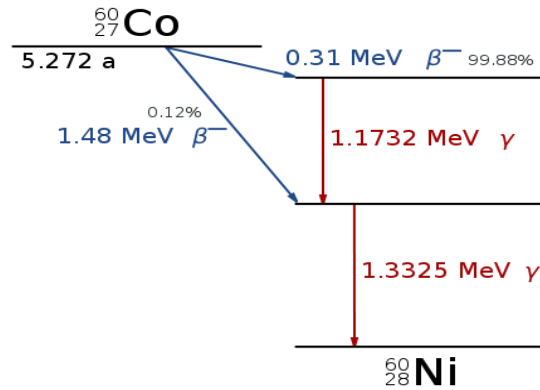


Fig. 3.1 The decay scheme of ^{60}Co

3.4.1.2 High-dose irradiated sample

For the high-dose irradiation experiment, 138 oil samples in total were sealed in 5 ml ampoules under argon (room temperature, in oxygen free conditions). Among them, subsamples of 10 Chinese Tarim oils were irradiated with doses ranging from 50–4000 kGy. Besides, 2 crude oils from the Alberta Basin and the North Sea area were subsampled and irradiated under a larger range (50–10000 kGy) for correlation and method development.

3.4.2 Low-dose irradiation experiment

3.4.2.1 Radioactive isotope

The radioactive isotope caesium-137 (^{137}Cs), with a half-life of about 30.2 years and a stable decay product of barium-137 (^{137}Ba) (0.662 MeV) (Fig. 3.2), was used in the low-dose irradiation experiment. ^{137}Cs decays by beta decay to ^{137}Ba and the activated barium nucleus emits one gamma ray with an energy of around 0.66 MeV (Fig. 3.2). In this experiment, the irradiation dose ranged from 0–200 kGy, with an irradiation dose rate around 0.171 kGy/h (120 kGy/month).

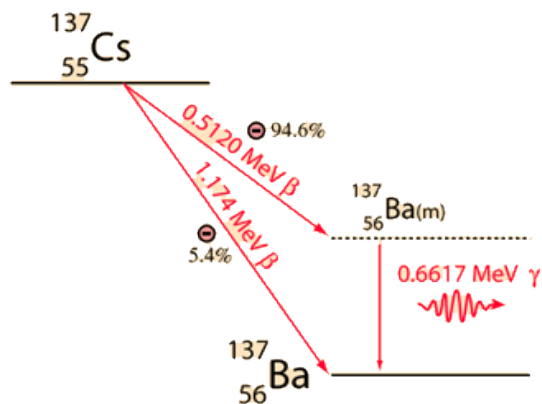


Fig. 3.2 The decay scheme of ^{137}Cs

3.4.2.2 Low-dose irradiated sample

For the low-dose irradiation experiments, 7 crude oil samples from North Sea and Barents Sea (listed in Table 3.4) were selected based on their different location and geochemical characteristics. These samples were sealed in 1 ml ampoules (Fig 3.3a) under argon (room temperature, in oxygen free conditions), divided into 138 subsamples, and irradiated under specific doses ranging from 2.70 to 215.94 kGy.

3.4.2.3 Experiment design

The purpose of conducting the low-dose experiments was to mimic the radiolysis process in natural reservoirs and help to better understand the natural radiolysis mechanisms. To build a more precise and realistic correlation between radiolysis proxies and irradiation dose, every subsample was designed to be irradiated under a specific dose with a general target distribution (basically targeted at 5 kGy, 10 kGy, 20 kGy, 40 kGy, 60 kGy, 80 kGy, 100 kGy, 125 kGy, 150 kGy, 200 kGy, with triplicates for 20 kGy and 80 kGy for error analysis).

A 3-layer foam cylinder, with 48 sample spots in total (Fig. 3.3c, d), was set with sample rotation mode off in the Health Science Irradiator (Fig. 3.3b). The samples were irradiated simultaneously with a specific dose rate for each spot (dose rate calibration described in 3.4.3.4), and the irradiation dose was monitored and controlled for each sample based on calibrated dose rates. The samples were removed once the target dose was reached, and new samples loaded into the empty spots to make the device run at its highest efficiency.

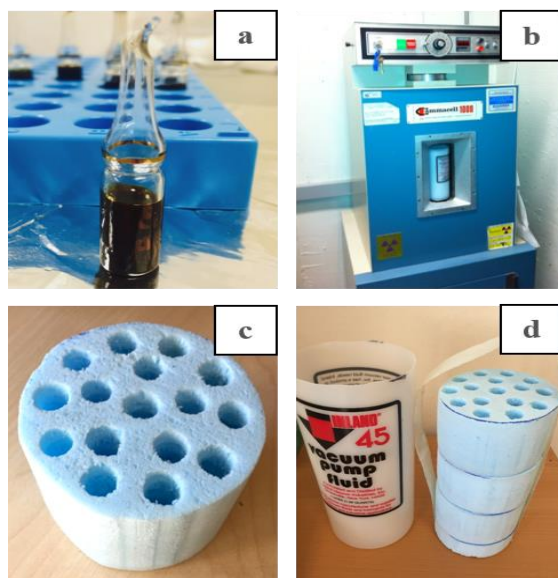


Fig. 3.3 Low-dose irradiation experiment design

3.4.2.4 Dose rate calibration

A 2 minute ^{137}Cs irradiation test was performed to evaluate the dose rate at the different sample positions. In this test, a water based gel was used to mimic the oil in each sample spot position. GAFCHROMIC EBT3 radiochromic dosimetry film (Fig. 3.4a) (Villarreal and Khan, 2014) was used to calibrate the dose rate. According to the manufacturer, the film is comprised of a single active layer, nominally $27\ \mu\text{m}$ thick, containing the active component, marker dye, stabilizers, and other additives giving the film its low-energy dependence.

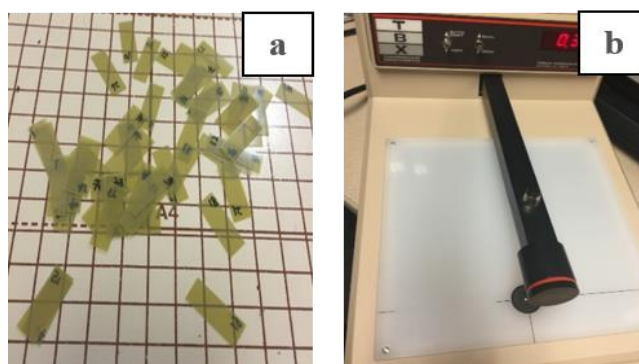
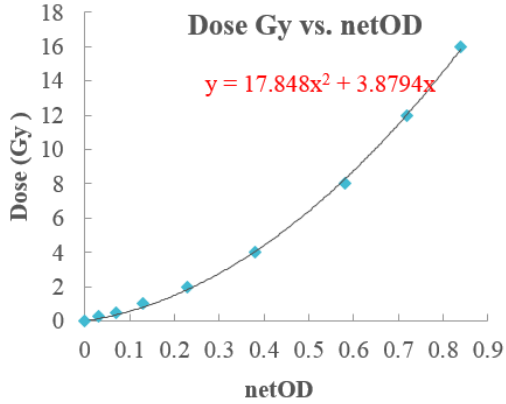


Fig. 3.4 Dose rate calibration method

The EBT3 film was cut into small pieces ($\sim 0.5 \times 2\ \text{cm}$) and inserted into the gel-filled spots. The 2-minute test was repeated three times, resulting in three independent irradiations and, therefore, 3 net Optical Density (netOD) evaluations for every beam energy and batch. The netOD for all the EBT3 film pieces was obtained using a single point with a light densitometer (Fig. 3.4b).

A calibration response was obtained using a 6 MV x-ray clinical beam. This calibration covered the 0-16 Gy dose range (Fig. 3.5).



C group	OD-TBX	netOD	Total dose (Gy)	Dose rate (Gy/min)
1	0.92	0.66	10.33	5.17
2	0.73	0.47	5.77	2.88
3	0.62	0.36	3.71	1.85
4	0.55	0.29	2.63	1.31
5	0.52	0.26	2.22	1.11
6	0.52	0.26	2.22	1.11
7	0.56	0.3	2.77	1.39
8	0.61	0.35	3.54	1.77
9	0.74	0.48	5.97	2.99
10	0.9	0.64	9.79	4.9
11	0.8	0.54	7.3	3.65
12	0.66	0.4	4.41	2.2
13	0.61	0.35	3.54	1.77
14	0.59	0.33	3.22	1.61
15	0.66	0.4	4.41	2.2
16	0.65	0.39	4.23	2.11

Fig. 3.5 Correlation between irradiation dose vs. netOD (net optical density) and calibration results for Layer C

This dose calibration was used to evaluate the total dose at all the spots within the sample holder. Dose rate for every spot in each layer was derived by dividing the total estimated dose (Gy) by the irradiation time (minutes). The example dose rate results for Layer C (bottom layer in Fig. 3.3d) are shown above.

Chapter Four: Basic Radiolysis Effects and Mechanism

The high dose irradiation experiments were conducted on one Alberta Heavy Oil (AHO) sample and one North Sea light oil (NSLO) sample under room temperature in sealed ampoules with ^{60}Co γ -ray (described in 4.4). In total, 29 NSLO subsamples and 39 AHO subsamples (including duplicates) were irradiated under doses ranging from 50 kGy to 10000 kGy and analyzed using GC-MS. As shown in Table 4.1, the experiments were conducted in two phases with different dose ranges, and were combined as relatively complete dose series covering both low-dose and high-dose runs. The GC-MS data interpretation for these two oils was used for the basic assessment during the method development.

Table 4.1 Radiation doses (kGy) of NSLO and AHO samples irradiated in phases 1 and 2

Oil sample	Radiation doses (kGy)
NSLO (phase 1)	50, 40, 800, 1200, 1500, 2000, 2400, 2800, 3000, 3200, 3600, 7600, 8400, 9600
NSLO (phase 2)	50, 100, 200, 400, 4400, 5600, 6000, 6800, 8800, 10000
AHO (phase 1)	4000, 4400, 4800, 5000, 5200, 5600, 6000, 6400, 6800, 7000, 7200, 9200, 10000
AHO (phase 2)	50, 100, 200, 400, 800, 1200, 1600, 2000, 2400, 3000, 3600, 4400, 5600, 6800, 7600, 8800, 10000

4.1 Compound destruction under high-dose irradiation (50-10000 kGy)

In this study, over 200 hydrocarbon compounds and sulfur compounds typically used in petroleum geochemistry assessment were quantified in irradiated AHO and NSLO samples. The most obvious radiation effects are concentration decreases of individual crude oil components. After plotting versus the radiation dose, the compound concentration for AHO and NSLO generally shows a significant, near-linear decrease with increasing radiation dose.

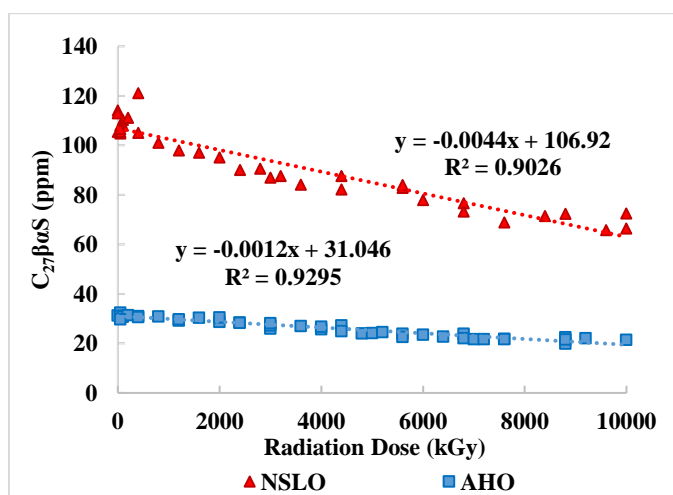


Fig. 4.1 Plot showing the variation in concentration of $\text{C}_{27} 10\beta(\text{H}), 13\alpha(\text{H}) 20\text{S}$ diasterane ($\text{C}_{27}\beta\alpha\text{S}$) with radiation dose (kGy) for NSLO and AHO samples

The C₂₇ 10β(H),13α(H) 20S diasterane (C₂₇βαS), for example, clearly shows destruction (Fig. 4.1) as a function of radiation dose, for both AHO and NSLO (with a slope around -0.0044 (Δppm/ΔkGy) for NSLO samples and -0.0012 (Δppm/ΔkGy) for AHO samples). The R² value (r is the correlation coefficient; r² is the coefficient of determination) of both trendlines were over 0.9, indicating the general reliability of these linear correlations and the concordancy of data.

Previous studies (e.g. Frolov et al., 1998) suggested that crude oils are very reactive under high radiation doses. This is verified from the above “compound loss” phenomenon in which the compounds in crude oils are altered by the irradiation. For a general discussion, the initial concentration versus the degradation slope (Δppm/ΔkGy) for 202 compounds in NSLO and AHO samples were plotted in Fig. 4.2. The compounds are classified into different groups including: normal and isoprenoid alkanes (alkanes); bicyclic sesquiterpanes (BSTs); tricyclic terpanes (TTs) and hopanes; steranes (STs); adamantanes (ADs); naphthalene and alkylnaphthalenes (Naphthalenes); phenanthrene and alkylphenanthrenes (Phenanthrenes); aromatic sulfur compounds (DBTs); aromatic steroid hydrocarbons (TAS+MAS).

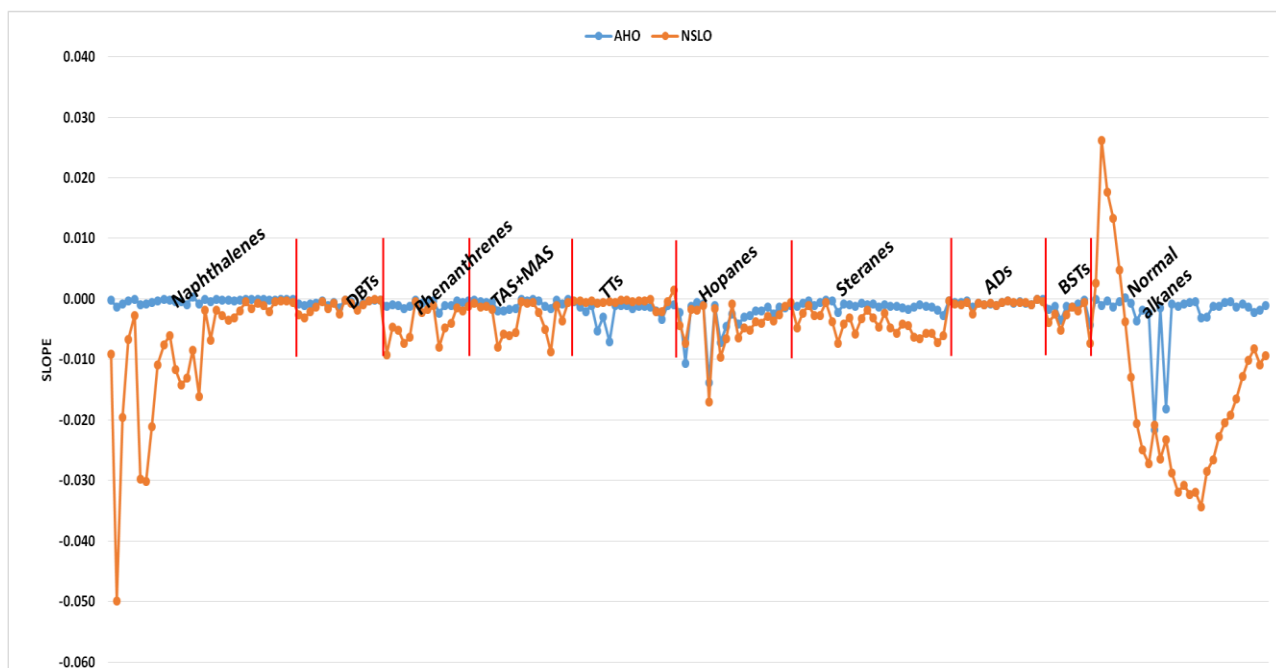


Fig. 4.2 Plot of initial concentration versus the degradation slope (Δppm/ΔkGy) for investigated saturated and aromatic hydrocarbons in high-dose (0–10000 kGy) irradiated NSLO and AHO samples

According to Fig. 4.1, it could be inferred that the destruction rate might be affected by original concentration for every compound (further discussed in following sections). This could also explain the big variation of compound destruction rates for NSLO and AHO (Fig.4.2). The alkylnaphthalenes (C₀₋₅ naphthalenes), for example, have much higher original concentrations (total concentration around 10000 ppm) in NSLO compared with that of AHO (total amount around 2000 ppm), the degradation slopes of each compound were also lower, correlating to higher destruction rates.

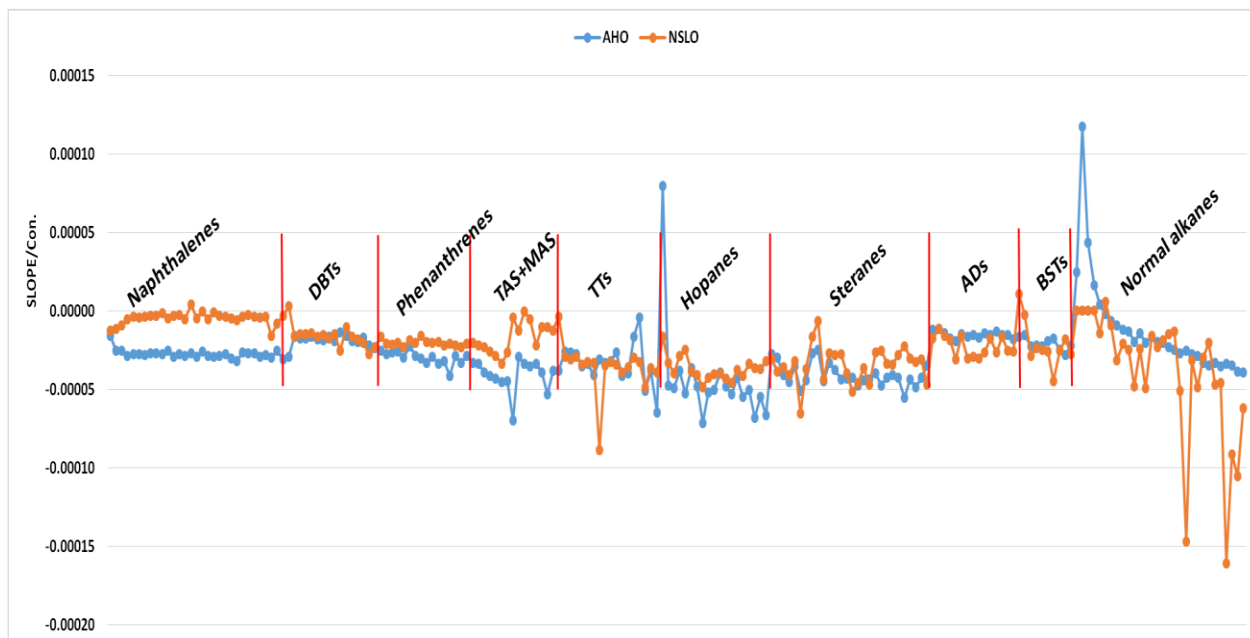


Fig. 4.3 Plot of normalized slopes (normalized concentration vs. dose) for investigated saturated and aromatic hydrocarbons in high-dose (0–10000 kGy) irradiated NSLO and AHO samples

After normalization to the original compound concentration, the destruction trends for NSLO and AHO samples became more consistent (Fig. 4.3), allowing the existing difference of destruction rates to be affected in terms of the oil matrix and other factors.

To have a more thorough understanding of radiolysis effects, the concentration and radiation dose correlation of major biomarkers and hydrocarbon compounds in crude oil will be discussed by different compound classes in the following sections. The compound classes were further divided into three levels by the data consistency (value of R^2 , shown in Table 4.2), indicating good to poor correlation statistics of compound destruction as a function of radiation dose. The data of Level 1 compounds, which generally exhibit very good consistency, could be

considered as good indicators for oil radiolysis and will be the focus of discussion. Noticeably, this category could only roughly generate a structure for the following discussion and could not be considered as the category of radiolysis indicator level.

Table 4.2 Compound type category

Range of R ²	Compound type
Level 1: 0.7–0.9 (good)	tricyclic terpanes and hopanes; phenanthrene and alkylphenanthrenes; triaromatic steroid hydrocarbons
Level 2: 0.5–0.7 (medium)	steranes, naphthalene and alkyl naphthalenes; dibenzothiophene (DBTs); Monoaromatic steroid hydrocarbons
Level 3: <0.5 (poor)	adamantanes; normal and isoprenoid alkanes; bicyclic sesquiterpanes

For each class, the source and chemical structure of major compounds as well as their distribution on GC-MS chromatograms are firstly provided as general geochemical background of the investigated species. Then, the concentration variations with increasing radiation doses of typical compounds are discussed, aiming at building radiolysis correlations among different compound classes as well as selecting "radio-markers" among the investigated compounds. Besides, the variation of degradation slope and normalized slope for individual compounds in every class were also plotted, in order to investigate their basic radiolysis behavior and potential influencing factors.

4.2 "Level 1" compounds

4.2.1 Tricyclic terpanes (TTs) and hopanes (PTs)

The tricyclic terpanes (TTs) are saturated hydrocarbons and are extensively found in crude oils, they occur as a pseudo-homologous series ranging from C₁₉ to as high as C₅₄. They are commonly recognized up to the C₃₀ compounds because the higher members of the series are often masked by hopanes in the m/z 191 mass chromatogram (Zhang and Huang, 2005). The biological source for tricyclic terpanes is still not clear. Ourisson et al. (1982) suggested that the tricyclic terpanes have been possibly sourced from bacterial (prokaryotic) membrane lipids. Aquino et al. (1983) indicated that tricyclic terpanes are normally associated with marine source. However, their ubiquitous occurrence in sediments and oils of varying ages demonstrates that additional sources must also exist (Peters et al., 2005).

Hopanoid compounds (pentacyclic triterpanes, PTs) ranging from C₂₇ to C₃₅ are ubiquitous components of crude oils and have been proven to be useful biomarkers and widely used to track

the depositional environment and the thermal maturity of sediments and oils. Hopanes originate from precursors in bacterial membranes (Ourisson et al., 1979).

The identified C₁₉₋₃₀ tricyclic terpanes and hopanes for NSLO and AHO (Table A1.3) are both illustrated in m/z 191 mass chromatograms in Fig. 4.4. Compared with NSLO, the tricyclic terpanes compounds of AHO were removed due to strong biodegradation.

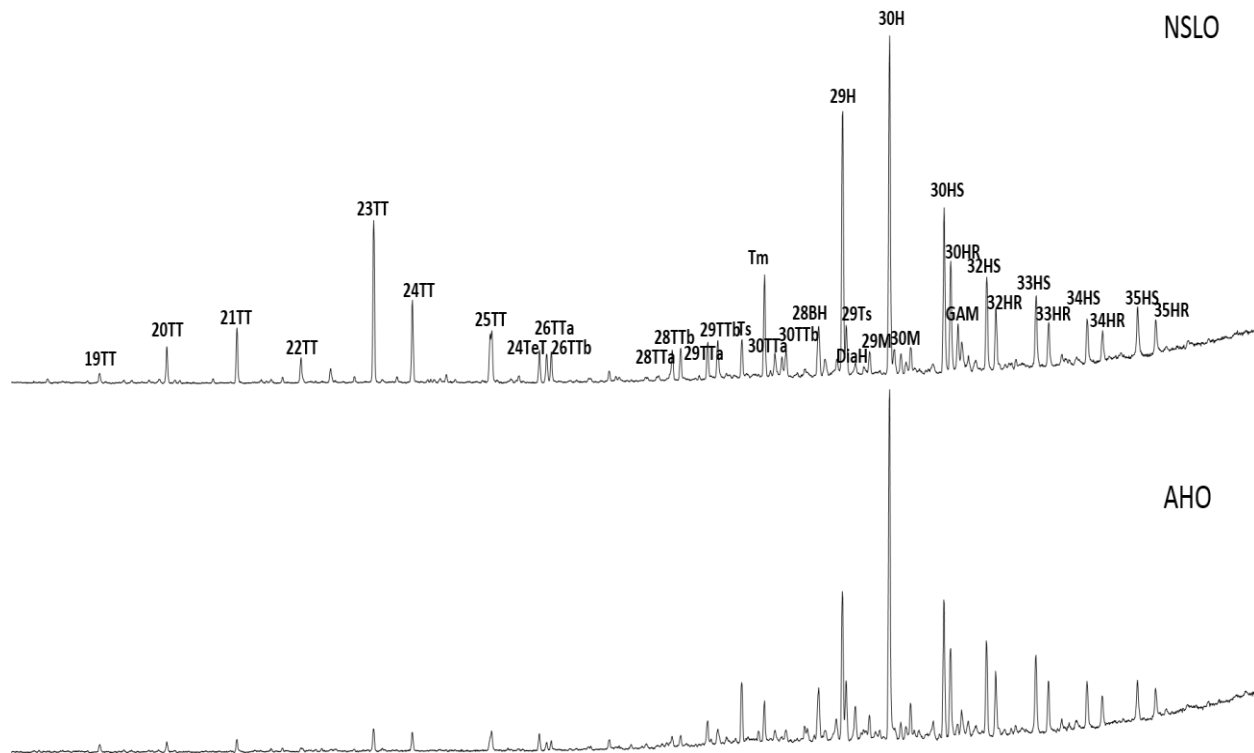


Fig. 4.4 Distribution of tricyclic terpanes and hopanes shown in GC-MS chromatogram m/z 191 of the saturated hydrocarbon fraction of non-irradiated NSLO and AHO samples

The sum of the concentration of the tricyclic terpanes were calculated from C₁₉ to C₂₆ compounds. Significant variations of concentration exist, changing from 195 to 135 ppm for NSLO and from 642 to 375 ppm for AHO (Fig. 4.5). A relatively larger variation occurs in AHO (with a slope around -0.023 ($\Delta\text{ppm}/\Delta\text{kGy}$)). The NSLO, with lower original concentration of tricyclic terpanes, displayed a more steady destruction trend compared with the heavier oil.

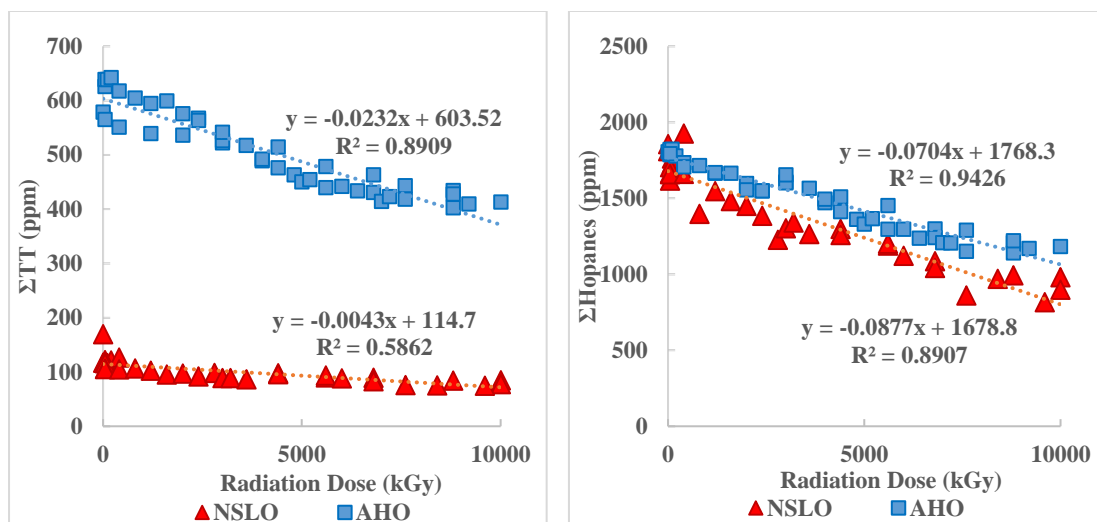
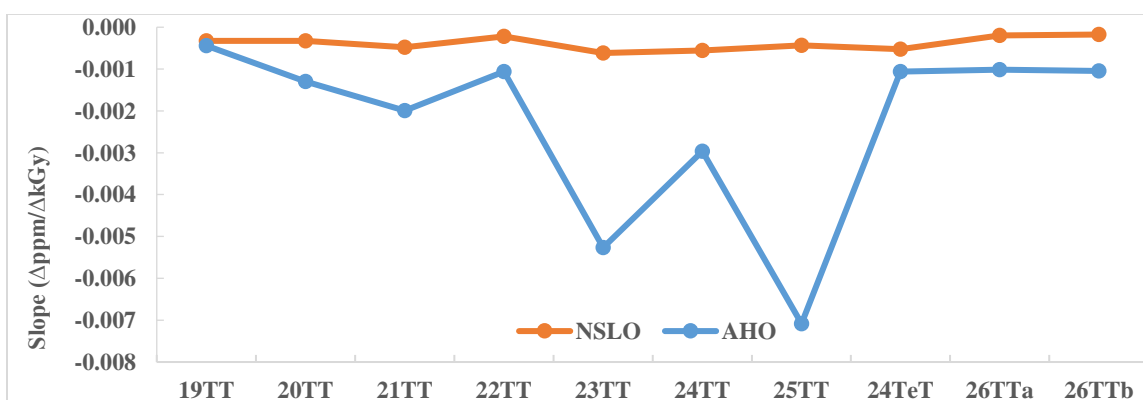


Fig. 4.5 Plots showing the variation in concentrations of tricyclic terpanes and pentacyclic terpanes (hopanes) with radiation dose (kGy)

As Fig. 4.5 shows, with increasing radiation dose, the concentration of hopanes decreases linearly from 1856 to 816 ppm for NSLO (with a slope around -0.088 ($\Delta\text{ppm}/\Delta\text{kGy}$)) and from 1823 to 1070 ppm for AHO (with a slope around -0.070 ($\Delta\text{ppm}/\Delta\text{kGy}$)). The destruction for NSLO is slightly faster than that of AHO.

The tricyclic terpanes are within the slope range of -0.0052 ($\Delta\text{ppm}/\Delta\text{kGy}$) to -0.0007 ($\Delta\text{ppm}/\Delta\text{kGy}$) for NSLO and -0.007 ($\Delta\text{ppm}/\Delta\text{kGy}$) to -0.0005 ($\Delta\text{ppm}/\Delta\text{kGy}$) for AHO. As indicated by Fig. 4.6, the radiolysis of TTs compounds are generally slow in NSLO, which could be inferred to be correlated to the very low original concentration (Fig. 4.5). The outstanding points of AHO slope (e.g. 23TT, 24TT, 25TT) are considered to be correlated to the relatively higher original concentration. The same rule was also shown in the degradation slope for hopanes in NSLO (-0.017 ($\Delta\text{ppm}/\Delta\text{kGy}$) to -0.0005 ($\Delta\text{ppm}/\Delta\text{kGy}$)) and AHO (-0.013 ($\Delta\text{ppm}/\Delta\text{kGy}$) to -0.0005 ($\Delta\text{ppm}/\Delta\text{kGy}$)).



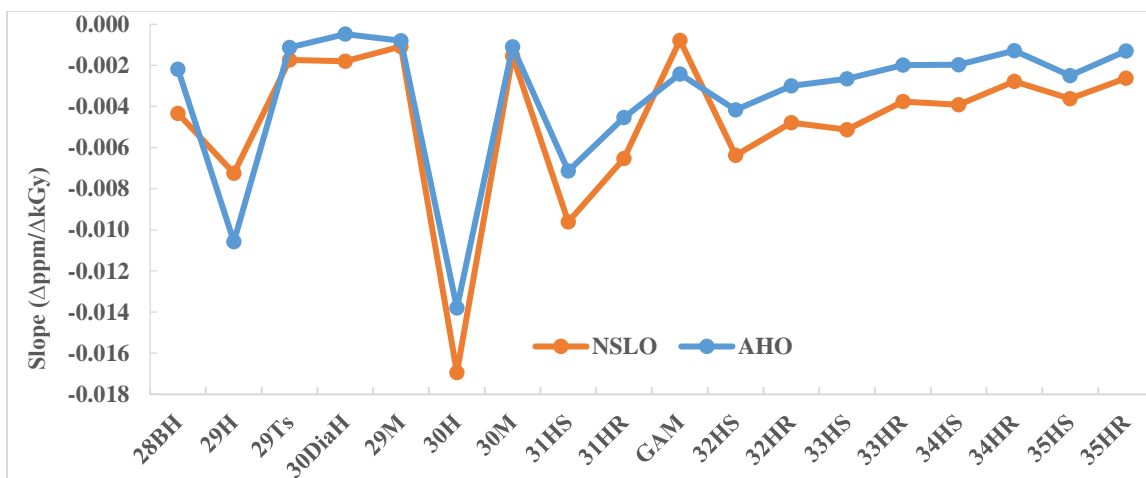
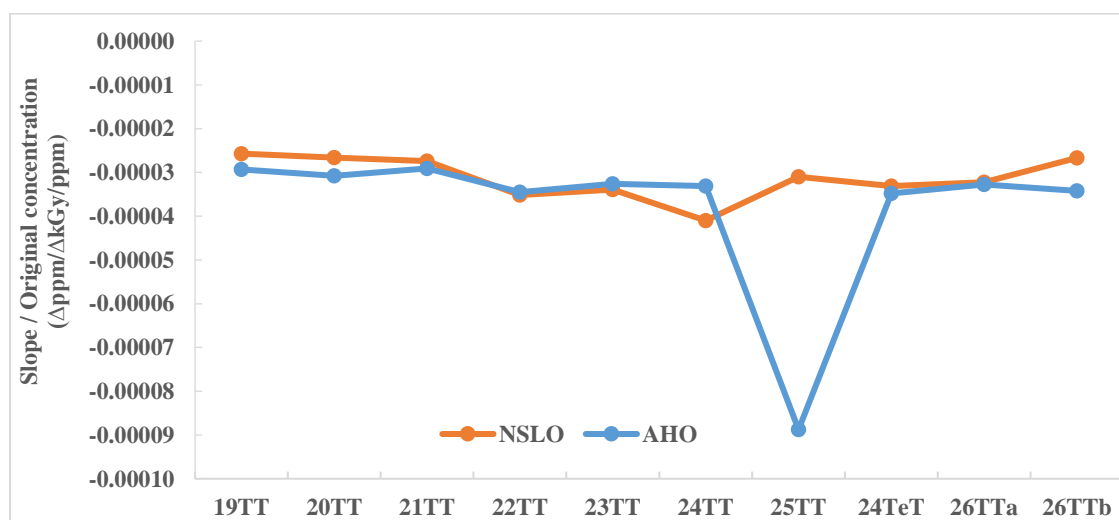


Fig. 4.6 Plot of degradation slopes ($\Delta\text{ppm}/\Delta\text{kGy}$) for tricyclic terpanes and pentacyclic terpanes (hopanes) in high-dose (0–10000 kGy) irradiated NSLO and AHO samples

The normalized slope plots (Fig. 4.7), which eliminated the effect of original compound concentration, indicate that the radiolysis of tricyclic terpanes and hopanes generally had similar rates for both oils. Some of the highlighted points such as C_{25} tricyclic terpene (25TT), C_{35} $17\alpha(\text{H})$, $21\beta(\text{H})$ 22R homohopane (35HR/S) might be the result of sensitivity variation among individual compounds.



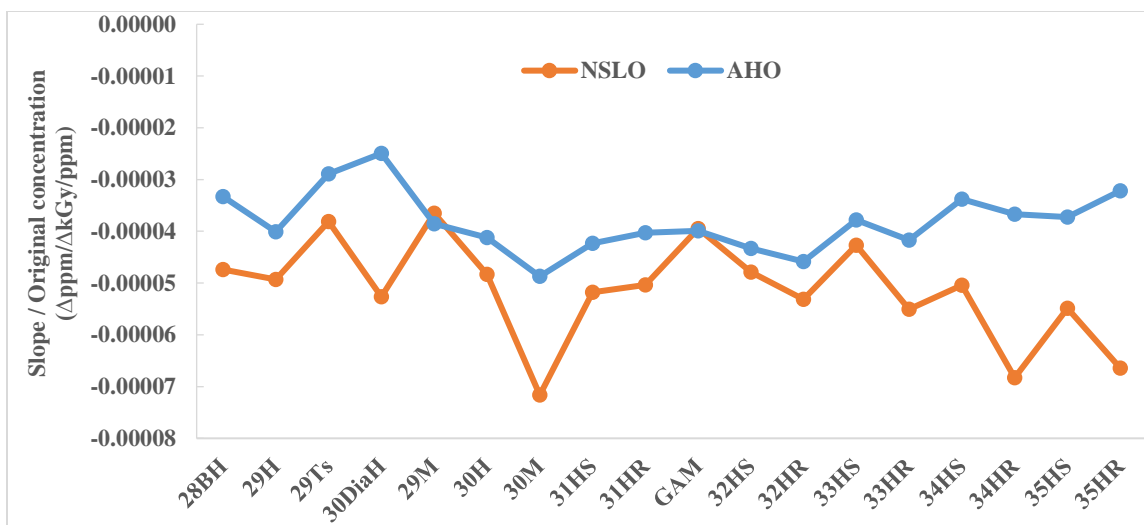


Fig. 4.7 Plot of normalized slopes (normalized concentration vs. dose) for tricyclic terpanes and pentacyclic terpanes in high-dose (0–10000 kGy) irradiated NSLO and AHO samples

4.2.2 Phenanthrene and alkylphenanthrenes (P)

Phenanthrene is a polycyclic aromatic hydrocarbon composed of three fused benzene rings (Fig. 4.8). The distributions of phenanthrene and alkylated phenanthrenes have been widely studied as indicators of thermal maturity in crude oils and source rock extracts (Radke, 1988; Garrigues et al., 1988).

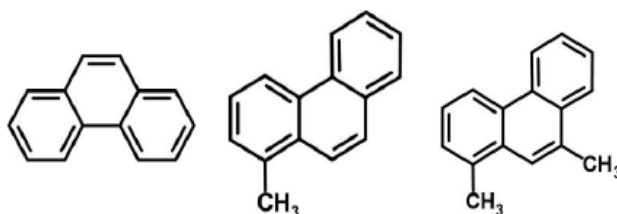


Fig. 4.8 Structure of phenanthrene and C₁₋₂ alkylphenanthrenes

The distributions of methylphenanthrene and C₂-alkylphenanthrenes are shown in Fig. 4.9 and identified compounds are listed in Table A2.2.

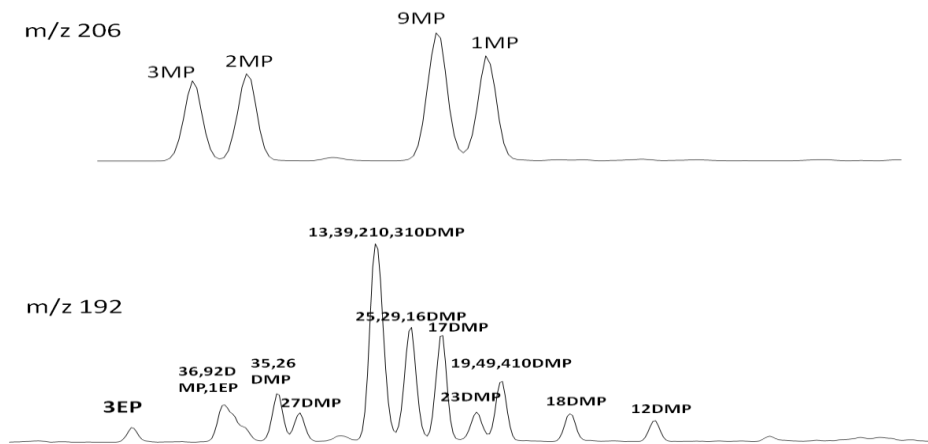


Fig. 4.9 Distribution of alkylphenanthrenes shown in GC-MS chromatogram m/z 192, 206 of the aromatic hydrocarbon fraction of non-irradiated NSLO samples

As Fig. 4.10 shows, the concentration of phenanthrene and sum C₁₋₂ alkyl-phenanthrene (methyl-, dimethyl-, ethyl-phenanthrene) compounds for NSLO decrease dramatically with increasing radiation dose. The phenanthrene decreases from 398 to 231 ppm for NSLO (with a slope around -0.010 (Δppm/ΔkGy)) and from 73 to 57 ppm for AHO (with a slope around -0.001 (Δppm/ΔkGy)). The C₁₋₂ alkyl-phenanthrene decrease from 1919 to 1107 ppm for NSLO (with a slope around -0.047 (Δppm/ΔkGy)) and from 578 to 424 ppm for AHO (with a slope around -0.008 (Δppm/ΔkGy)). The AHO samples, with low abundance of phenanthrenes compounds, exhibiting a stable state irradiated under high-dose irradiation (Fig. 4.10).

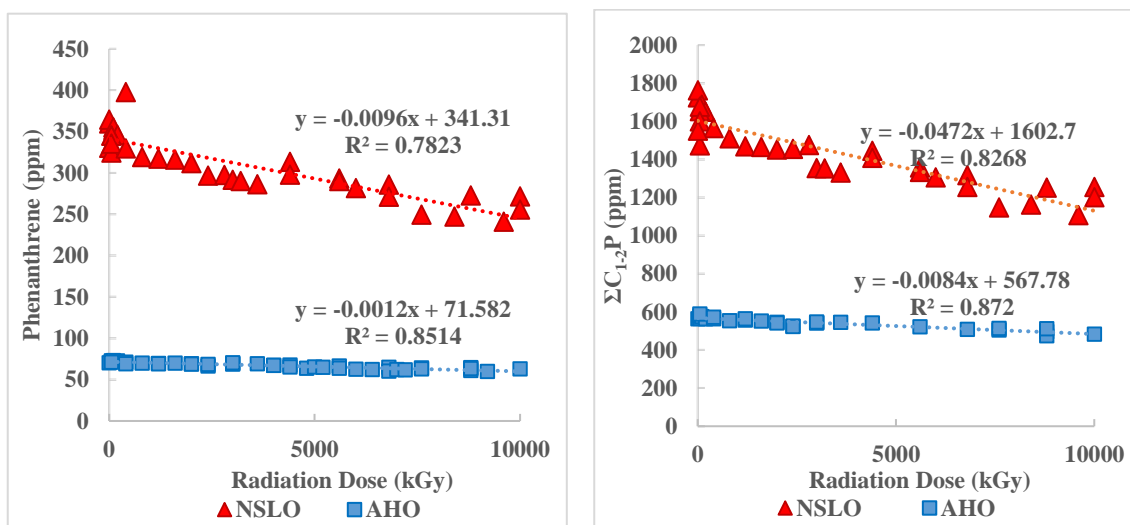


Fig. 4.10 Plots showing the variation in concentrations of phenanthrenes and C₁₋₂ alkyl-phenanthrenes with radiation dose (kGy)

The individual phenanthrene and its alkyl substituted compounds are within the slope range of -0.0097 ($\Delta\text{ppm}/\Delta\text{kGy}$) to -0.0006 ($\Delta\text{ppm}/\Delta\text{kGy}$) for NSLO and -0.0034 ($\Delta\text{ppm}/\Delta\text{kGy}$) to -0.0001 ($\Delta\text{ppm}/\Delta\text{kGy}$) for AHO (Fig. 4.11).

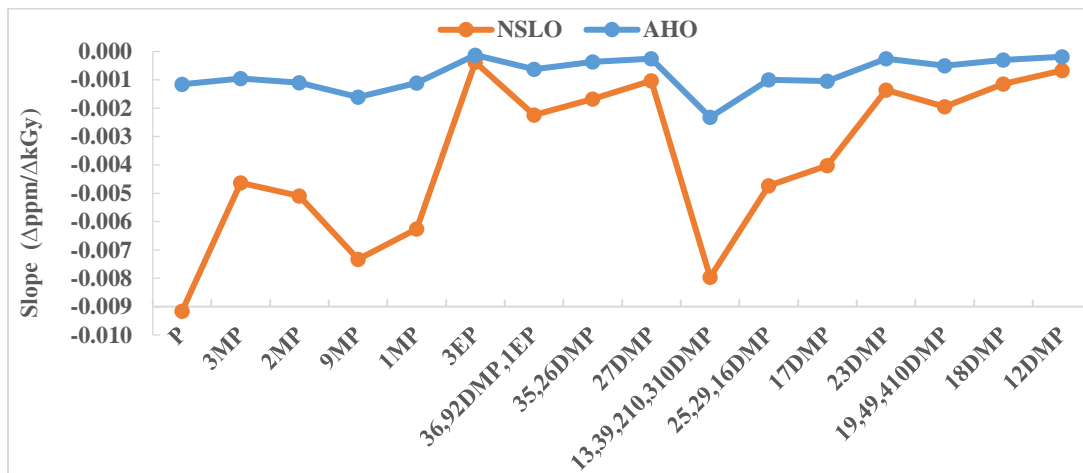


Fig. 4.11 Plot of degradation slopes ($\Delta\text{ppm}/\Delta\text{kGy}$) for phenanthrenes and C_{1-2} alkyl-phenanthrenes in high-dose (0–10000 kGy) irradiated NSLO and AHO samples

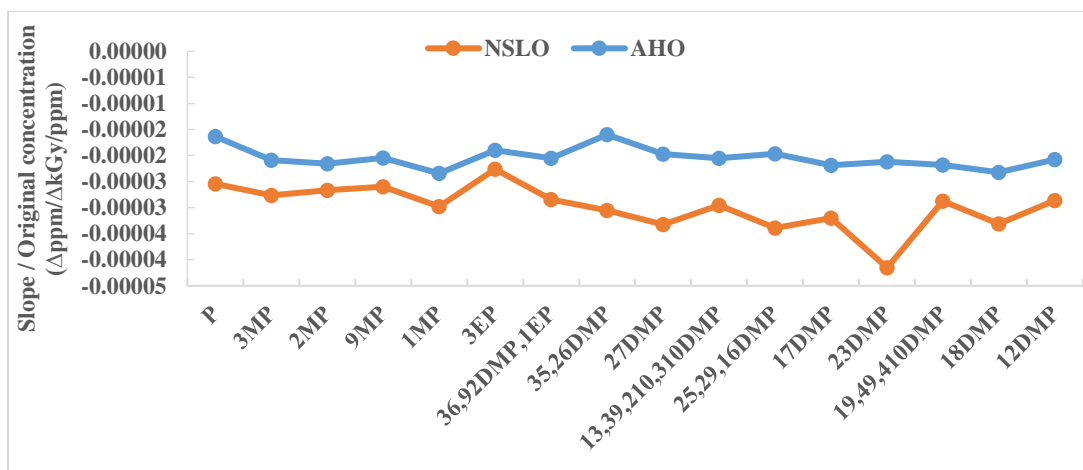


Fig. 4.12 Plot of normalized slopes (normalized concentration vs. dose) for phenanthrene and C_{1-2} alkyl-phenanthrenes in high-dose (0–10000 kGy) irradiated NSLO and AHO samples

As indicated by Fig. 4.12, the slope variation of NSLO and AHO are normalized to similar pattern by eliminating the original concentration factor. However, it is noticeable that the radiolysis rate of NSLO is still higher than AHO, which indicated a lower stability of phenanthrene compounds in these lighter oils. This could be attributed to their different geochemical composition and oil matrix, which will be further discussed In following sections and Chapter 5.

4.2.3 Aromatic steroid hydrocarbons (TAS & MAS)

The loss of a methyl group at the A/B ring junction during thermal maturation results in the aromatization of C-ring monoaromatic (MA) steroid hydrocarbons to ABC-ring triaromatic steroid (TA) hydrocarbons (Fig. 4.13). The asymmetric center at C-5 is lost during conversion of the monoaromatic to the triaromatic compounds. Thus, maturation of monoaromatic steroids yields triaromatic steroids with one less carbon (Peters et al., 2005).

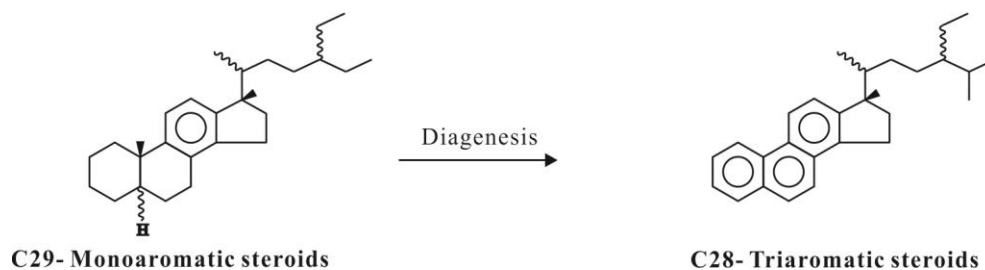


Fig 4. 13 Conversion of C29-monoaromatic (MA) with C28-triaromatic (TA) steroids during thermal maturation (Peters et al., 2005)

The MAS includes the total of all C₂₇–C₂₉ C-ring monoaromatic steroid hydrocarbon family peaks (m/z 253) and the TAS represents the total of all C₂₆–C₂₈ triaromatic steroid hydrocarbon family peaks (m/z 231) (Table A2.4). The distributions are characterized in Fig. 4.14.

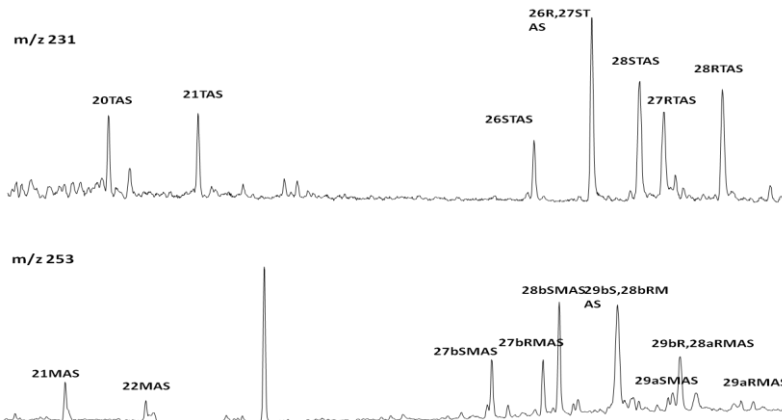


Fig. 4.14 Distribution of mono-, tri-aromatic steroid shown in GC-MS chromatograms m/z 253, 231 of the aromatic hydrocarbon fraction of non-irradiated NSLO and AHO samples

Concentrations of mono- and triaromatic steroid hydrocarbons versus radiation dose are plotted in Fig. 4.15. With increasing radiation dose, the concentration of identified TAS have a very consistent destruction ranging from 815 to 388 ppm for NSLO (with a slope around -0.029 ($\Delta\text{ppm}/\Delta\text{kGy}$)) and from 335 to 240 ppm for AHO (with a slope around -0.009 ($\Delta\text{ppm}/\Delta\text{kGy}$)).

Destruction of MAS was also observed in both NSLO and AHO samples. However, due to a less stable molecular structure compared with triaromatic steroid hydrocarbons, the destruction of monoaromatic steroid hydrocarbons for both oils were not consistent with radiation dose (with R^2 around 0.5 for NSLO, and lower for AHO).

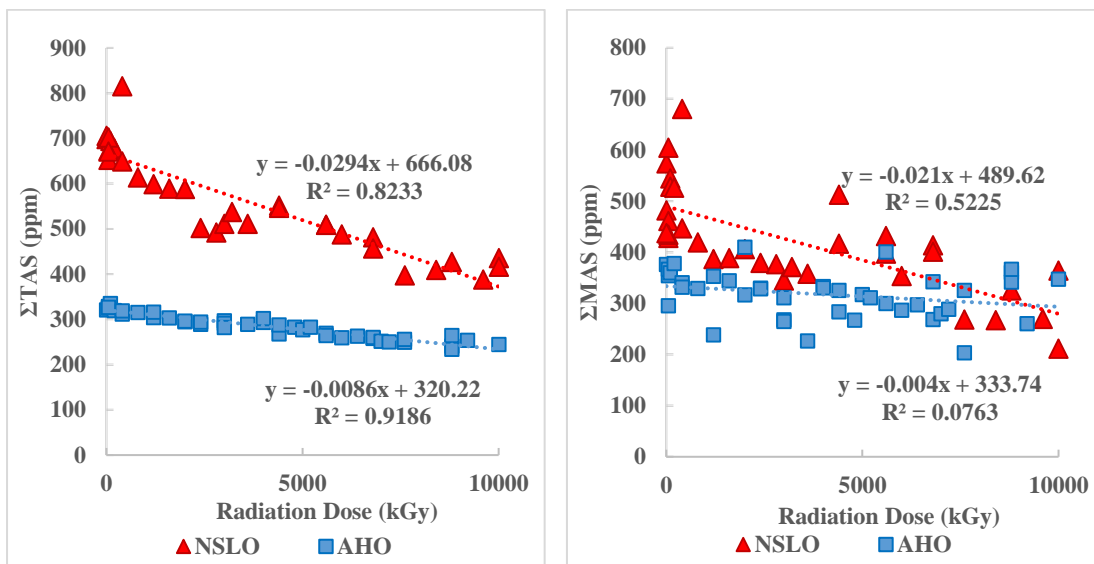


Fig. 4.15 Plots showing the variation in concentrations of monoaromatic steroid (MAS) and triaromatic steroid (TAS) hydrocarbons with radiation dose (kGy)

The degradation of individual monoaromatic steroid and triaromatic steroid hydrocarbons are within the slope range of -0.0087 ($\Delta\text{ppm}/\Delta\text{kGy}$) to -0.0003 ($\Delta\text{ppm}/\Delta\text{kGy}$) for NSLO and -0.0020 ($\Delta\text{ppm}/\Delta\text{kGy}$) to -0.00001 ($\Delta\text{ppm}/\Delta\text{kGy}$) for AHO (Fig. 4.16). After normalization (Fig.4.17), the results indicated that radiolysis rate of triaromatic steroids were basically increasing with carbon number.

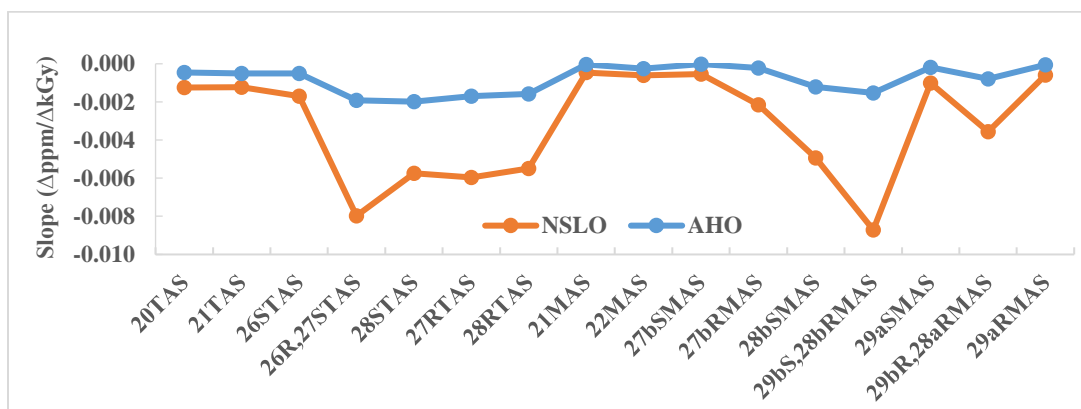


Fig. 4.16 Plot of slopes ($\Delta\text{ppm}/\Delta\text{kGy}$) for MAS and TAS in high-dose (0–10000 kGy) irradiated NSLO and AHO samples

Again, the normalized slope results indicated that after eliminating the effect of original concentration, the radiolysis rate for heavy oil were still slower than light oil. Thus, it is reasonable to infer that the matrix of oil is also an important factor affecting the radiolysis process and compounds destruction.

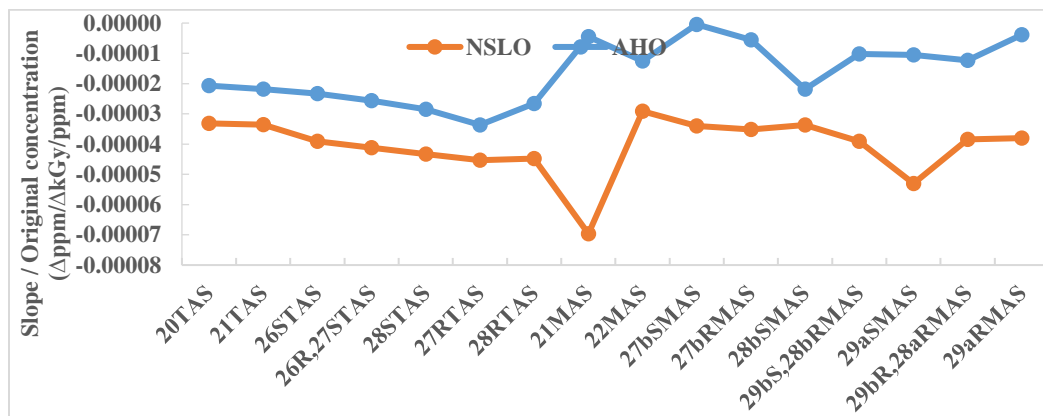


Fig. 4.17 Plot of normalized slopes (normalized concentration vs. dose) for MAS and TAS in high-dose (0–10000 kGy) irradiated NSLO and AHO samples

4.2.4 Steranes (STs)

Most steranes in crude oil originate from sterols in the lipid membranes of eukaryotic organisms during diagenesis (Ourisson et al., 1979). During the burial history, steranes with biological configurations convert to their isomers with more stable geological configurations (Fig. 4.18). The distribution of identified compounds including pregnanes, steranes and diasteranes (Table A1.4) was shown on m/z 217 mass chromatogram (Fig. 4.19) with generally similar patterns for AHO and NSLO.

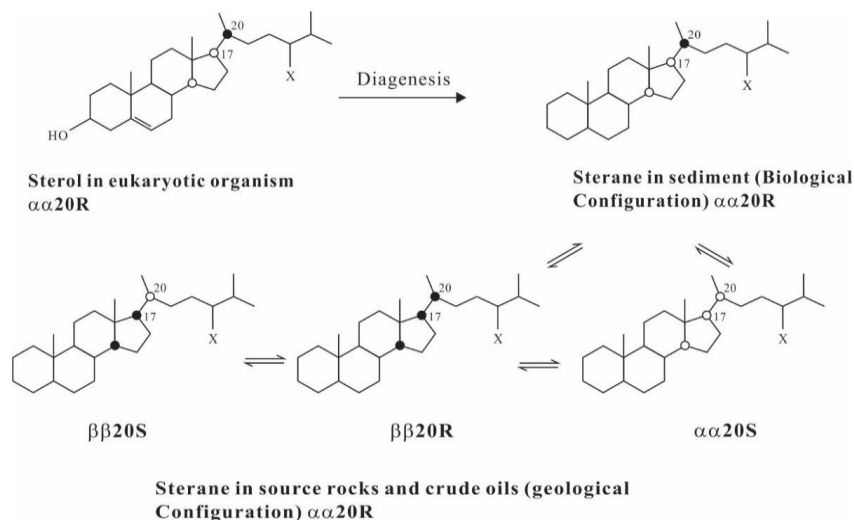


Fig. 4.18 Formation and isomerization of steranes (after Peters et al., 2005)

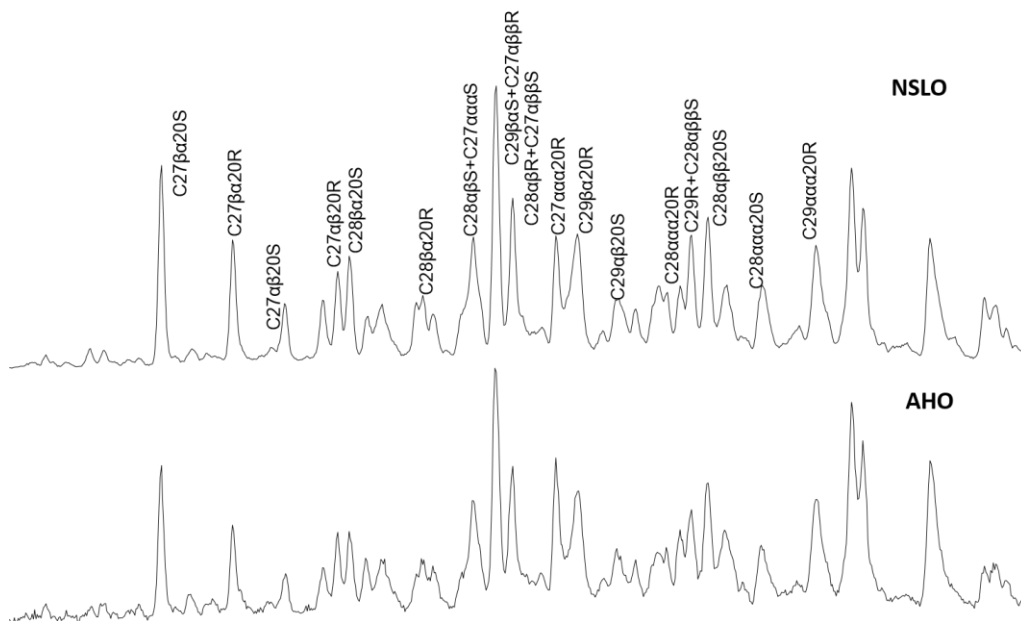


Fig. 4.19 Distribution of steranes shown in GC-MS chromatogram m/z 217 of the saturated hydrocarbon fraction of non-irradiated NSLO and AHO samples

Similar to the terpenoids, the concentration of steranes decrease with increasing radiation dose for both oils (Fig. 4.10), with a slope of around -0.068 ($\Delta\text{ppm}/\Delta\text{kGy}$) for NSLO and -0.016 ($\Delta\text{ppm}/\Delta\text{kGy}$) for AHO. Compared with above classes, the destruction of steranes for both NSLO and AHO samples were featured by relatively more scattered data with lower R^2 value (< 0.7).

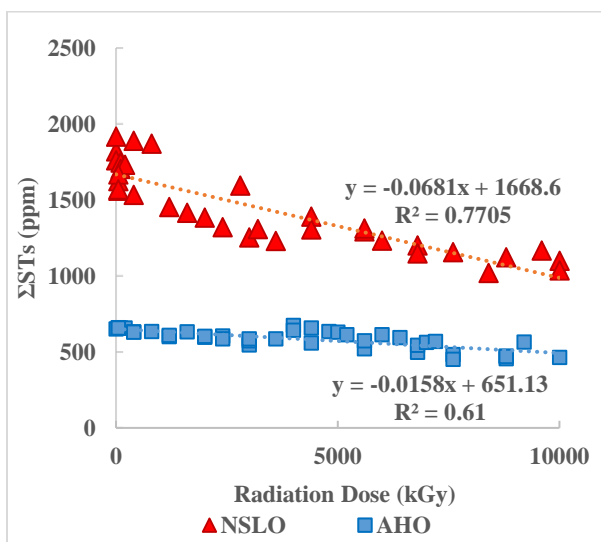


Fig. 4.20 Plots showing the variation in concentrations of steranes with radiation dose (kGy)

To look into the inconsistencies existing in each oil data set, the two phases of experiments were plotted separately. As Fig. 4.21 indicated, the radiolysis destruction was more consistent internally within each experimental phase (with $R^2 > 0.8$), and the calculated slope for individual phase was higher than plotting all data together. The variation for the two phases might be due to experimental error caused by internal standard concentration. Here, sterane would also be considered as a good radiolysis indicator ("Level 1" compound) assuming that the experimental errors were excluded.

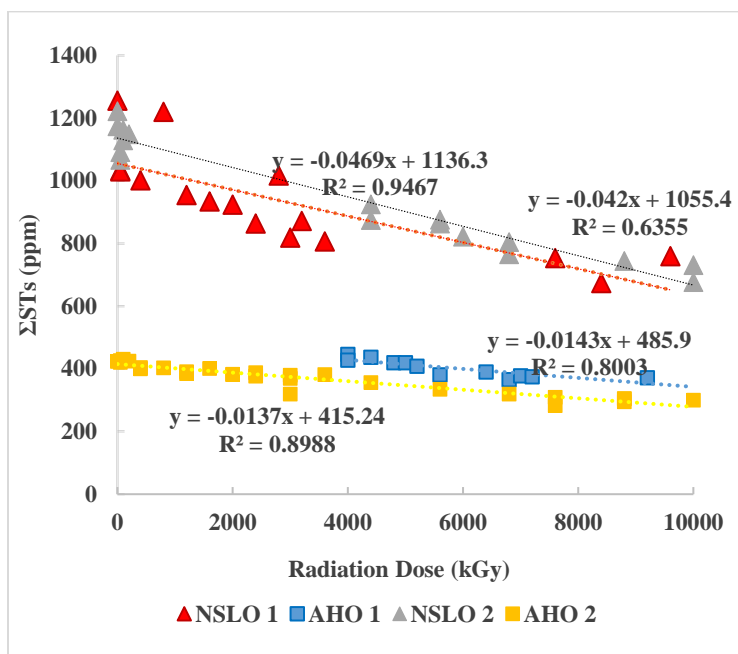


Fig. 4.21 Plots showing the variation in concentrations of steranes with radiation dose (kGy) for samples irradiated in phase 1 & 2

To ensure the accuracy of slope values, only phase 2 concentration data was selected for slope calculation (Fig. 4.22). The pregnanes, steranes and diasteranes are generally within the slope range of -0.0073 ($\Delta\text{ppm}/\Delta\text{kGy}$) to -0.0006 ($\Delta\text{ppm}/\Delta\text{kGy}$) for NSLO and -0.0027 ($\Delta\text{ppm}/\Delta\text{kGy}$) to -0.0002 ($\Delta\text{ppm}/\Delta\text{kGy}$) for AHO.

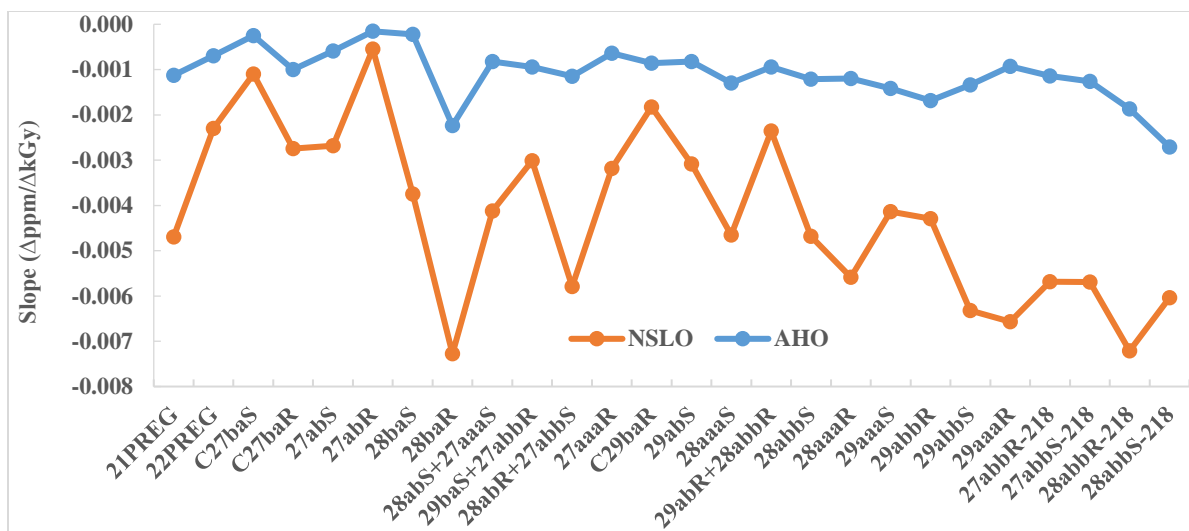


Fig. 4.22 Plot of degradation slopes ($\Delta\text{ppm}/\Delta\text{kGy}$) for steranes in high-dose (0–10000 kGy) irradiated NSLO and AHO samples

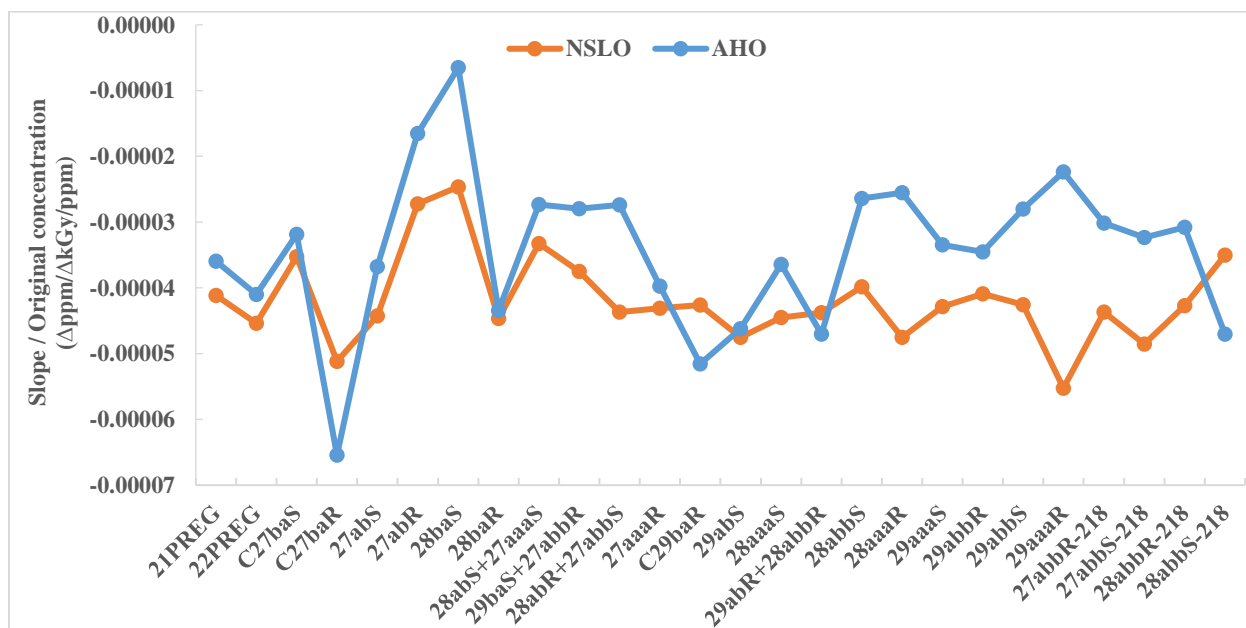


Fig. 4.23 Plot of normalized slopes (normalized concentration vs. dose) for steranes in high-dose (0–10000 kGy) irradiated NSLO and AHO samples

As indicated by Fig. 4.23, after eliminating cocentration factor, the normalized slope of NSLO and AHO exhibit similar patterns with a more sensitive trend for light oils. Some of the individual compounds, especially steranes with higher carbon number, show adverse radiation resistance for the light and heavy oils.

4.3 "Level 2" compounds

4.3.1 Naphthalene and alkylnaphthalenes (N)

Polycyclic aromatic hydrocarbons (PAHs) are a class of organic compounds characterized by fused-ring chemical structures. They are generally found in crude oils and source rock extracts throughout geological time but absent in the living organisms. Naphthalene ($C_{10}H_8$) is the simplest PAH with a fused pair of benzene rings. The C_{0-5} -alkylnaphthalenes are common constituents of oils and source rock extracts (Huang et al., 2004).

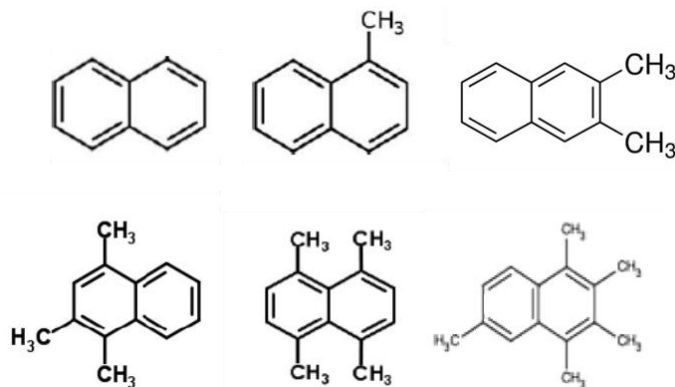


Fig. 4.24 Structure of naphthalene and C_{1-5} methylnaphthalenes

The structure of naphthalene and its alkyl substitutes including dimethylnaphthalenes (DMNs), trimethylnaphthalenes (TMNs), tetramethylnaphthalenes (TeMNs) and pentamethylnaphthalenes (PMNs) (Table A2.1) are shown as Fig. 4.24, and the compounds are detected from GC-MS traces (m/z 128, 142, 156, 170, 184, 198) (Fig. 4.25).

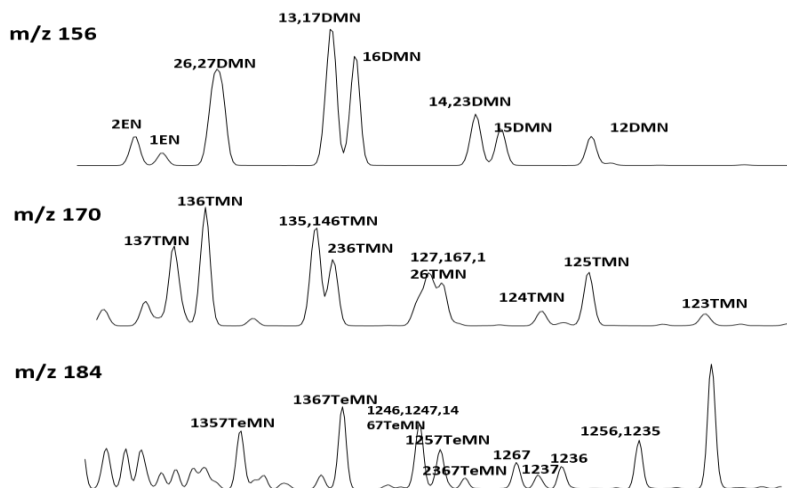


Fig. 4.25 Distribution of alkylnaphthalenes shown in GC-MS chromatogram m/z 156, 170,184 of the aromatic hydrocarbon fraction of non-irradiated NSLO samples

The alkylnaphthalenes are enriched in NSLO and AHO, especially with significantly high abundance in NSLO samples. The concentration of the sum of the C_{0.5} alkylnaphthalenes was calculated and plotted with increasing radiation dose (Fig. 4.26).

For NSLO samples, a large concentration variation of the total amount of alkyl-substituted naphthalenes exists (Fig. 4.26), changing from 11868 to 5753 ppm for NSLO (with a slope around -0.285 (Δppm/ΔkGy)) and 2827 to 1745 ppm for AHO (with a slope around -0.022 (Δppm/ΔkGy)).

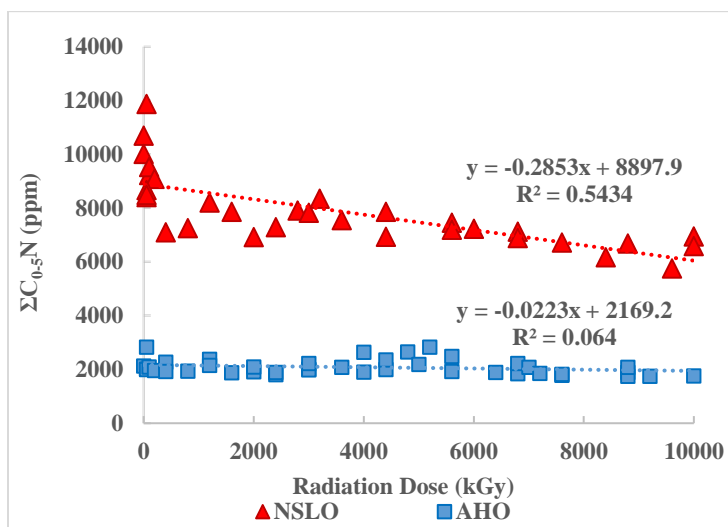


Fig.4.26 Plots showing the variation in concentrations of naphthalenes and C_{0.5} alkylnaphthalenes with radiation dose (kGy)

The concentration data of phase 1 and 2 for naphthalene with no alkyl-substitute have set variation, and were in relatively poor radiolysis correlation with the radiation dose in both NSLO and AHO samples (Fig. 4.27). This could result from the high volatility of naphthalene or the slight error of internal standard compound. However, it is reasonable to infer that naphthalene and alkyl-substituted naphthalenes may also be included in "Level 1" radiolysis indicators if irradiation and separation experiments were conducted in only one batch.

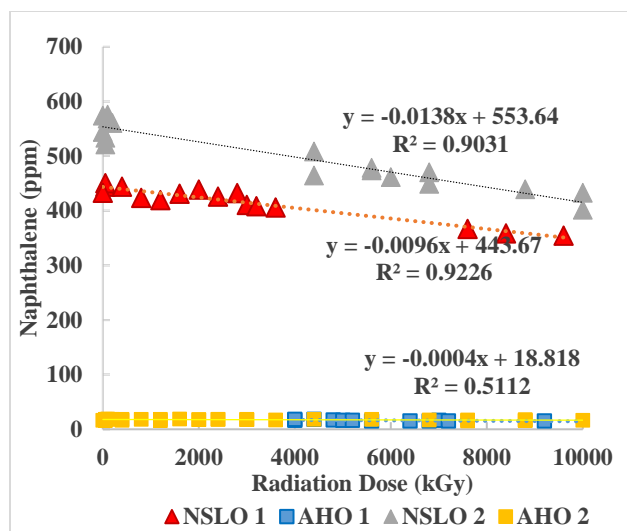


Fig. 4.27 Plots showing the variation in concentrations of naphthalene with radiation dose (kGy) for NSLO and AHO samples irradiated in phase 1 and 2

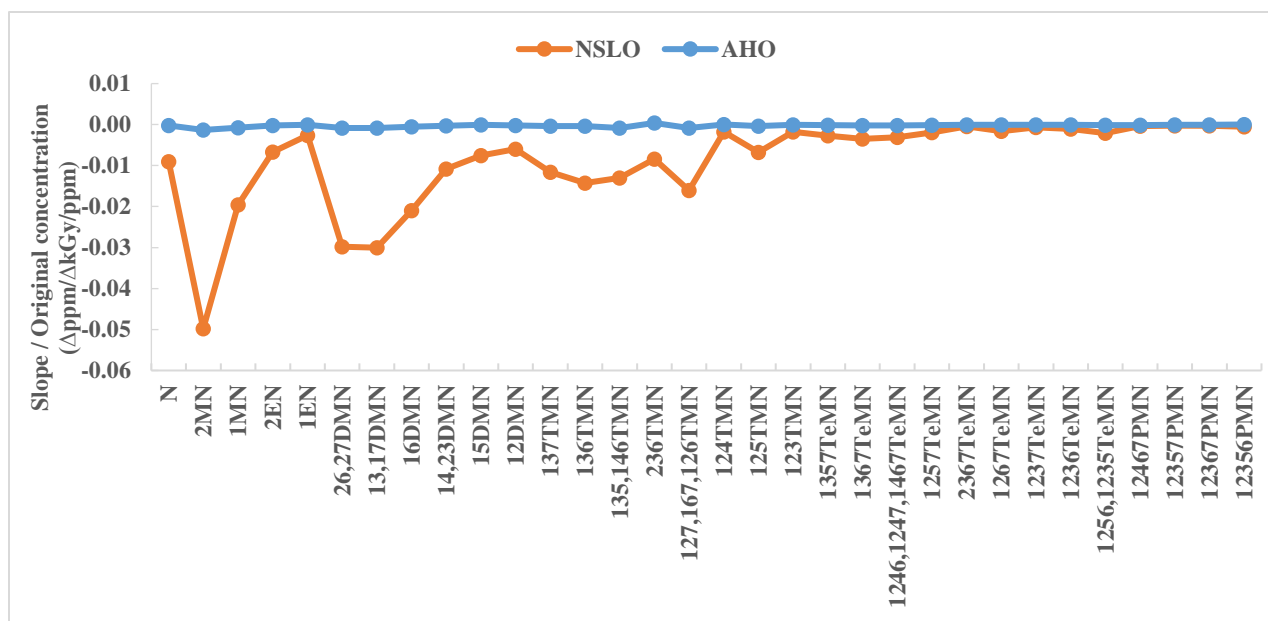


Fig. 4.28 Plot of degradation slopes ($\Delta\text{ppm}/\Delta\text{kGy}$) for sum C_{0-5} alkyl naphthalenes in high-dose (0–10000 kGy) irradiated NSLO and AHO samples

The individual naphthalene and its alkyl-substituted compounds are within the slope range of -0.0500 ($\Delta\text{ppm}/\Delta\text{kGy}$) to -0.0003 ($\Delta\text{ppm}/\Delta\text{kGy}$) for NSLO and -0.0001 ($\Delta\text{ppm}/\Delta\text{kGy}$) to 0.0008 ($\Delta\text{ppm}/\Delta\text{kGy}$) for AHO (Fig. 4.28). Fig. 4.28 shows the normalized slope of naphthalene class which could eliminate the factor of original concentration for different compounds. The results

indicated that lighter compounds including naphthalene, 2MN and 1MN are slightly more stable than the C₂₋₅N group in NSLO samples, while less stable in AHO samples.

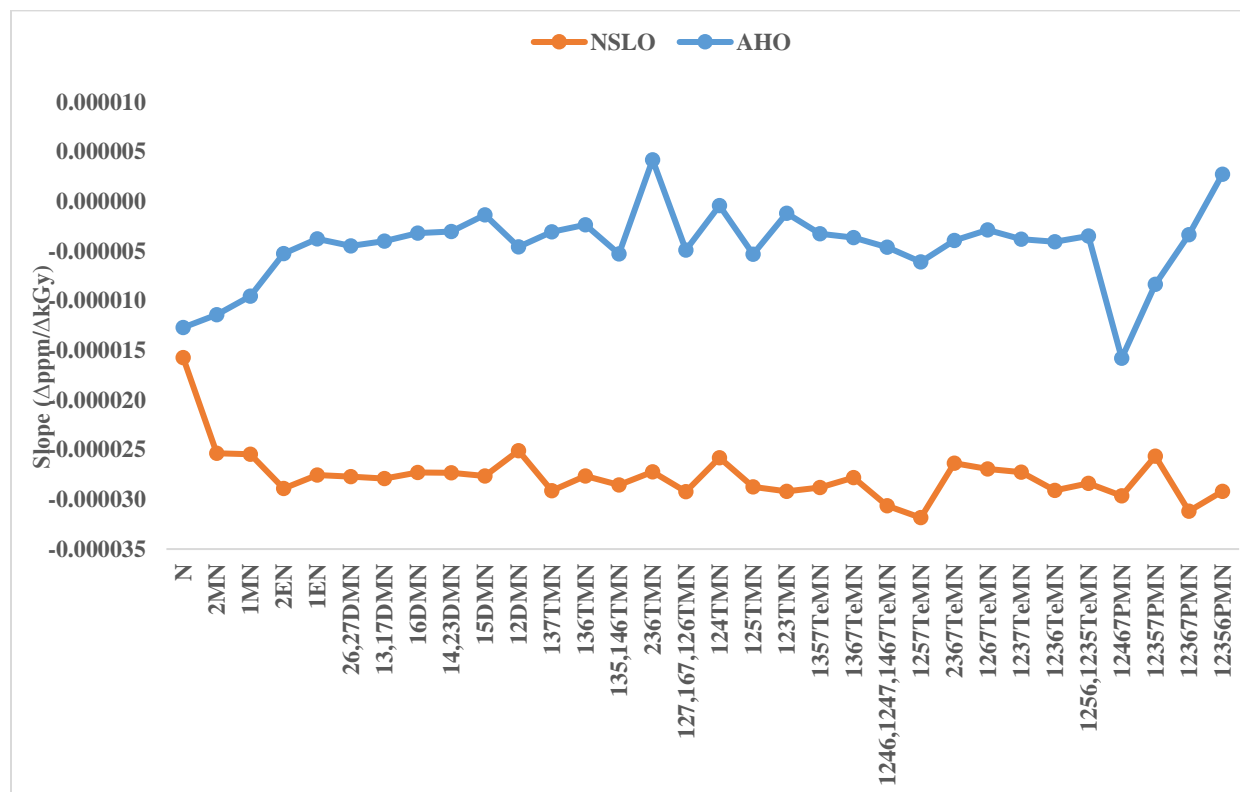


Fig. 4.29 Plot of normalized slopes (normalized concentration vs. dose) for naphthalenes and C₁₋₅ alkylnaphthalenes in high-dose (0–10000 kGy) irradiated NSLO and AHO samples

4.3.2 Dibenzothiophenes (DBTs)

Dibenzothiophene (DBTs) is the organosulfur compound consisting of two benzene rings and a central thiophene ring (Fig. 4.30). This tricyclic heterocycle, and especially its alkyl homologues, occur widely in heavier fractions of petroleum.

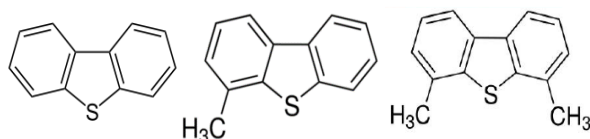


Fig. 4.30 Chemical structure of dibenzothiophenes and alkyldibenzothiophenes

The dibenzothiophene, methyl-, and dimethyl-dibenzothiophene isomers (Table A2.2) were detected from GC-MS traces (*m/z* 184, 198, 212) (Fig. 4.31).

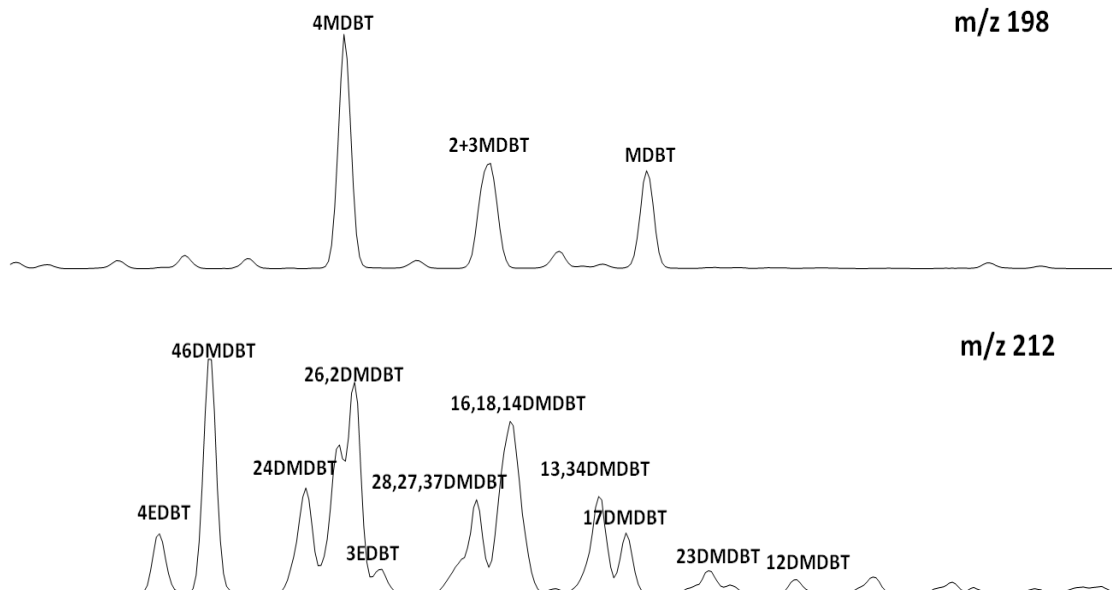


Fig. 4.31 Distribution of alkyldibenzothiophenes shown in GC-MS chromatogram m/z 198, 212 of the aromatic hydrocarbon fraction of non-irradiated NSLO samples

The concentration of methyl-dibenzothiophenes (MDBTs) and C_{0-3} dibenzothiophenes were plotted versus radiation dose respectively. MDBTs were destroyed for both oils with concentration ranging from 385 to 283 ppm for NSLO and 178 to 143 ppm for AHO (Fig. 4.32). The clusters of C_{0-3} dibenzothiophenes show higher destruction rate (with a slope around -0.009 ($\Delta\text{ppm}/\Delta\text{kGy}$) for NSLO and -0.017 ($\Delta\text{ppm}/\Delta\text{kGy}$) for AHO).

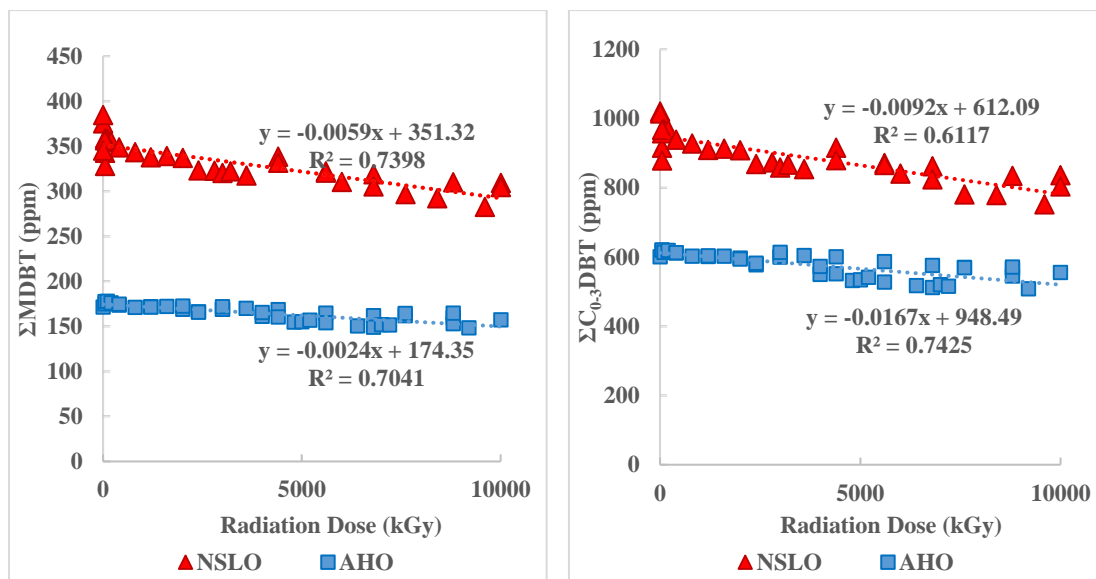


Fig. 4.32 Plots showing the variation in concentrations of MDBT and C_{0-3} DBT with radiation dose (kGy)

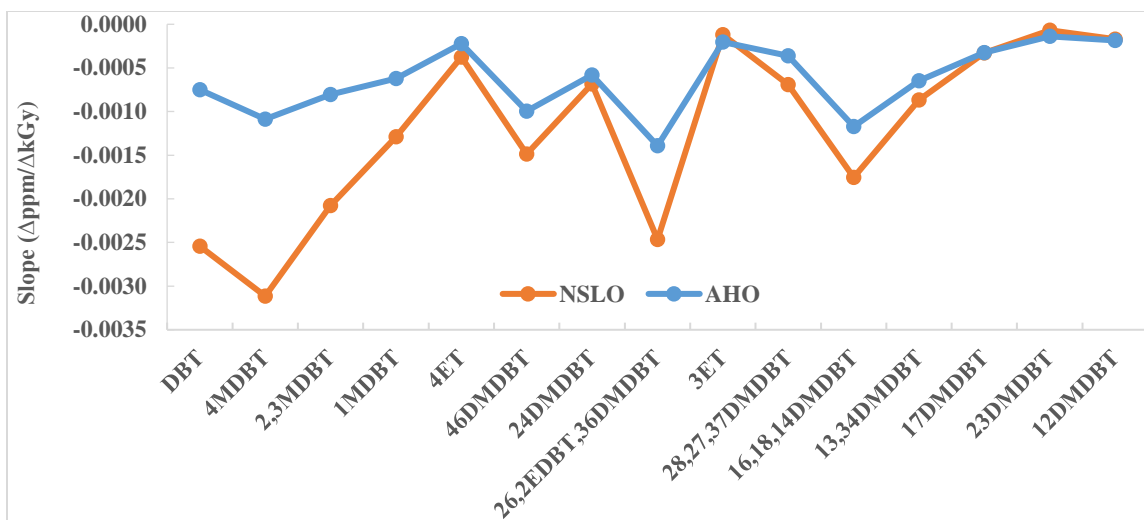


Fig. 4.33 Plot of degradation slopes ($\Delta\text{ppm}/\Delta\text{kGy}$) for dibenzothiophene and C₀₋₂ dibenzothiophenes in high-dose (0-10000 kGy) irradiated NSLO and AHO samples

The slope of individual dibenzothiophene and its alkyl-substituted compounds are within the range of -0.0030 ($\Delta\text{ppm}/\Delta\text{kGy}$) to -0.00005 ($\Delta\text{ppm}/\Delta\text{kGy}$) for NSLO and -0.0015 ($\Delta\text{ppm}/\Delta\text{kGy}$) to -0.00015 ($\Delta\text{ppm}/\Delta\text{kGy}$) for AHO (Fig. 4.33). After normalization to the original concentration (Fig. 4.34), several larger compounds such as 24DMDBT, 3ET and 23DMDBT showed a faster radiolysis rate for NSLO than the AHO.

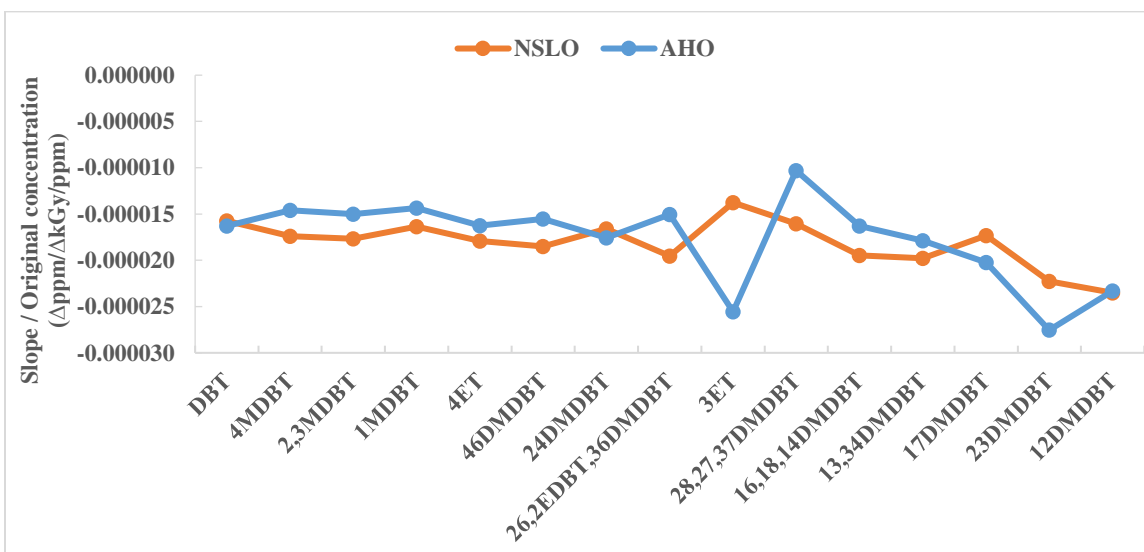


Fig. 4.34 Plot of normalized slopes (normalized concentration vs. dose) for dibenzothiophene and C₀₋₂ dibenzothiophenes in high-dose (0–10000 kGy) irradiated NSLO and AHO samples

4.3.3 Normal and isoprenoid alkanes

Normal alkanes (*n*-alkanes), with a general formula C_nH_{2n+2} , are the straight-chain alkanes and are present in significant concentrations in crude oils and sediments. Brooks (1969) explains the abundant *n*-alkanes in most crude oils as originating from lipids in living organisms, including naturally occurring *n*-alkanes and fatty acids. The C_{19} and C_{20} isoprenoids (pristane and phytane) are primarily derived from the phytyl side chain of chlorophyll in phototrophic organisms, but other sources such as archaea have also been reported (Chappe et al., 1982; Goossens et al., 1984).

The distribution of *n*-alkanes ($>C_8$) and isoprenoid alkanes (Table A1.1) are shown on mass chromatogram m/z 85 with a significant distinction among the NSLO and AHO samples (Fig. 4.35). The *n*-alkanes occur in significant quantities in the original and irradiated North Sea light oil sample. As for the AHO sample, the *n*-alkanes were almost absent due to severe biodegradation.

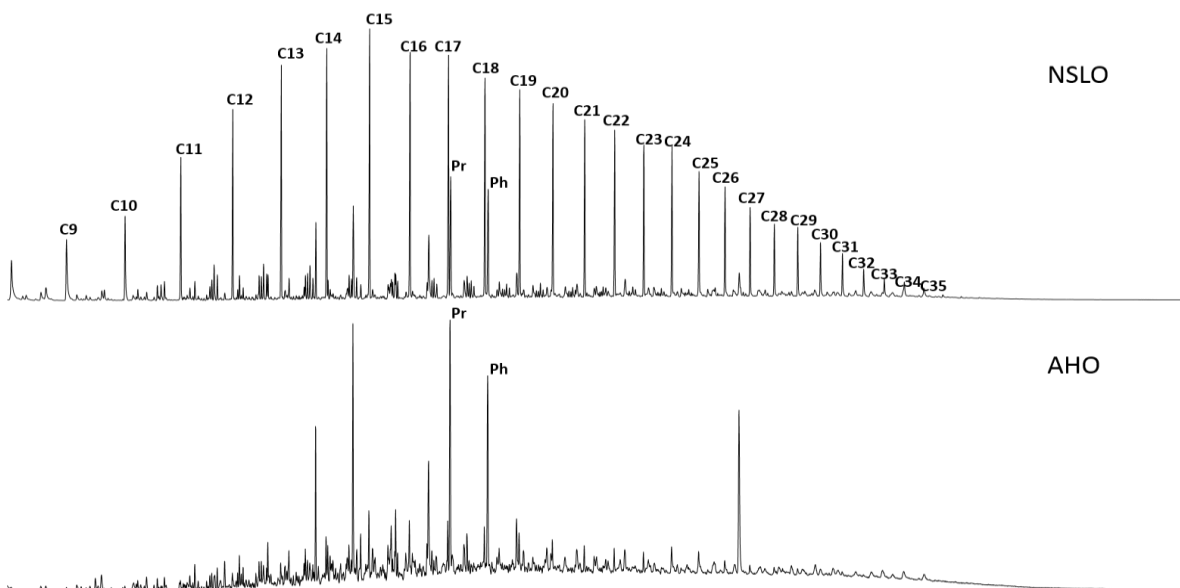


Fig. 4.35 Distribution of normal and isoprenoid alkanes shown in GC-MS chromatogram m/z 85 of the saturated hydrocarbon fraction of non-irradiated NSLO and AHO samples (Pr: pristane, Ph: phytane)

After irradiation, the concentration varies a lot in the two oils with increasing radiation dose. Due to variation in data between the two experimental phases, the sum of the concentrations of the C_9 - C_{35} alkanes (detectable on GC-MS) in NSLO only show consistent destruction in abundance internally (with a slope around -0.333 ($\Delta\text{ppm}/\Delta\text{kGy}$) for phase 1 samples and -0.609 ($\Delta\text{ppm}/\Delta\text{kGy}$) for phase 2 samples) (Fig. 4.36).

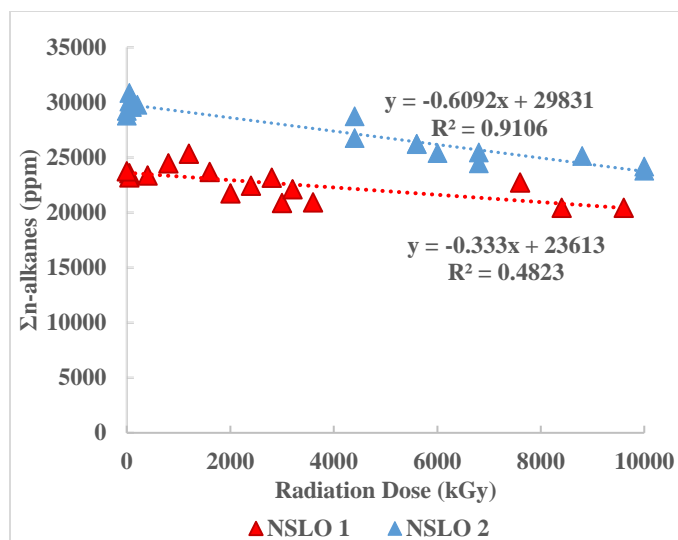


Fig. 4.36 Plots showing the variation in concentrations of C_{9-35} n -alkanes with radiation dose (kGy) for NSLO samples irradiated in phase 1 and 2

The concentration of AHO samples decreased from 1465 to 959 ppm with a slope around -0.323 ($\Delta\text{ppm}/\Delta\text{kGy}$) (Fig.4.37).

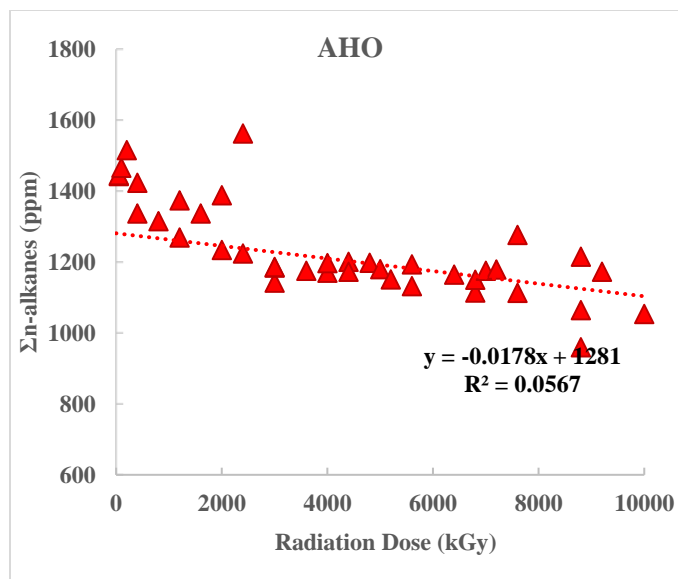


Fig. 4.37 Plots showing the variation in concentrations of C_{9-35} n -alkanes with radiation dose (kGy) for AHO samples

Interestingly, the n -alkane and isoprenoid alkanes show different radiolysis behavior after irradiation. After plotting the degradation slope ($\Delta\text{ppm}/\Delta\text{kGy}$) for individual n -alkane (C_9-C_{35}) components, there is a noticeable shift between C_{12} and C_{13} alkanes. As Fig. 4.38 indicated, lighter

n-alkanes (C_{9–12}) were basically generated after oil radiolysis, with a positive value of slope. While, larger ones (C_{13–35}) show systematic decreases in concentration with increasing radiation dose.

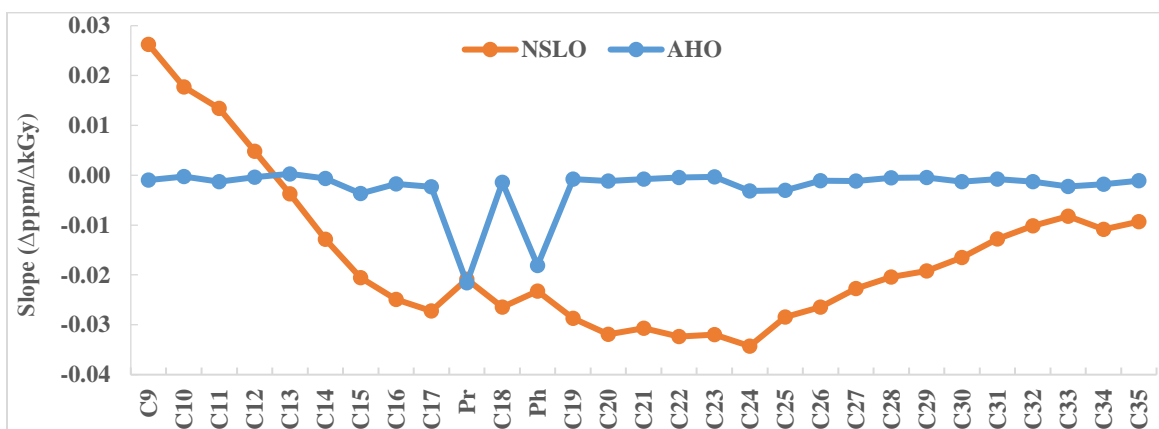


Fig. 4.38 Plot of degradation slopes ($\Delta\text{ppm}/\Delta\text{kGy}$) for *n*-alkanes (C₉–C₃₅) and isoprenoid alkanes (pristane and phytane) in high-dose (0–10000 kGy) irradiated North Sea Light Oils

An inflexion was also noticed as Fig. 4.38 shows. The magnitude of slope continuously increased for the short-middle chain (*n*-C₉ to *n*-C₂₄) components, reaching the most negative point at the C₂₄ alkane (-0.034 ($\Delta\text{ppm}/\Delta\text{kGy}$)), and then decreasing for middle to long chain (*n*-C₂₅ to *n*-C₃₅) components.

It could be inferred that during the irradiation process, high energy γ -particles may enter the hydrocarbon phase, the chemical bonds of larger *n*-alkanes were thus broken under the bombardment. Lighter *n*-alkanes are generated while the larger ones are destroyed, with even stronger radiolysis resistance when carbon number increases. Intermediate carbon number *n*-alkanes, such as compounds in the range of *n*-C₁₃ to *n*-C₂₀ are both being produced and degraded in significant amount.

4.4 "Level 3" compounds (compounds with poor correlated concentration and dose)

4.4.1 Adamantanes (AD)

Diamondoid hydrocarbons are polycyclic alkanes that have a diamond-like structure with rigid fused rings. Adamantanes, the low molecular weight diamondoids with a small cage structure repeated throughout the crystal lattice of a diamond (Wingert, 1992), were always found in petroleum. Diamondoids are generally produced by catalytic rearrangement of polycyclic hydrocarbons during or after oil generation or even during diagenesis (Zhang et al., 2005).

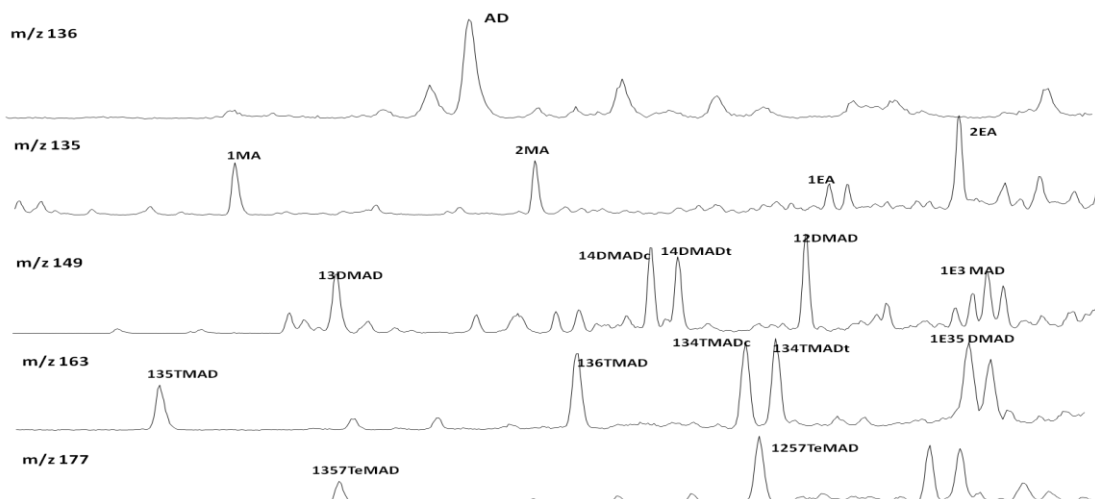


Fig. 4.39 Distribution of C₀₋₄ alkyl-adamantanes shown in GC-MS chromatogram m/z 136, 135, 149, 163, 177 of the saturated hydrocarbon fraction of non-irradiated NSLO and AHO samples

The major adamantane compounds (Table A1.4) were identified in m/z 136, 135, 149, 163, 177 mass chromatograms (Fig. 4.39). It is suggested that adamantanes are more stable than most hydrocarbons and are resistant to thermal and biological degradation once formed (Aczel et al, 1979). Thus, for AHO and NSLO, there are no significant differences in their adamantane distribution patterns as well as the concentration (Fig. 4.40).

The sum concentration of identified adamantane and its alkylated homologs decrease with increasing radiation dose at very similar rates for both oils (Fig. 4.40), with a slope of around -0.0013 ($\Delta\text{ppm}/\Delta\text{kGy}$) for NSLO and -0.0012 ($\Delta\text{ppm}/\Delta\text{kGy}$) for AHO. The poor consistency of concentration for adamantanes, however, would be due to other reactions or be resulted of experimental error between two phases, and will not be discussed in detail in this case.

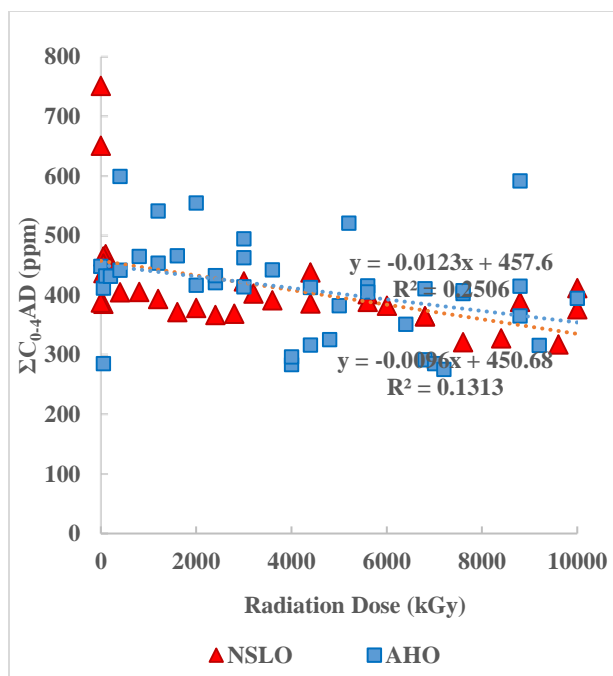


Fig. 4.40 Plots showing the variation in concentrations of sum C₀₋₄ alkyl-adamantanes with radiation dose (kGy)

4.4.2 Bicyclic sesquiterpane (BSTs)

The bicyclic sesquiterpane is composed of three C₅-isoprene subunits, which is a basic structural unit of many biomarkers. The crude oils have different abundance and distribution of BSTs, they are applied to differentiate the organic matter input from various sedimentary environments. The change of abundance of BSTs can be used to determine the extent of weathering and artificial evaporation (Yang et al., 2009). In this study, 8 main bicyclic sesquiterpanes (Table A1.2) were recognized and detected on GC-MS chromatograms (m/z 123) (Fig.4.41).

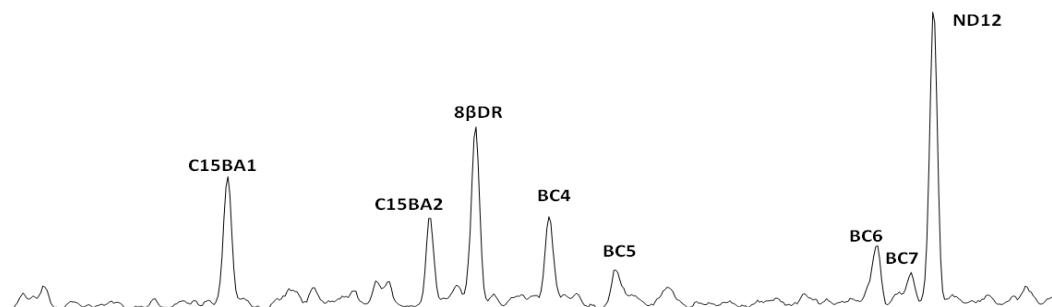


Fig. 4.41 Distribution of bicyclic sesquiterpanes shown in GC-MS chromatogram m/z 123 of the saturated hydrocarbon fraction of non-irradiated NSLO

The summed BSTs concentrations for NSLO are slightly higher than AHO, changing from 742 to 318 ppm and 753 to 261 ppm, respectively, with increasing radiation dose (Fig. 4.42).

Similarly with the adamantane class, the concentration variation for bicyclic sesquiterpanes was messy and inconsistent, while it might suggest other potential reaction processes except for compound destruction during the radiation.

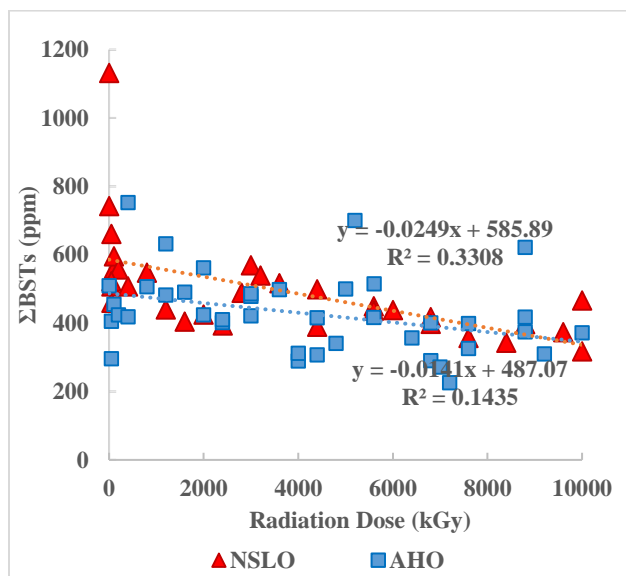


Fig. 4.42 Plots showing the variation in concentrations of bicyclic sesquiterpanes with radiation dose (kGy)

4.5 Basic radiolysis mechanism

4.5.1 Influencing factor: original concentration

As discussed above, the original concentration of individual compounds in the same compound class, as well as the summed concentration of different compound classes can be considered as the most important influencing factor during the radiolysis process, and significantly affect the destruction rates for almost every investigated compound.

For example, the naphthalene plot of the original concentration (non-irradiated) for naphthalene and alkyl-substituted naphthalenes versus their destruction slope under high-dose irradiation shows a very good correlation with $R^2 > 0.99$ (Fig. 4.43), which clearly indicates that the radiolysis impact on compounds is largely dependent on their amount before being irradiated.

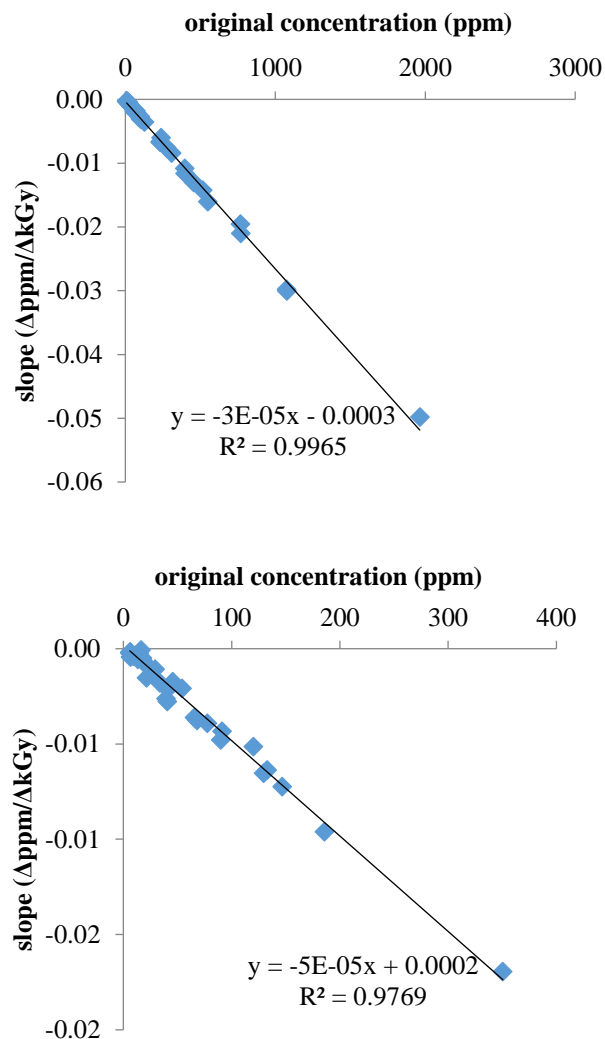


Fig. 4.43 Plots showing the variation of slopes ($\Delta\text{ppm}/\Delta\text{kGy}$) with original concentration (ppm) of $\text{C}_{0.5}$ naphthalenes (left) and tricyclic terpanes and hopanes (right) in phase 1 and 2 irradiated NSLO samples

The same relationship was also verified in tricyclic terpanes and hopanes (Fig.4.43, right), as well as other compounds and varied among different classes (further discussed in section 4.5.3).

Typically, the plotting of normal and isoprenoid alkanes exhibits a different trend compared with other compounds. During radiolysis, the lighter *n*-alkanes (C_{9-2}) show a positive radiolysis slope while larger ones (*n*- C_{13-35}) show negative slope relationship between radiation dose and compound concentration. Positive slopes indicate generation of components during radiolysis, whereas negative slopes indicate net destruction of the *n*-alkanes.

As Fig. 4.44 shows, there are 3 significant trends correlating to the original concentration. (1) The visible generation of light alkanes ($n\text{-C}_{9-12}$) was moderated and slowed down with increasing compound concentration. (2) There is a reduction in the net destruction rates for $n\text{-C}_{14-24}$ alkanes, which is likely due to the simultaneous production of such species from other oil molecules. (3) Starting from the $n\text{-C}_{24}$ alkane, the destruction rate again showed a positive correlation with original concentration, indicating a domination of compound destruction rather than production for these larger molecules.

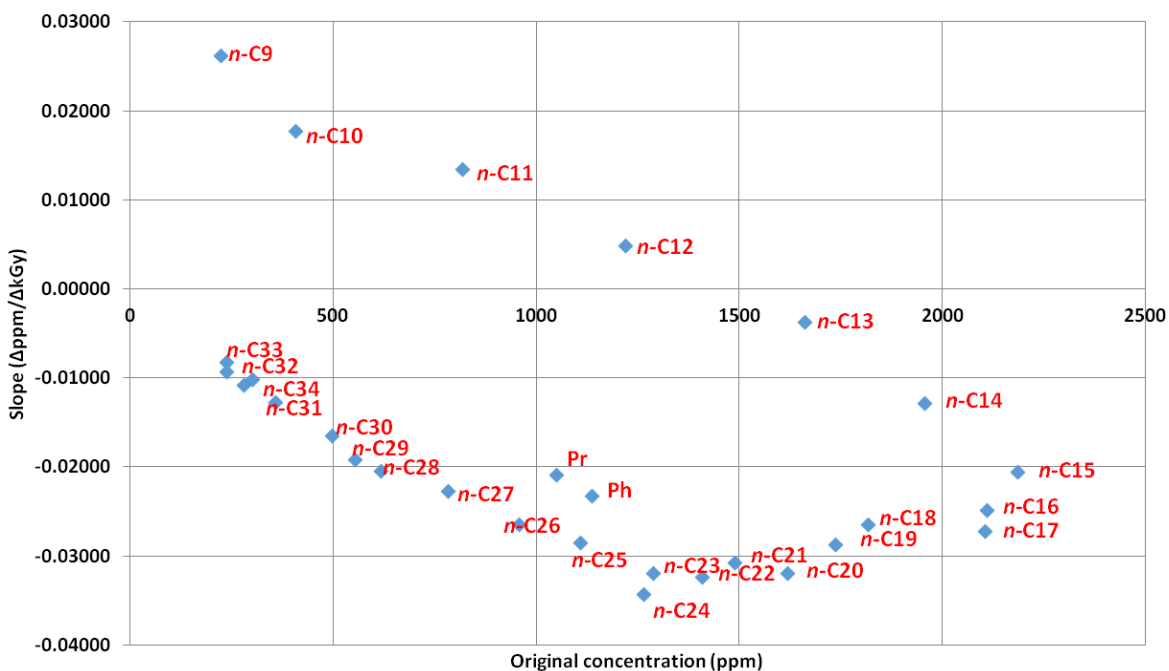


Fig. 4.44 Plots showing the variation of radiolysis slopes ($\Delta\text{ppm}/\Delta\text{kGy}$) with original compound concentration (ppm) of C_{9-35} normal alkanes in phase 1 and 2 irradiated NSLO samples

It would appear from above analysis, that the dose-dependent destruction of the alkanes depends both on the concentration and carbon numbers. The carbon number of hydrocarbons, as another important radiolysis influencing factor, affects the radiolysis process for most investigated compounds.

4.5.2 Influencing factor: compound class

The radiolysis degradation slope of each investigated compound, as measured by a linear fit of the concentration versus radiation dose, is plotted against the compound original concentrations in Fig. 4.45 (NSLO only).

The clear correlation between original concentration of a given compound and the measured degradation slope were already discussed as the major influencing factor of radiolysis. Besides, significant distinctions were found among different compound classes even if they fell within the same range of concentration, which indicates that the radiolysis was also distinctly affected by compound classes and chemical properties.

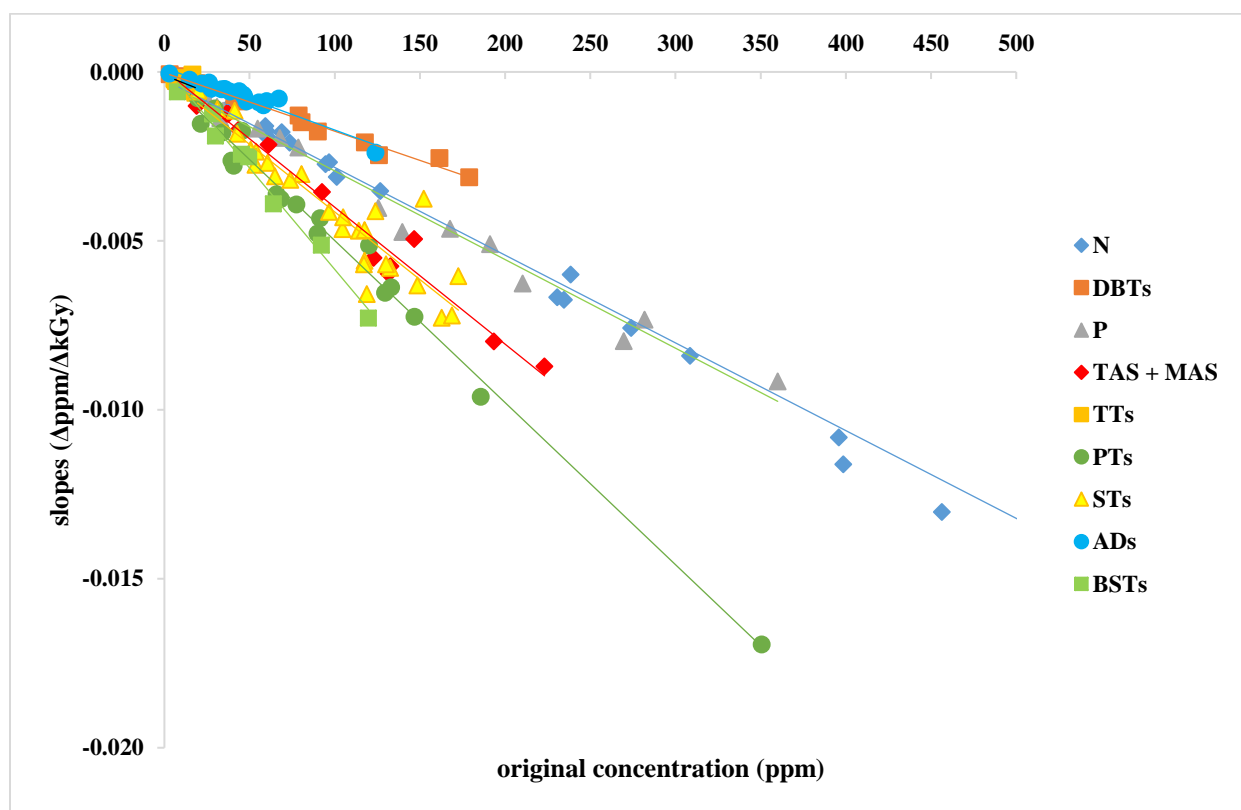


Fig. 4.45 Plots showing the variation of degradation slopes ($\Delta\text{ppm}/\Delta\text{kGy}$) with original concentration (ppm) of all compounds (*n*-alkanes are excluded) in phase 1 and 2 NSLO

Among the investigated compounds, aromatic hydrocarbons including naphthalenes, dibenzothiophenes, adamantanes, phenanthrenes and aromatic steroid hydrocarbons generally have lower destruction rates (lower slope magnitudes) compared with saturated hydrocarbons such

as steranes, terpanes and BSTs. This greater stability of aromatic species to radiation has been reported before (Williams, 1963).

As Table 4.3 shows, the compounds radiolysis rate, normalized to the original compound concentration can be sorted into the following order: hopanes > TAS and MAS > steranes > tricyclic terpanes > phenanthrenes > naphthalenes > BSTs > *n*-alkanes > DBTs > adamantanes. The normal alkanes, due to the production of lighter molecules, might have an actual higher radiolysis rate for larger compounds.

Table 4.3 Normalized radiolysis destruction slopes (normalized concentration vs. dose) for investigated hydrocarbon compounds in high-dose irradiated NSLO samples

Compound classes	Normalized slopes (slope/original concentration)
Hopanes (PT)	-4.84377E-05
Triaromatic steroid hydrocarbon (TAS)	-4.20425E-05
Monoaromatic steroid hydrocarbon (MAS)	-3.74518E-05
Steranes (STs)	-3.61339E-05
Tricyclic terpanes (TTs)	-3.13685E-05
Phenanthrenes (C0-2P)	-2.92544E-05
Naphthalenes (C0-5N)	-2.66515E-05
Bicyclic sesquiterpanes (BSTs)	-2.20422E-05
Normal and isoprenoid alkanes	-2.09616E-05
Dibenzothiophenes (C0-3DBT)	-1.76747E-05
Adamantanes (Ad)	-1.56582E-05

4.5.3 Influencing factor: oil matrix

As Fig. 4.3 shows, the destruction for every investigated compound varies between NSLO and AHO samples, even after being normalized to their original concentration. Thus, it can be inferred that compound type and concentration are not the only factors that influence the radiolysis process. Based on the above analysis, the oil matrix could be inferred to be another important factor that affects the rate of compound destruction under high-dose irradiation. This will be further considered and discussed in the following case study.

Chapter Five: Case studies I and II: High-dose and low-dose irradiated oils

Case study I: High-dose irradiated oils from Tarim Basin, NW China

In this chapter, a case study of the Tarim sample sets irradiated under high-dose (0–4000 kGy) is conducted for further discussion of the radiolysis mechanism. Ten oil/condensate samples from Tarim Basin were collected and analysed using the same method with NSLO and AHO samples. The Tarim oils in this study were all separated and analyzed in one batch, which enables higher consistency and better accuracy compared with NSLO and AHO samples. The study in this chapter mainly focuses on the effect of different oil matrix on radiolysis process.

5.1 Basic geochemical characteristics of original oils from Tarim Basin

The bulk composition and physical properties of these 10 Tarim oils as well as their geological background were already described in chapters Two and Three. In this section, a brief molecular characterization will firstly be provided, in order to give an overview and to select representative samples for further discussion.

Based on previous study, these selected oils are mixtures of previously biodegraded oil and late charged, highly mature oils which have experienced migration fractionation. The selected geochemical characteristics and molecular parameters are summarized in Table 5.1.

Table 5.1 Molecular parameters based on saturated hydrocarbon and aromatic hydrocarbons for T1-T10 non-irradiated samples

Code	TMNr	TeMNr	MPI	MDR	n-C ₁₇ /Pr	n-C ₁₈ /Ph	C ₂₉ Ts/C ₂₉ H	C ₂₉ H/C ₃₀ H	C ₂₃ TT/C ₃₀ H	Ts/(Ts+Tm)
T1	0.76	0.86	0.77	1.57	3.14	2.01	0.75	1.00	4.33	0.67
T2	0.73	0.73	0.78	1.37	4.64	3.32	0.17	0.53	0.37	0.36
T3	0.69	0.69	0.72	1.44	3.93	2.98	0.20	0.87	0.69	0.32
T4	0.62	0.58	0.95	1.55	6.15	4.37	0.43	0.87	2.99	0.59
T5	0.71	0.72	0.75	1.45	3.43	2.15	0.20	0.89	0.95	0.42
T6	0.76	0.73	0.87	1.64	3.53	2.25	0.30	1.03	2.11	0.34
T7	0.80	0.83	0.75	1.42	3.80	2.62	0.32	0.83	1.46	0.56
T8	0.72	0.73	0.78	1.47	4.10	2.63	0.17	0.89	0.80	0.38
T9	0.73	0.78	0.65	1.48	6.35	4.41	0.40	0.74	1.09	0.54
T10	0.77	0.80	0.86	1.47	5.36	4.02	0.57	0.69	0.91	0.73

(*Pr: Pristane; n-C₁₇: C₁₇ n-alkane; Ph: phytane; n-C₁₈: C₁₈ n-alkane; Ts: 18 α (H)-trisorneohopane; Tm: 17 α (H)-trisorneohopane; C₂₉Ts: 18- α (H)-30-norneohopane; C₂₉H: C₂₉17 α (H), 21 β (H) hopane; C₃₀H: C₃₀ 17 α (H), 21 β (H) hopane; C₂₃TT: C₂₃ tricyclic terpane; TMNr: 1,3,7-TMN/(137- + 125-TMN); TeMNr: 1367 TeMN/(1367- + 1256- + 1235-TeMN); MPI: 1.5×(3MP + 2MP)/(P + 9MP + 1MP); MDR: 4MDBT/1MDBT)

Higher values of C₂₉Ts/C₂₉H, TeMNr and TMNr, MPI and MDR generally correlate to higher thermal maturity. The results indicated that these oils/condensates vary significantly in their maturity levels.

The m/z 191 mass chromatograms of investigated samples are shown in Fig. 5.1. The terpane (tricyclic terpanes and hopanes) distribution for these 10 oils/condensates generally show large variations, which are caused by multiple processes including biodegradation, thermal cracking, migration fractionation and late of charge and mixing.

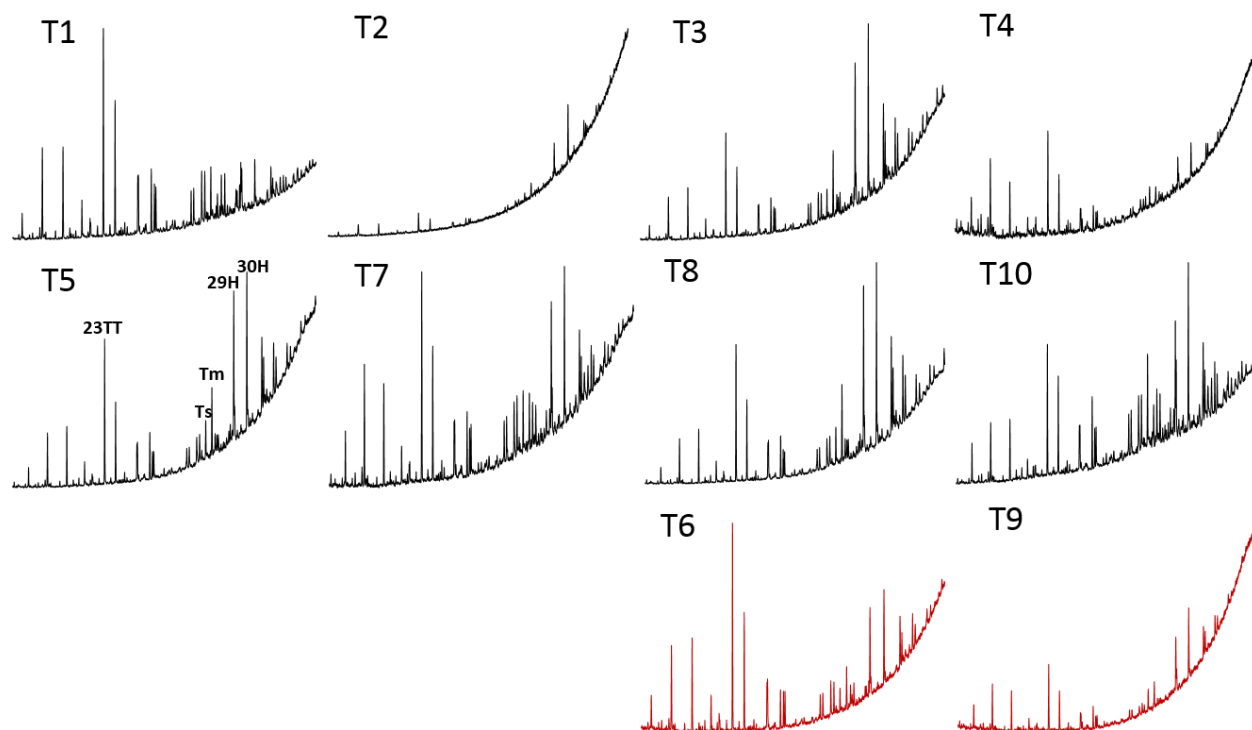


Fig. 5.1 Terpane distribution (m/z 191) of non-irradiated Tarim Oils (see Fig. 4.4 for terpane compounds distribution; black traces: oils; red traces: condensates)

Tricyclic terpanes (TTs) extend to carbon numbers up to C₃₀ and C₂₃TT is the most abundant component. There is a marked difference between the relative abundance of TTs to PTs with C₂₃TT/C₃₀H ratios (Table 5.1) varying from 0.4 (T2) to 4.3 (T1).

The pentacyclic triterpane (PT) distributions display overall similar characteristics in these oils (Fig. 5.1). Their chromatograms are dominated by 17 α (H), 21 β (H) hopane (C₃₀H), and show a decreasing relative abundance of C₃₁–C₃₅ homohopanes. The ratios of C₂₉/C₃₀H are generally < 1. Tm is generally more abundant than Ts in the heavier oils, while this relationship is reversed in the lighter oils (with higher API gravity value) such as T7 (API=43.2), T10 (API=32.4) and condensate T9, where PTs are depleted and Ts is more abundant than Tm. Ratios of Ts/(Ts+Tm) vary from 0.32–0.73 (Table 5.1)

The m/z 217 mass chromatograms of investigated samples are shown in Fig. 5.2. The sterane distribution generally shows a similar pattern and is characterized by a predominance of C₂₉ relative to C₂₈ and C₂₇ steranes although there are some variations, while T4 has a significantly lower sterane concentration showing the dominance of pregnanes.

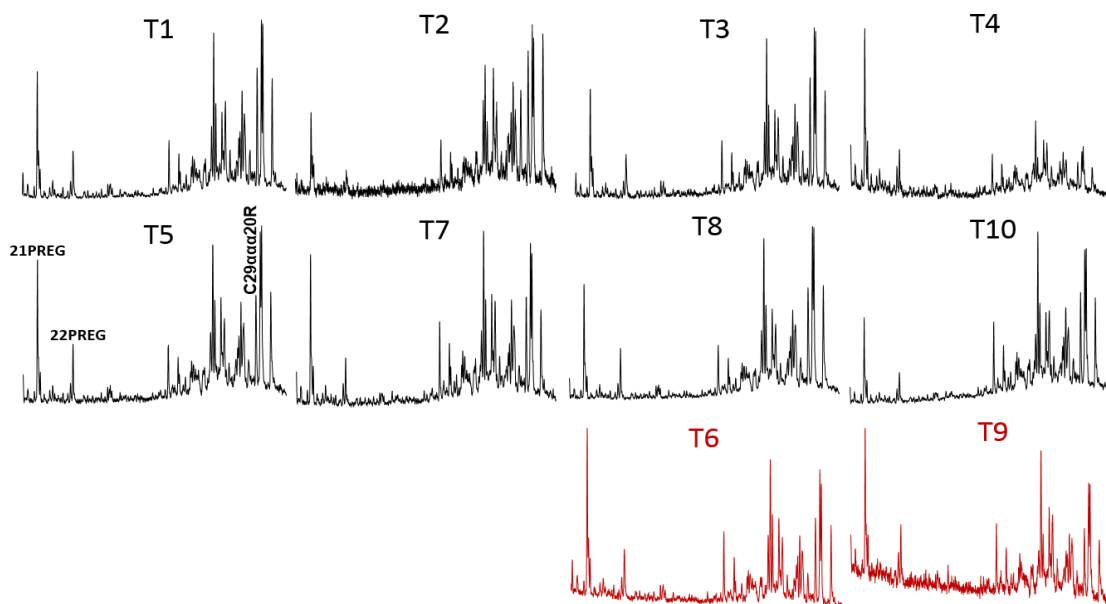


Fig. 5.2 Sterane distributions (m/z 217) of non-irradiated Tarim Oils (see Fig. 4.9 for sterane compounds distribution; black traces: oils; red traces: condensates)

Though the detailed geochemistry will not be discussed in this section, the above parameters and chromatograms can give a general sense of the maturity and composition variation among these samples.

5.2 Compound destruction rates: "SCORE" for representative radiolysis markers

The sum concentration of all investigated compound classes were calculated and plotted against radiation doses. Significant variations of concentration exist in these oils. After comparing their physical properties, geochemical characteristics and concentration similarity on the plots, T1, T2 and T6 were selected as representative samples for further discussion. The information and bulk composition for them were listed below (Table 5.2).

Table 5.2 Table of selected Tarim oil sample information and bulk composition

Code	Well	Fm.	Depth (m)	API (°)	Viscosity (cP@50°C)	Sat%	Aro%	Polar1 %	Polar2%
T1	Ha6C	O	6788.32	24.0	16.9	42.6	22.5	17.1	17.8
T2	TZ62	O	4729.25	41.1	3.0	76.0	20.6	3.0	0.3
T6	LN57	T	4342.9	53.2	1.1	78.7	15.3	2.2	3.8

In Chapter four, the radiolysis for different compounds was discussed in detail. In this section, several typical saturated and aromatic hydrocarbon compounds were plotted with radiation doses for further investigation of the mechanisms.

5.2.1 Saturated hydrocarbon: TTs, PTs, STs

The tricyclic terpanes, hopanes and steranes show similar destruction trends with good consistency (Fig. 5.3). The concentrations of these compounds were high in T1 with lower values for T2 and T6.

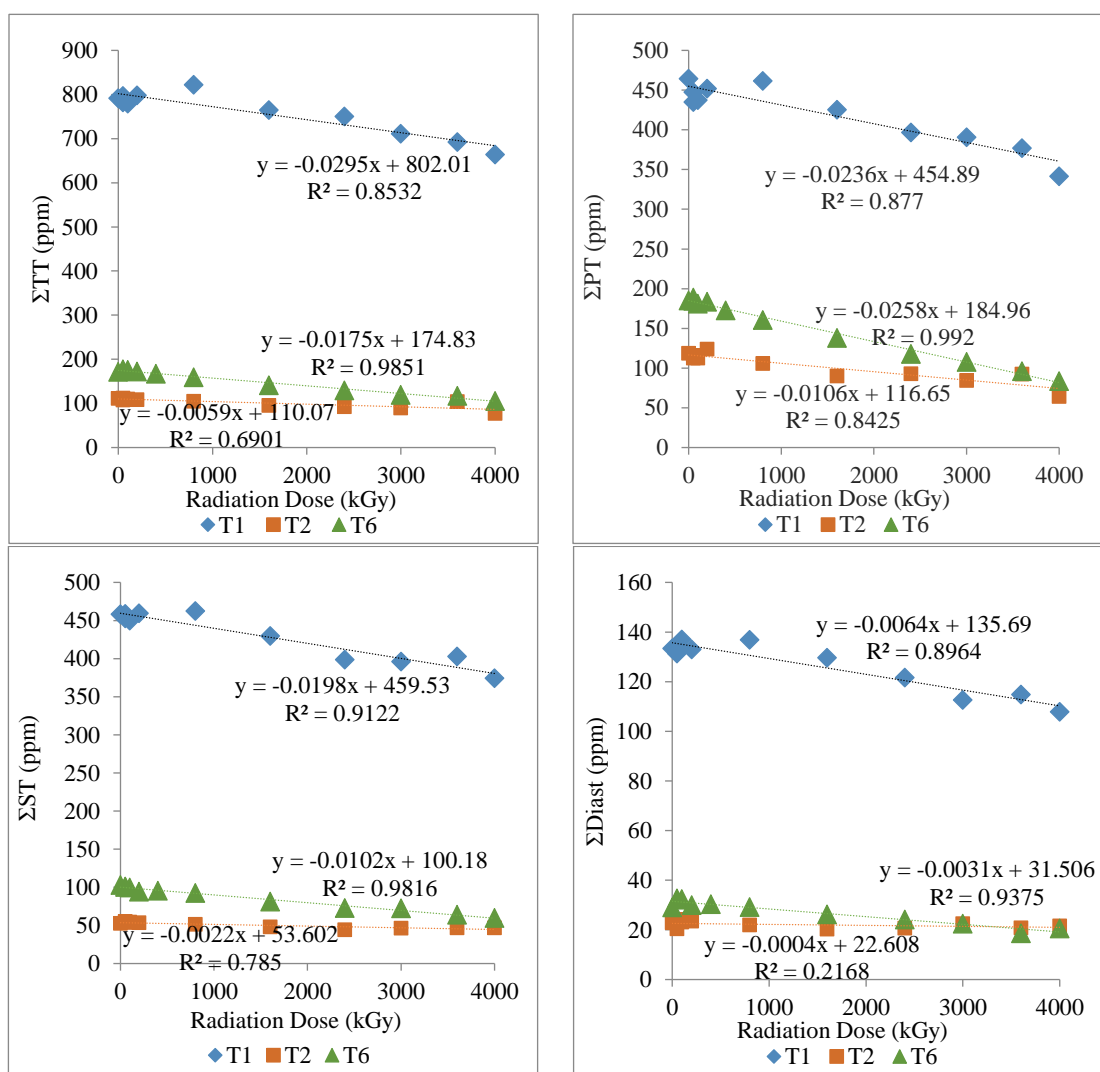


Fig. 5.3 Plots showing the variation in concentrations of tricyclic terpanes (TTs), hopanes (PTs), steranes (STs), diasteranes (Diast) with radiation dose for T1, T2 and T6 samples (kGy)

To eliminate the influence of the different original concentrations, the irradiated sample results (C_i) for each compound were all normalized to the concentration of the non-irradiated samples (C_0).

For easier comparison of these 3 different oils, a "SCORE" concept was used to evaluate the radiolysis rates. The concentration for every compound class in non-irradiated T1, T2 and T6 oils were defined as "score=100". Thus, the normalized concentration of compounds in irradiated samples ($C_{nor.}$) could be calculated as C_i/C_0 , and score [XY] (XY: compound classes) for irradiated samples is:

$$\text{score [XY]} = 100 \times C_i / C_0$$

Score is a direct indication of compound radiolysis extent, with a faster decreasing of value correlated to a faster radiolysis speed.

We also define the capital "SCORE" to be another evaluation parameter for radiolysis of every compound class, which is calculated as below:

$$\text{SCORE} = 4000 \times | \text{slope} [\Delta \text{score} / \Delta \text{dose}] |$$

Numerically, it represents the changing rate of "score" on a one-hundred-unit scale. The value of SCORE can be considered as a measurement of average radiolysis susceptibility for different compound classes (listed in Table 5.3).

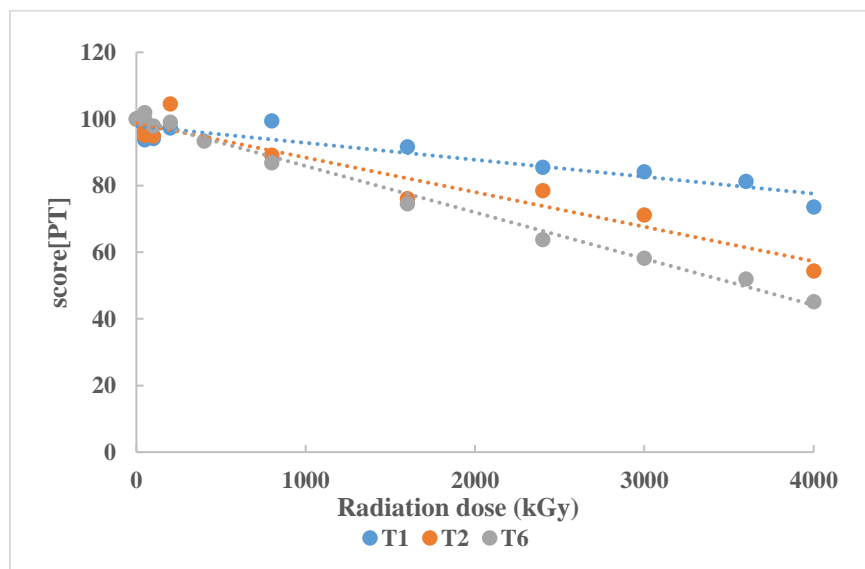


Fig. 5.4 Plots showing the variation of "score" for hopanes (PTs) with radiation dose for T1, T2 and T6 samples (kGy)

The hopanes score plot [PT], for example (Fig. 5.4), for each oil against radiation dose shows that the radiolysis rates of hopanes varied in different oils (T1>T2>T6). The radiolysis rate was negatively correlated with the API value as well as viscosity. The lighter oil (T6), with lowest viscosity was destroyed faster than the heavier, high viscosity oil (T1).

5.2.2 Aromatic hydrocarbons: N, P, DBTs and TAS

The typical aromatic hydrocarbons C₀₋₅ naphthalenes, C₀₋₂ phenanthrenes, dibenzothiophenes and triaromatic steroid hydrocarbons were also plotted against radiation doses (Fig. 5.5). Compared with saturated hydrocarbons, the aromatic hydrocarbons generally show higher radiolysis rates.

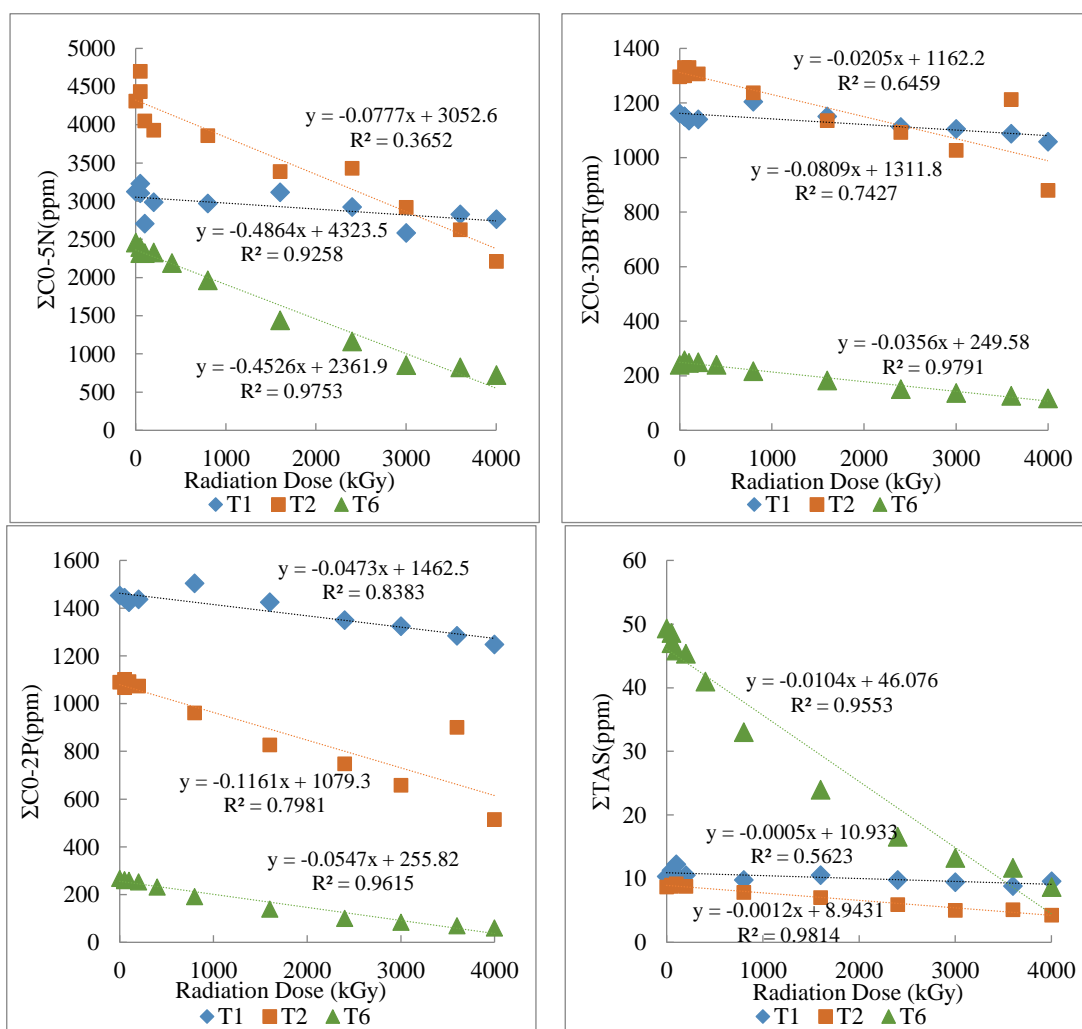


Fig. 5.5 Plots showing the variation in concentrations of C₀₋₅ naphthalenes (C₀₋₅ N), C₀₋₂ phenanthrenes (C₀₋₂P), dibenzothiophenes (DBTs) and triaromatic steroid hydrocarbons (TAS) with radiation dose for T1, T2 and T6 samples (kGy)

Fig. 5.6 indicates that the scores for P (similar for N, TAS and DBT) also varied in different oil samples (T1 > T2 > T6). Again, the scores were negatively correlated with the API value as well as viscosity. The radiolysis mechanism for aromatic hydrocarbons is similar to the saturated hydrocarbons. While, for these Tarim oils, the saturated hydrocarbons have smaller ranges of scores (more resistant to high-dose irradiation).

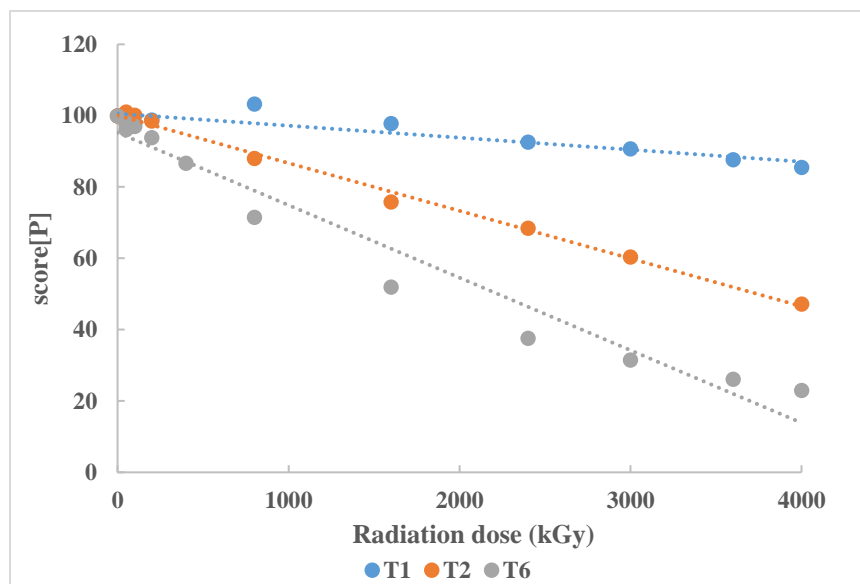


Fig. 5. 6 Plots showing the variation of "score" for Phenanthrenes (P) with radiation dose for T1, T2 and T6 samples (kGy)

The SCORE for T1: hopanes > TAS > steranes > tricyclic terpanes > phenanthrenes > naphthalenes > DBTs > BSTs > *n*-alkanes & adamantanes. For T2: TAS > naphthalenes > phenanthrenes > hopanes > DBTs > tricyclic terpanes > steranes > adamantanes > BSTs > *n*-alkanes. The SCORE for T6: TAS > phenanthrenes > naphthalenes > DBTs > hopanes > steranes and tricyclic terpanes > BSTs > adamantanes > *n*-alkanes. Although the order of SCOREs classes varies among different oil type, the trend can be suggested as: SCORE for aromatic hydrocarbons were generally higher than saturated hydrocarbons, correlating to an overall higher degradability and radiolysis rates.

Table 5.3 Radiolysis SCORE for compounds in T1, T2 and T6 high-dose irradiated samples

	C ₀₋₅ N	C ₀₋₃ DBT	C ₁₋₂ P	TAS	<i>n</i> -alkanes	Ad	BSTs	TTs	PTs	STs
T1	10	7	13	18	2	2	3	15	20	17
T2	45	25	43	54	0	19	1	21	36	17
T6	74	59	81	84	7	16	28	40	56	40

For different oil types, the destruction rates varied with highest SCORE for T6 (lighter oil) and lowest for T1 (heavier oil). It can be concluded that the radiolysis rate is directly affected by the oil matrix, and positively correlated with the API value (negatively correlated with the density and viscosity for original oils). Besides, the stability of saturated and aromatic hydrocarbons in different type of oils also varied a lot, which could be due to the inner matrix variation.

Case study II: Low-dose irradiated oils from the North Sea and Barents Sea, Norway

5.3 Basic geochemical characteristics of original oils from North Sea and Barents Sea

As described in Chapter three, GC-MS analysis was carried out for 23 crude oil samples (Table 3.3) that were collected from the North Sea and Barents Sea. The North Sea samples in this study (Utsira High and Brynhild) were mainly sourced from Upper Jurassic strata, while the Barents Sea oils were sourced from Triassic strata. This could be verified by the abundant occurrence of C₂₈ bisnorhopane for Utsira High and Brynhild samples (Fig. 5.7), which is often called a marker for Upper Jurassic sourced oils in the North Sea and is associated with anoxic deposition environments (Grantham et al., 1980; Dahl, 2004).

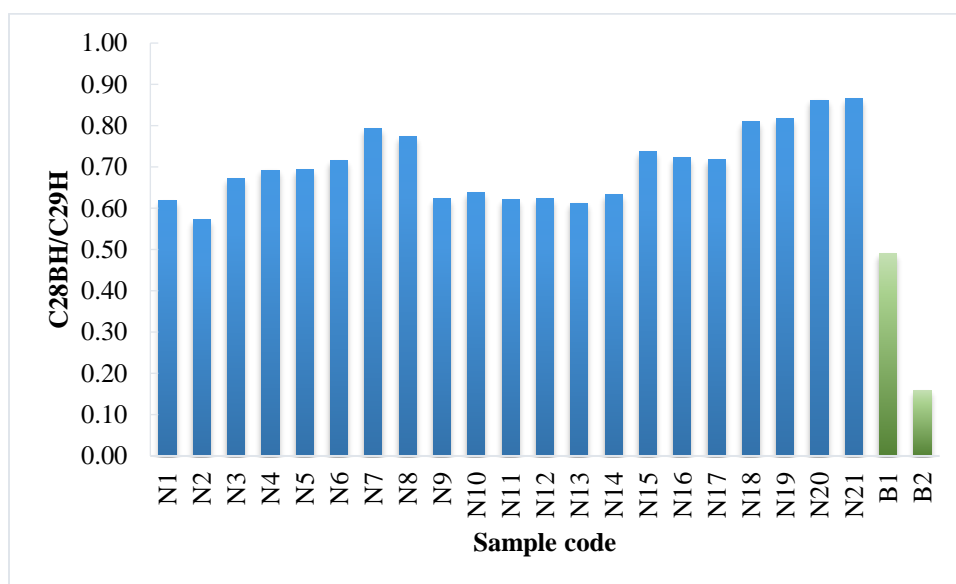


Fig. 5.7 Ratio of C₂₈BH/C₂₉H (C₂₈ bisnorneohopane/ C₂₉ 17 α (H),21 β (H) hopane) for 23 investigated oils from North Sea and Barents Sea area (well data from *Lundin Energy*)

The steranes were characterized by a predominance of C₂₇ relative to C₂₈ and C₂₉ steranes although there are some variations (Fig. 5.8). The slight dominance of C₂₇ regular steranes over the C₂₉ homologues indicated that these samples were generally dominated by marine algal organic matter with terrigenous input.

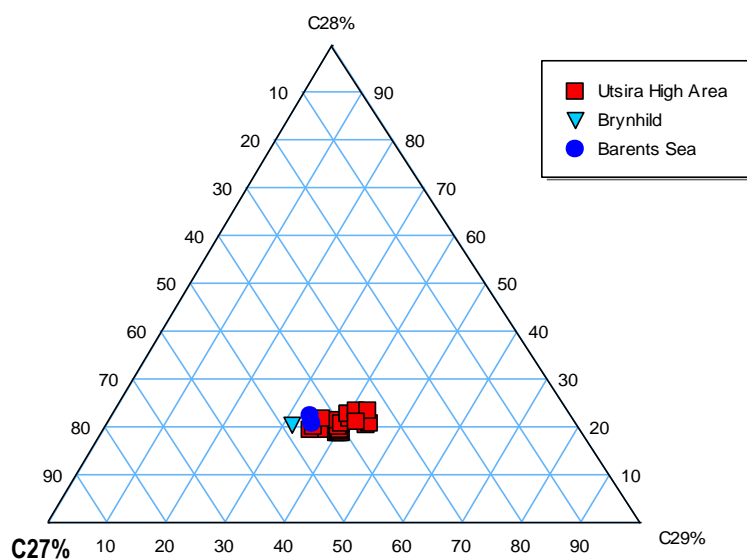


Fig. 5.8 Ternary plot of C₂₇₋₂₉ regular steranes

To assess the thermal maturity level of these oils, typical parameters, such as C₂₉ 20S/(20S+20R) and $\beta\beta/(\alpha\alpha+\beta\beta)$ ratios were calculated and plotted (Fig. 5.9). With increasing maturity, the isomerisation at C₂₉-steranes will cause an increase in both values. Therefore, a good correlation may show that the oil samples from the North Sea are generally less mature than the samples from Barents Sea.

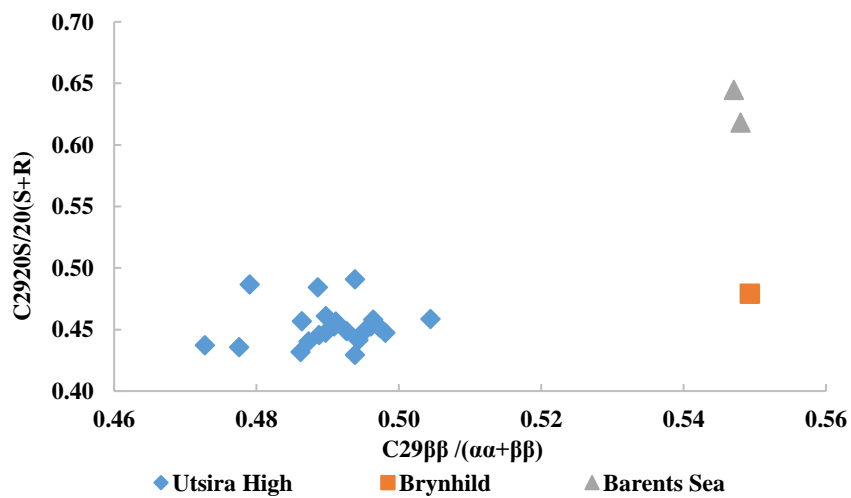


Fig. 5.9 Cross plot of C₂₉ $\beta\beta/(\alpha\alpha+\beta\beta)$ versus C₂₉ 20S/(20S+20R)

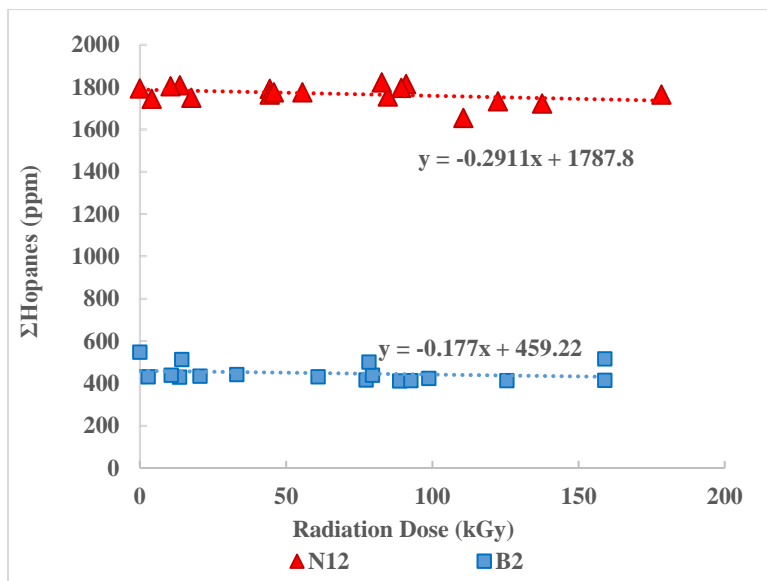
Seven representative samples (Table 3.4) were selected to be irradiated under low-dose γ -radiation (~0–200 kGy). After irradiation, sample set "N12" from North Sea and "B2" from Barents Sea were selected as test samples for GC-MS analysis.

5.4 Compound destruction under low-dose irradiation

5.4.1 Concentration: no significant change

The objective for conducting low-dose irradiation experiments was initially to mimic the natural radiation process in reservoirs and build a more precise correlation of compounds with radiation doses in the low-dose range.

As Fig. 5.10 shows, for representative compounds in these low-dose irradiated oils, the data was inconsistent and concentration barely changed on GC-MS results. This indicated that low-dose irradiation effect might not be precisely detected only using GC-MS. However, it is necessary and important to conduct the design and development of low-dose experiments as the first step to consider natural in-reservoir radiolysis process. More analytical tools such as the Bruker 12 Tesla Fourier Transform Ion Cyclotron Resonance Mass Spectrometer (FT-ICR-MS), a new high-resolution molecular analytical instrument, needs to be tested in the future to characterize the variation among low-dose irradiated oils.



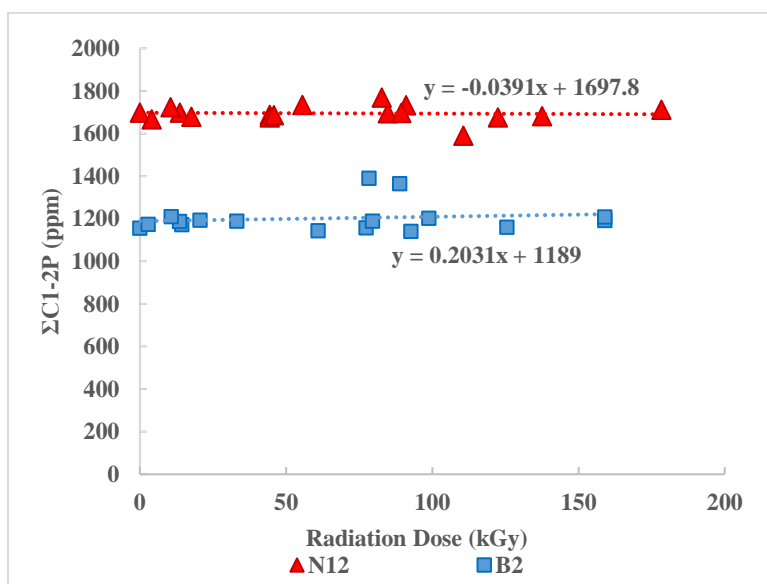
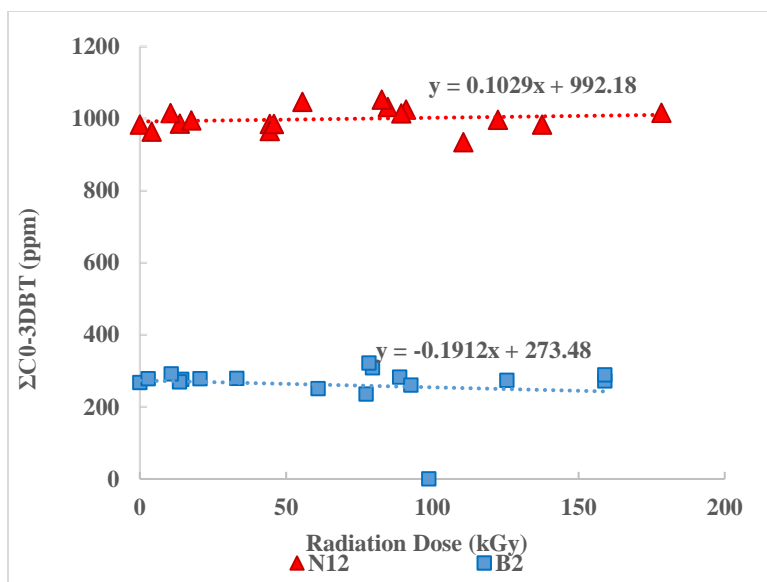


Fig. 5.10 Plots showing the variation in concentrations of steranes with radiation dose (kGy)

Chapter Six: Conclusions and Future work

Dating fluid residence time in reservoirs is typically important in petroleum system evaluation, basin modeling and carbon storage studies and is currently based on indirect methods. In Chapter one, a brief introduction of earlier attempts to assess fluid residence time in petroleum reservoirs based on the literature review was given. Limitations exist in the current age dating tools such as K/Ar dating of illite, fluid inclusion and Re/Os dating. This research aimed at developing a new precise analytical method to permit functional dating of reservoirs by organic geochemical proxies with realistic reservoir gamma ray doses.

Motivated by the previous finding of olefins in crude oil and the development of radiation chemistry, a series of high-dose (50–10000 kGy) and low-dose (0–200 kGy) gamma ray irradiation experiments were designed and conducted on different type of crude oils to investigate their radiolysis effects and mechanisms. Over two hundred compounds were selected and analyzed by GC-MS. The majority of GC-MS monitored compounds is destroyed after radiolysis, showing a negative slope of concentration with dose (ppm/ Δ kGy).

It is concluded that the different destruction rates in crude oils, which is represented by the degradation slope, depend on the following 3 major factors:

1. Original concentration: the original concentration of individual compounds (non-irradiated) is considered as the most important influencing factor during radiolysis process, and significantly affects the destruction rates for the majority of investigated compound.
2. Compound classes: aromatic hydrocarbons are generally more resistant to radiolysis than saturated hydrocarbons. Based on the high-dose irradiation results, compounds radiolysis sensitivity can be sorted as follows: hopanes > TAS and MAS > steranes > tricyclic terpanes > phenanthrenes > naphthalenes > BSTs > *n*-alkanes > DBTs > adamantanes.
3. Oil matrix: the radiolysis rate is directly affected by the oil matrix, and is negatively correlated with the density and viscosity for original oils.

The GC-MS results of low-dose irradiation experiments were also generated, while they show insignificant changes or correlations between compounds concentration and irradiation doses. This indicated that more analytical tools need to be tested in the future to characterize the variation among low-dose irradiated oils.

REFERENCES

- Aczel, T., Gorbaty, M.L., Maa, P.S., Schlosberg, R.H., 1979. Stability of adamantane and its derivatives to coal-liquefaction conditions, and its implications toward the organic structure of coal. *Fuel* 58(3), 228-230.
- Aquino Neto, F.R., Trendel, J.M., Restle, A., Connan, J., Albrecht, P.A., 1983. Occurrence and formation of tricyclic and tetracyclic terpanes in sediments and petroleums. In: M.Bjørøy, et al. (Editors), *Advances in Organic Geochemistry 1981*, Wiley, Chichester, 659-667.
- Barnard, P.C., Cooper, B.S., 1981. Oils and source rocks of the North Sea area. In: Illing, L.V., Hobson, G.D. (Eds.), *Petroleum Geology of the Continental Shelf of North-West Europe: Proceedings of the 2nd Conference*. Heyden and Son, London, 169-175.
- Bastow, T.P., van Aarssen, B.G., Lang, D., 2007. Rapid small-scale separation of saturate, aromatic and polar components in petroleum. *Organic Geochemistry* 38(8), 1235-1250.
- Bennett, B., Larter, S.R., 2000. Quantitative separation of aliphatic and aromatic hydrocarbons using silver ion-silica solid-phase extraction. *Analytical Chemistry* 72, 1039-1044.
- Brooks, J.D., Gould, K., Smith, J.W., 1969. Isoprenoid hydrocarbons in coal and petroleum. *Nature*, 222, 257-9.
- Chappe, B., Albrecht, P., Michaelis, W., 1982. Polar lipids of archaeobacteria in sediments and petroleums. *Science* 217(4554), 65-66.
- Chmielewski, A.G., 2007. Practical applications of radiation chemistry. *Russian Journal of Physical Chemistry A, Focus on Chemistry* 81(9), 1488-1492.
- Coward, M.P., 1995. Structural and tectonic setting of the Permo-Triassic basins of northwest Europe. In: Boldy, S.A.R. (ed.) *Permian and Triassic Rifting in Northwest Europe*. Geological Society, London, Special Publication 91, 7-39.
- Dahl, B., 2004. The use of bisnorhopane as a stratigraphic marker in the Oseberg Back Basin, North Viking Graben, Norwegian North Sea. *Organic geochemistry* 35(11), 1551-1571.
- Erwin, D.H., 2006. DATES AND RATES: Temporal Resolution in the Deep Time Stratigraphic Record. *Annual Review of Earth and Planetary Sciences* 34, 569-590.
- Færseth, R.B., 1996. Interaction of Permo-Triassic and Jurassic extensional fault-blocks during the development of the northern North Sea. *Journal of the Geological Society* 153(6), 931-944.
- Frolov, E.B., Smirnov, M.B., 1994. Unsaturated hydrocarbons in crude oils. *Organic geochemistry* 21(2), 189-208.
- Frolov, E.B., Smirnov, M.B., Melikhov, V.A., Vanyukova, N.A., 1998. Olefins of radiogenic origin in crude oils. *Organic geochemistry* 29(1-3), 409-20.
- Gabrielsen, R.H., R.B., Færseth, L.N., Jensen, J.E., Kalheim, F.R., 1990. Structural elements of the Norwegian continental shelf: I. The Barents Sea region: Norwegian Petroleum Directorate Bulletin 6, 33

- Glasmann, J.R., Lundegard, P.D., Clark, R.A., Penny, B.K., Collins, I.D., 1989. Geochemical evidence for the history of diagenesis and fluid migration; Brent Sandstone, Heather Field, North Sea. *Clay Minerals* 24(2), 255-84.
- Glennie, K.W., Underhill, J.R., 1998. The development and evolution of structural styles in the North Sea. In: Glennie, K.W. (ed.) *Introduction to the Petroleum Geology of the North Sea: Basic Concepts and Recent Advances*. Blackwell Science, Oxford, 42-84.
- Goossens, H. D., De Leeuw, J. W., Schenck, P. A., Brassell, S. C., 1984. Tocopherols as likely precursors of pristane in ancient sediments and crude oils. *Nature* 312(5993), 440-442.
- Grantham, P.J., Posthuma, J., De Groot, K., 1980. Variation and significance of the C₂₇ and C₂₈ triterpane content of a North Sea core and various North Sea crude oils. *Physics and Chemistry of the Earth* 12, 29-38.
- Haszeldine R.S, Cavanagh, A.J, England G.L., 2003. Effects of oil charge on illite dates and stopping quartz cement: calibration of basin models. *Journal of Geochemical Exploration*, 78:373-6.
- Hoering, T.C., 1977. Olefinic hydrocarbons from Bradford, Pennsylvania, crude oil. *Chemical Geology* 20, 1-8.
- Huang, H.P., Pearson, M.J., 1999. Source rock palaeoenvironments and controls on the distribution of dibenzothiophenes in lacustrine crude oils, Bohai Bay Basin, eastern China. *Organic Geochemistry* 30, 1455-1470
- Huang, H., Bowler, B.F., Oldenburg, T.B., Larter, S.R., 2004. The effect of biodegradation on polycyclic aromatic hydrocarbons in reservoir oils from the Liaohe basin, NE China. *Organic geochemistry* 35(11), 1619-1634.
- Isaksen, G.H., Ledje, K.H.I., 2001. Source rock quality and hydrocarbon migration pathways within the greater Utsira High area, Viking Graben, Norwegian North Sea. *AAPG Bulletin* 85 (5), 861-883.
- Jackson, C.A., Kane, K.E., Larsen, E., 2010. Structural evolution of minibasins on the Utsira High, northern North Sea; implications for Jurassic sediment dispersal and reservoir distribution. *Petroleum Geoscience* 16(2), 105-120.
- Jia, C.Z., Wei, G.Q., 2002. Structural characteristics and petroliferous features of Tarim Basin. *Chinese Science Bulletin* 47, 1-11.
- Kane, K.E., Jackson, C.A.L., Larsen, E., 2010. Normal fault growth and fault-related folding in a salt-influenced rift basin: South Viking Graben, offshore Norway. *Journal of Structural Geology* 32(4), 490-506.
- Kelly, J., Parnell, J., Chen, H.G., 2000. Application of fluid inclusion to studies of fractured sandstone reservoirs, *Journal of Geochemical Exploration* 69: 705.
- Li, D.S., Liang, D.G., Jian, C.Z., Wang, G., Wu, Q.Z., He, D.F., 1996. Hydrocarbon accumulations in the Tarim Basin, China. *American Association of Petroleum Geologists Bulletin* 80, 1587-1603.

- Li, S.M., Pang, X.Q., Yang, H.J., Xiao, Z.Y., Gu, Q.Y., Zhang, B.S., Wang, H.J., 2010. Origin of crude oil in the Lunan region, Tarim Basin. *Acta Geologica Sinica – English Edition* 84, 1157-1169.
- Liewig, N., Clauer, N., 2000. K-Ar dating of varied microtextural illite in Permian gas reservoirs, northern Germany. *Clay Minerals* 35(1), 271-282.
- MacRae, A., 1998. Radiometric Dating and the Geological Time Scale. <http://www.talkorigins.org/faqs/dating.html> [accessed on 2017-03-08].
- Magoon, L.B., Dow, W.G., 1994. *The Petroleum System-From Source to Trap*. American Association of Petroleum Geologists, Tulsa.
- McLimans, R.K., 1987. The application of fluid inclusions to migration of oil and diagenesis in petroleum reservoirs. *Applied Geochemistry* 2(5-6): 585-603.
- Middleton, D., Parnell, J., Carey, P., Xu, G., 2000. Reconstruction of fluid migration history in Northwest Ireland using fluid inclusion studies. *Journal of Geochemical Exploration* 69, 673-677.
- Ohm, S.E., Karlsen, D.A., Austin, T.J.F., 2008. Geochemically driven exploration models in uplifted areas: Examples from the Norwegian Barents Sea. *American Association of Petroleum Geologists Bulletin* 92(9), 1191-1223.
- Ourisson, G., Albrecht, P., Rohmer, M., 1979. The hopanoids: palaeochemistry and biochemistry of a group of natural products. *Pure and Applied Chemistry* 51(4), 709-729.
- Ourisson, G., Albrecht, P., Rohmer, M., 1982. Predictive microbial biochemistry—from molecular fossils to procaryotic membranes. *Trends in Biochemical Sciences* 7(7), 236-239.
- Pang, H., Chen, J.Q., Pang, X.Q., Liu, K.Y., Xiang, C.F., 2012. Estimation of the hydrocarbon loss through major tectonic events in the Tazhong area, Tarim Basin, Basin, west China. *Marine and Petroleum Geology* 38, 195-210.
- Pegrum, R.M., Spencer, A.M., 1990. Hydrocarbon plays in the northern North Sea. In: Brooks, J. (Ed.), *Classic petroleum provinces*. Geological Society Special Publication 50, 441-470.
- Peters, K.E., Walters, C.C., Moldowan, J.M., 2005. *The Biomarker Guide*. Vol. 1. Cambridge University Press, 2005.
- Radke, M., 1988. Application of aromatic compounds as maturity indicators in source rocks and crude oils. *Marine and Petroleum Geology* 5(3), 224-236.
- Thomas, D.W., Coward, M.P. 1996. Mesozoic regional tectonics and South Viking Graben formation: evidence for localized thin-skinned detachments during rift development and inversion. *Marine and Petroleum Geology* 13, 149-177.
- Villarreal-Barajas, J.E., Khan, R.F., 2014. Energy response of EBT3 radiochromic films: implications for dosimetry in kilovoltage range. *Journal of Applied Clinical Medical Physics*, 15(1).
- Williams, F., 1963. Radiation chemistry of hydrocarbons. *Quarterly Reviews, Chemical Society* 17(2), 101-132.

- Wingert, W.S., 1992. GC-MS analysis of diamondoid hydrocarbons in Smackover petroleums. *Fuel* 71(1), 37-43.
- Yang, C., Wang, Z., Hollebhone, B.P., Brown, C.E., Landriault, M., 2009. Characteristics of bicyclic sesquiterpanes in crude oils and petroleum products. *Journal of Chromatography A* 1216(20), 4475-4484.
- Zhang, S.C., Hanson, A.D., Moldowan, J.M., Graham, S.A., Liang, D.G., Chang, E., Fago, F., 2000. Paleozoic oil–source rock correlations in the Tarim Basin, NW China. *Organic Geochemistry* 31, 273-286.
- Zhang, S., Huang, H., 2005. Geochemistry of Palaeozoic marine petroleum from the Tarim Basin, NW China: Part 1. Oil family classification. *Organic Geochemistry* 36(8), 1204-1214.
- Zhang, S.C., Huang, H.P., Xiao, Z.Y., Liang, D.G., 2005. Geochemistry of Palaeozoic marine petroleum from the Tarim Basin, NW China. Part 2: maturity assessment. *Organic Geochemistry* 36, 1215-1225.
- Zhang, S.C., Su, J., Wang, X.M., Zhu, G.Y., Yang, H.J., Liu, K.Y., Li, Z.X., 2011. Geochemistry of Palaeozoic marine petroleum from the Tarim Basin, NW China. Part 3: thermal cracking of liquid hydrocarbons and gas washing as the major mechanisms for deep gas condensate accumulations. *Organic Geochemistry* 42, 1394-1410.
- Zhang, S., Huang, H., Su, J., Liu, M., Wang, X., Hu, J., 2015. Geochemistry of Paleozoic marine petroleum from the Tarim Basin, NW China: Part 5. Effect of maturation, TSR and mixing on the occurrence and distribution of alkyldibenzothiophenes. *Organic Geochemistry* 86, 5-18.
- Ziegler, P.A., 1990. Tectonic and palaeogeographic development of the North Sea rift system. In: Blundell, D.J. & Gibbs, A.D. (eds) *Tectonic Evolution of the North Sea Rifts*. *International Lithosphere Programme* 81, 1-36.
- Ziegler, P.A., 1992. North Sea rift system. *Tectonophysics* 208, 55-75

APPENDIX 1: GC-MS IDENTIFICATION OF COMPOUNDS

A1.1 Saturated hydrocarbons

Table A1.1 Normal and isoprenoid alkanes m/z 85

Peak	m/z	Compound	Abbreviation
1	85	normal alkane C ₈	<i>n</i> -C ₈
2	85	normal alkane C ₉	<i>n</i> -C ₉
3	85	normal alkane C ₁₀	<i>n</i> -C ₁₀
4	85	normal alkane C ₁₁	<i>n</i> -C ₁₁
5	85	normal alkane C ₁₂	<i>n</i> -C ₁₂
6	85	normal alkane C ₁₃	<i>n</i> -C ₁₃
7	85	normal alkane C ₁₄	<i>n</i> -C ₁₄
8	85	normal alkane C ₁₅	<i>n</i> -C ₁₅
9	85	normal alkane C ₁₆	<i>n</i> -C ₁₆
10	85	normal alkane C ₁₇	<i>n</i> -C ₁₇
11	85	Pristane	Pr
12	85	normal alkane C ₁₈	<i>n</i> -C ₁₈
13	85	Phytane	Ph
14	85	normal alkane C ₁₉	<i>n</i> -C ₁₉
15	85	normal alkane C ₂₀	<i>n</i> -C ₂₀
16	85	normal alkane C ₂₁	<i>n</i> -C ₂₁
17	85	normal alkane C ₂₂	<i>n</i> -C ₂₂
18	85	normal alkane C ₂₃	<i>n</i> -C ₂₃
19	85	normal alkane C ₂₄	<i>n</i> -C ₂₄
20	85	normal alkane C ₂₅	<i>n</i> -C ₂₅
21	85	normal alkane C ₂₆	<i>n</i> -C ₂₆
22	85	normal alkane C ₂₇	<i>n</i> -C ₂₇
23	85	normal alkane C ₂₈	<i>n</i> -C ₂₈
24	85	normal alkane C ₂₉	<i>n</i> -C ₂₉
25	85	normal alkane C ₃₀	<i>n</i> -C ₃₀
26	85	normal alkane C ₃₁	<i>n</i> -C ₃₁
27	85	normal alkane C ₃₂	<i>n</i> -C ₃₂
28	85	normal alkane C ₃₃	<i>n</i> -C ₃₃
29	85	normal alkane C ₃₄	<i>n</i> -C ₃₄
30	85	normal alkane C ₃₅	<i>n</i> -C ₃₅

Table A1.2 Bicyclic sesquiterpane m/z 123

Peak	m/z	Compound	Abbreviation
31	123	C ₁₅ bicyclic alkane	C15BA1
32	123	C ₁₅ bicyclic alkane	C15BA2
33	123	8 β (H)-drimane	8 β DR
34	123	C ₁₅ bicyclic alkane	BC4
35	123	C ₁₅ bicyclic alkane	BC5
36	123	C ₁₅ bicyclic alkane	BC6
37	123	C ₁₅ bicyclic alkane	BC7
38	123	8 β (H)-homodrimane	ND12

Table A1.3 Terpanes m/z 191

Peak	m/z	Compound	Abbreviation
39	191	C ₁₉ tricyclic terpane	19TT
40	191	C ₂₀ tricyclic terpane	20TT
41	191	C ₂₁ tricyclic terpane	21TT
42	191	C ₂₂ tricyclic terpane	22TT
43	191	C ₂₃ tricyclic terpane	23TT
44	191	C ₂₄ tricyclic terpane	24TT
45	191	C ₂₅ tricyclic terpane	25TT
46	191	C ₂₄ tetracyclic terpane	24TeT
47	191	C ₂₆ tricyclic terpane	26TTa
48	191	C ₂₆ tricyclic terpane	26TTb
49	191	C ₂₈ tricyclic terpane	28TTa
50	191	C ₂₈ tricyclic terpane	28TTb
51	191	C ₂₉ tricyclic terpane	29TTa
52	191	C ₂₉ tricyclic terpane	29TTb
53	191	C ₂₇ 18 α (H)-22,29,30- trisnorneohopane	Ts
54	191	C ₂₇ 17 α (H)-22,29,30- trisnorneohopane	Tm
55	191	C ₃₀ tricyclic terpane	30TTa
56	191	C ₃₀ tricyclic terpane	30TTb
57	191	C ₂₈ bisnorneohopane	28BH
58	191	C ₂₉ 17 α (H),21 β (H) hopane	29H
59	191	C ₂₉ 18 α (H)-30-norneohopane	29Ts
60	191	C ₃₀ 17 α (H) diahopane	30DiaH
61	191	C ₂₉ 17 β (H),21 α (H)hopane	29M
62	191	C ₃₀ 17 α (H),21 β (H)hopane	30H
63	191	C ₃₀ 17 β (H),21 α (H)hopane	30M
64	191	C ₃₁ 17 α (H),21 β (H) 22S homohopane	31HS
65	191	C ₃₁ 17 α (H),21 β (H) 22R homohopane	31HR
66	191	gammacerane	GAM
67	191	C ₃₂ 17 α (H),21 β (H) 22S homohopane	32HS
68	191	C ₃₂ 17 α (H),21 β (H) 22R homohopane	32HR
69	191	C ₃₃ 17 α (H),21 β (H) 22S homohopane	33HS
70	191	C ₃₃ 17 α (H),21 β (H) 22R homohopane	33HR
71	191	C ₃₄ 17 α (H),21 β (H) 22S homohopane	34HS
72	191	C ₃₄ 17 α (H),21 β (H) 22R homohopane	34HR
73	191	C ₃₅ 17 α (H),21 β (H) 22S homohopane	35HS
74	191	C ₃₅ 17 α (H),21 β (H) 22R homohopane	35HR

Table A1.3 Steranes m/z 217

Peak	m/z	Compound	Abbreviation
75	217	C ₂₁ ααα+αββ pregnane	21PREG
76	217	C ₂₂ ααα+αββ pregnane	22PREG
77	217	C ₂₇ 10β(H),13α(H) 20S diasterane	C27baS
78	217	C ₂₇ 10β(H),13α(H) 20R diasterane	C27baR
79	217	C ₂₇ 10α(H),13β(H) 20S diasterane	27abS
80	217	C ₂₇ 10α(H),13β(H) 20R diasterane	27abR
81	217	C ₂₈ 10β(H),13α(H) 20S diasterane	28baS
82	217	C ₂₈ 10β(H),13α(H) 20R diasterane	28baR
83	217	C ₂₈ 10α(H),13β(H) 20S diasterane + C ₂₇ 5α(H),14α(H),17α(H) 20S sterane	28abS+27aaaS
84	217	C ₂₉ 10β(H),13α(H) 20S diasterane + C ₂₇ 5α(H),14β(H),17β(H) 20R sterane	29baS+27abbR
85	217	C ₂₈ 10α(H),13β(H) 20S diasterane + C ₂₇ 5α(H),14α(H),17α(H) 20S sterane	28abR+27abbS
86	217	C ₂₇ 5α(H),14α(H),17α(H) 20R sterane	27aaaR
87	217	C ₂₉ 10β(H),13α(H) 20R diasterane	C29baR
88	217	C ₂₈ 10α(H),13β(H) 20S diasterane	29abS
89	217	C ₂₈ 5α(H),14α(H),17α(H) 20S sterane	28aaaS
90	217	C ₂₉ 10α(H),13β(H) 20S diasterane + C ₂₈ 5α(H),14β(H),17β(H) 20R sterane	29abR+28abbR
91	217	C ₂₈ 5α(H),14α(H),17α(H) 20S sterane	28abbS
92	217	C ₂₈ 5α(H),14α(H),17α(H) 20R sterane	28aaaR
93	217	C ₂₈ 5α(H),14α(H),17α(H) 20S sterane	29aaaS
94	217	C ₂₉ 5α(H),14β(H),17β(H) 20R sterane	29abbR
95	217	C ₂₉ 5α(H),14α(H),17α(H) 20S sterane	29abbS
96	217	C ₂₉ 5α(H),14α(H),17α(H) 20R sterane	29aaaR
97	217	C ₂₇ 10β(H),13α(H) 20S diasterane	C27baS
98	217	C ₂₇ 10β(H),13α(H) 20R diasterane	C27baR
99	217	C ₂₇ 10α(H),13β(H) 20S diasterane	27abS
100	217	C ₂₇ 10α(H),13β(H) 20R diasterane	27abR
101	217	C ₂₈ 10β(H),13α(H) 20S diasterane	28baS
102	217	C ₂₈ 10β(H),13α(H) 20R diasterane	28baR
103	217	C ₂₈ 10α(H),13β(H) 20S diasterane + C ₂₇ 5α(H),14α(H),17α(H) 20S sterane	28abS+27aaaS
104	217	C ₂₉ 10β(H),13α(H) 20S diasterane + C ₂₇ 5α(H),14β(H),17β(H) 20R sterane	29baS+27abbR
105	217	C ₂₈ 10α(H),13β(H) 20S diasterane + C ₂₇ 5α(H),14α(H),17α(H) 20S sterane	28abR+27abbS
106	217	C ₂₇ 5α(H),14α(H),17α(H) 20R sterane	27aaaR

Table A1.4 Adamantanes m/z 136, 135, 149, 163, 177

Peak	m/z	Compound	Abbreviation
107	136	adamantane	AD
108	135	1-methyladamantane	1MAD
109	135	2-methyladamantane	2MAD
110	135	1-ethyladamantane	1EAD
111	135	2-ethyladamantane	2EAD
112	149	1,3-dimethyladamantane	13DMAD
113	149	1,4-dimethyladamantane (cis)	14DMADc
114	149	1,4-dimethyladamantane (trans)	14DMADt
115	149	1,2-dimethyladamantane	12DMAD
116	149	1-ethyl-3-methyladamantane	1E3MAD
117	163	1,3,5-trimethyladamantane	135TMAD
118	163	1,3,6-trimethyladamantane	136TMAD
119	163	1,3,4-trimethyladamantane (cis)	134TMADc
120	163	1,3,4-trimethyladamantane (trans)	134TMADt
121	163	1-ethyl-3,5-dimethyladamantane	1E35DMAD
122	177	1,3,5,7-tetramethyladamantane	1357TeMAD
123	177	1,2,5,7-tetramethyladamantane	1257TeMAD

A1.2 Aromatic hydrocarbons

Table A2.1 Naphthalene and alkylnaphthalenes m/z 128, 142, 156, 170, 184, 198

Peak	m/z	Compound	Abbreviation
124	128	naphthalene	N
125	142	2-methylnaphthalene	2MN
126	142	1-methylnaphthalene	1MN
127	156	2-ethylnaphthalene	2EN
128	156	1- ethylnaphthalene	1EN
129	156	2,6- + 2,7-dimethylnaphthalene	26,27DMN
130	156	1,3- + 1,7- dimethylnaphthalene	13,17DMN
131	156	1,6- dimethylnaphthalene	16DMN
132	156	1,4- +2,3- dimethylnaphthalene	14,23DMN
133	156	1,5- dimethylnaphthalene	15DMN
134	156	1,2- dimethylnaphthalene	12DMN
135	170	1,3,7-trimethylnaphthalene	137TMN
136	170	1,3,6- trimethylnaphthalene	136TMN
137	170	1,3,5- + 1,4,6- trimethylnaphthalene	135,146TMN
138	170	2,3,6- trimethylnaphthalene	236TMN
139	170	1,2,7- + 1,6,7- + 1,2,6- trimethylnaphthalene	127,167,126TMN
140	170	1,2,4- trimethylnaphthalene	124TMN
141	170	1,2,5- trimethylnaphthalene	125TMN
142	170	1,2,3- trimethylnaphthalene	123TMN
143	184	1,3,5,7-tetramethylnaphthalene	1357TeMN
144	184	1,3,6,7- tetramethylnaphthalene	1367TeMN
145	184	1,2,4,6- + 1,2,4,7- + 1,4,6,7 tetramethylnaphthalene	1246,1247,1467TeMN
146	184	1,2,5,7- tetramethylnaphthalene	1257TeMN
147	184	2,3,6,7- tetramethylnaphthalene	2367TeMN
148	184	1,2,6,7- tetramethylnaphthalene	1267TeMN
149	184	1,2,3,7- tetramethylnaphthalene	1237TeMN
150	184	1,2,3,6- tetramethylnaphthalene	1236TeMN
151	184	1,2,5,6- + 1,2,3,5 tetramethylnaphthalene	1256,1235TeMN
152	198	1,2,4,6,7-pentamethylnaphthalene	12467PMN
153	198	1,2,3,5,7- pentamethylnaphthalene	12357PMN
154	198	1,2,3,6,7- pentamethylnaphthalene	12367PMN
155	198	1,2,3,5,6- pentamethylnaphthalene	12356PMN

Table A2.2 Phenanthrene and alkylphenanthrenes m/z 178, 192, 206

Peak	m/z	Compound	Abbreviation
156	178	phenanthrene	P
157	192	3-methylphenanthrene	3MP
158	192	2-methylphenanthrene	2MP
159	192	9-methylphenanthrene	9MP
160	192	1-methylphenanthrene	1MP
161	206	3-ethylphenanthrene	3EP
162	206	9-,2-,1-ethyl + 3,6-dimethylphenanthrene	36,92DMP,1EP
163	206	3,5- + 2,6-dimethylphenanthrene	35,26DMP
164	206	2,7-dimethylphenanthrene	27DMP
165	206	1,3- +3,9- +2,10- +3,10-dimethylphenanthrene	13,39,210,310DMP
166	206	2,,5- +2,9- +1,6-dimethylphenanthrene	25,29,16DMP
167	206	1,7-dimethylphenanthrene	17DMP
168	206	2,3-dimethylphenanthrene	23DMP
169	206	1,9- +4,9- +4,10-dimethylphenanthrene	19,49,410DMP
170	206	1,8-dimethylphenanthrene	18DMP
171	206	1,2-dimethylphenanthrene	12DMP

Table A2.3 Dibenzothiophene and alkyl dibenzothiophenes m/z 184, 198, 212

Peak	m/z	Compound	Abbreviation
172	184	dibenzothiophene	DBT
173	198	4-methyldibenzothiophene	4MDBT
174	198	2,3-methyldibenzothiophene	2,3MDBT
175	198	1-methyldibenzothiophene	1MDBT
176	212	4-ethyldibenzothiophene	4EDBT
177	212	4,6-dimethyldibenzothiophene	46DMDBT
178	212	2,4-dimethyldibenzothiophene	24DMDBT
	212	2,6-+2-ethyldibenzothiophene+3,6-	26,2EDBT,36DMDBT
179		dimethyldibenzothiophene	
180	212	3-ethyldibenzothiophene	3EDBT
	212	2,8-+2,7-+3,7-	28,27,37DMDBT
181		dimethyldibenzothiophene	
	212	1,6-+1,8-+1,4-	16,18,14DMDBT
182		dimethyldibenzothiophene	
183	212	1,3-+3,4-dimethyldibenzothiophene	13,34DMDBT
184	212	1,7-dimethyldibenzothiophene	17DMDBT
185	212	2,3-dimethyldibenzothiophene	23DMDBT
186	212	1,2-dimethyldibenzothiophene	12DMDBT

Table A2.4 Triaromatic and monoaromatic steroid hydrocarbons m/z 231, 253

Peak	m/z	Compound	Abbreviation
187	231	C ₂₀ -triaromatic steroid hydrocarbon	20TAS
188	231	C ₂₁ -triaromatic steroid hydrocarbon	21TAS
189	231	C ₂₆ 20S triaromatic steroid hydrocarbon	26STAS
190	231	C ₂₆ 20R+C ₂₇ 20S triaromatic steroid hydrocarbon	26R,27STAS
191	231	C ₂₈ 20S triaromatic steroid hydrocarbon	28STAS
192	231	C ₂₇ 20R triaromatic steroid hydrocarbon	27RTAS
193	231	C ₂₈ 20R triaromatic steroid hydrocarbon	28RTAS
194	253	C ₂₁ -monoaromatic steroid hydrocarbon	21MAS
195	253	C ₂₂ -monoaromatic steroid hydrocarbon	22MAS
196	253	C ₂₇ 14 β (H) 20S monoaromatic steroid hydrocarbon	27bSMAS
197	253	C ₂₇ 14 β (H) 20R monoaromatic steroid hydrocarbon	27bRMAS
198	253	C ₂₈ 14 β (H) 20S monoaromatic steroid hydrocarbon	28bSMAS
199	253	C ₂₉ 14 β (H) 20S+C ₂₈ 14 β (H) 20R monoaromatic steroid hydrocarbon	29bS,28bRMAS
200	253	C ₂₉ 14 α (H) 20S monoaromatic steroid hydrocarbon	29aSMAS
201	253	C ₂₉ 14 β (H) 20S+C ₂₈ 14 α (H) 20R monoaromatic steroid hydrocarbon	29bR,28aRMAS
202	253	C ₂₉ 14 α (H) 20R monoaromatic steroid hydrocarbon	29aRMAS